Politecnico di Milano

Scuola di Ingegneria Industriale e dell'Informazione

Corso di Laurea Magistrale in Ingegneria Matematica

Numerical Modelling of Ventricular Mechanics: Role of the Myofibre Architecture

Relatore:
Prof. Davide Carlo Ambrosi

Tesi di Laurea di:
Nicolò Matteo Colombo
Matr. 769995

Anno Accademico 2013/2014

Abstract

The heart is a complex organ whose function is to pump oxygenated blood through the network of arteries and veins; given its vital role, the understanding of the main functional and structural features of the cardiac muscle is a key element for the identification of common cardiac diseases. The cardiac tissue is characterized by a rather complex microstructure: it is composed of a helical network of muscle fibres, called myocytes, which are organized into laminar structures separated by cleavage planes. The understanding and the proper reproduction of the fibrous architecture is essential for a correct mechanical modelling of the cardiac muscle.

In this work, we focus on the left ventricle, which is the most important chamber in the heart, and we consider the Holzapfel-Ogden model for the passive cardiac tissue, which is assumed to be an incompressible orthotropic hyperelastic material; on the other hand, the contraction of the muscle fibres is enconded in the mathematical formulation using an active strain approach. Based on a simplified prolate geometry for the left ventricle, we provide a numerical solution for the variational formulation associated to the pressure-volume loop.

A great emphasis is placed on the modelling of the myocardial microstructure: as a matter of fact, the transmural variation of the fibre angle has a notable impact on the stress distribution inside the cardiac wall; moreover, it can influence the cardiac functionality in a significant way, improving or decreasing its efficiency and altering the ventricular shortening and twitch during the cardiac cycle. We also discuss the role of the presence of the transverse fibre angle, which induces a mechanical coupling bewteen the sub-endocardial and sub-epicardial layers, and we evaluate the effects of the organization of myofibres into laminar structures.

Furthermore, we investigate two additional modelling and mathematical issues: first, we analyse the influence of the second strain invariant in the mechanical model, which is usually neglected; then, we propose some possible modifications to standard boundary conditions, in order to take into account the effects of the surrounding anatomy of the ventricle.

Sintesi

La meccanobiologia è un campo di ricerca in forte sviluppo che si occupa dello studio del comportamento meccanico dei tessuti viventi, e costituisce il legame tra biologia ed ingegneria. Il cuore è un organo complesso, la cui funzione fondamentale è di pompare il sangue ossigenato attraverso il sistema circolatorio, costituito da vene ed arterie. Dato il suo ruolo vitale, la comprensione delle principali caratteristiche funzionali e strutturali del muscolo cardiaco è un elemento chiave per l'identificazione delle più comuni patologie cardiache. Nuovi modelli basati sulla meccanica dei continui, tecniche di visualizzazione avanzata e moderni strumenti per il calcolo numerico possono fornire una migliore comprensione della complessità del miocardio e guidare lo studio di nuove strategie per il trattamento delle patologie cardiache.

Nella nostra trattazione, l'attenzione viene posta sul ventricolo sinistro, che è la camera più importante del cuore ed è responsabile del pompaggio del sangue ossigenato attraverso la rete di arterie. La microstruttura del ventricolo è piuttosto complessa, in quanto è composto da una rete elicoidale di fibre muscolari, che sono a loro volta organizzate in strutture laminari, chiamate fogli. La configurazione di fibre del ventricolo può essere interamente descritta dalla definizione di due angoli, l'angolo elicodale e l'angolo trasverso, che determinano compiutamente l'orientamento del campo di fibre in ogni punto del ventricolo. Numerose ricerche di natura istologica sono state effettuate al fine di determinare la configurazione di fibre nel muscolo cardiaco, ma i risultati riportati nella letteratura risultano essere frequentemente in disaccordo. Lo scopo principale di questa tesi è di analizzare in modo completo come diverse configurazioni microstrutturali influiscono sulla meccanica e sull'efficienza del ventricolo: a questo fine, ci serviamo di una serie di indicatori fisiologici, ovvero quantità meccaniche e geometriche che definiscono in modo sintetico la funzionalità del ventricolo durante il ciclo cardiaco.

Dal punto di vista meccanico, il tessuto cardiaco è un materiale incomprimibile, iperelastico e ortotropo: di conseguenza, la relazione tra deformazione e sforzo viene descritta da una appropriata funzione densità di energia di deformazione. In questa tesi, viene utilizzato il modello proposto da Holzapfel e Ogden, basato su un insieme di invarianti ridotto e su uno splitting additivo dell'energia di deformazione, in cui ogni termine presenta una dipendenza esponenziale dal corrispettivo invariante. È ovviamente necessario codificare il comportamento attivo delle fibre muscolari, in quanto il loro accorciamento determina direttamente la contrazione cardiaca: per inserire questa caratteristica modellistica, vengono proposti due differenti approcci, ovvero *active stress* e *active strain*, dei quali soltanto il secondo viene utilizzato nel modello.

Successivamente, viene proposta un'approssimazione numerica del ciclo cardiaco, che porta a un problema di punto-sella non lineare, risolvibile tramite l'applicazione del

metodo di Newton. Dopo aver definito un'opportuna mesh computazionale, il problema in esame può essere risolto tramite il metodo degli elementi finiti, utilizzando opportuni spazi finito-dimensionali; questo metodo è stato implementato utilizzando il software FEniCS per la risoluzione di equazioni a derivate parziali. Viene quindi discussa una simulazione di riferimento, basata su una microstruttura semplice caratterizzata da una variazione transmurale dell'angolo elicoidale lineare.

Successivamente, l'attenzione viene posta sulla microstruttura cardiaca, ed in particolare sul suo impatto sulle principali quantità meccaniche e sull'efficienza cardiaca. Viene prima studiata la variazione dell'angolo elicoidale all'interno della parete ventricolare, mantenendo però fissati i valori dell'angolo sia all'endocardio che all'epicardio: la differente proporzione tra le fibre disposte in senso longitudinale e quelle circonferenziali e la loro diversa collocazione all'interno della parete hanno una notevole influenza sul ciclo cardiaco, alterando non solo la distribuzione di deformazione e sforzo, ma anche l'efficienza e la funzionalità ventricolare. In particolare, viene studiata l'asimmetria del campo di fibre rispetto al centro della parete e la rapida variazione dell'angolo elicoidale al centro della parete o in prossimità dei bordi. Successivamente, l'attenzione viene posta invece sull'angolo trasverso, che introduce un accoppiamento meccanico tra il sub-endocardio e il sub-epicardio ed è responsabile della riduzione dello shear transmurale. A conclusione dell'analisi microstrutturale, viene valutato il ruolo meccanico delle strutture laminari del miocardio.

Vengono poi analizzate due ulteriori problematiche modellistiche e numeriche: la prima riguarda l'introduzione nel modello meccanico del secondo invariante principale dello strain, che viene solitamente trascurato, e vengono proposti due differenti approcci per valutare l'importanza meccanica di questo invariante; in aggiunta, viene proposta una breve discussione riguardante l'imposizione delle condizioni al bordo nella formulazione variazionale.

CONTENTS

LIST OF FIGURES

LIST OF TABLES

INTRODUCTION

The emerging field of mechanobiology is focused on the study of the mechanical behaviour of living tissues and comprises the connection between biology and engineering. The heart is a complex organ whose function is to pump oxygenated blood through the network of arteries and veins; given its vital role, the understanding of the main functional and structural features of the cardiac muscle is a key element for the identification of common cardiac diseases. New models based on contiuum mechanics, advanced imaging techniques and modern simulation tools can provide a greater insight into the complexity of the myocardium and guide the design of new treatment strategies for cardiac pathologies.

The cardiac tissue is characterized by a complex microstructure: it is composed of a helical network of muscle fibres, called myocytes, which are organized into laminar structures separated by cleavage planes. The understanding and the proper reproduction of the fibrous architecture is essential for a better mechanical modelling of the cardiac muscle.

In Chapter 1, we resume the most important physiological features of the heart and its pumping function. In particular, we provide a detailed description of the microstructure of the myocardium, based on histological studies and advanced imaging techniques. We also introduce a set physiological indicators, such as ejection fraction, wall thickening and torsion, in order to allow a synthetic analysis of the cardiac efficiency.

In Chapter 2, we consider the Holzapfel-Ogden model for the passive cardiac tissue, which is assumed to be an incompressible orthotropic hyperelastic material; on the other hand, we encode the contraction of the muscle fibres in the mathematical formulation using an active strain approach. Based on a simplified prolate geometry for the left ventricle, we provide a numerical approximation for the pressure-volume loop, which can be properly solved thanks to the finite element method. In the last section of the chapter, we perform

a reference numerical simulation with a simple microstructural configuration.
In Chapter 3, we focus on the modelling of the fibrous microstructure: in particular, we evaluate the mechanical impact of the transmural variation of the helix angle of myofibres, while keeping the epicardial and endocardial angles fixed. Moreover, we also discuss the role of the transverse angle, which adds a mechanical coupling between the sub-epicardial and sub-endocardial layers of the cardiac muscle. For a complete microstructural study, the mechanical impact of different configurations of the laminar structure is also evaluated.
In Chapter 4, we investigate two additional modelling and mathematical issues: first, we analyse the influence of the second strain invariant in the mechanical model, which is usually neglected; then, we propose some minor modifications to boundary conditions, in order to take into account the effects of the surrounding anatomy of the ventricle.

CHAPTER 1

PHYSIOLOGY AND MICROSTRUCTURE OF THE HEART

Introduction

The heart is a muscular organ which pumps the blood through the network of arteries and veins, called the cardiovascular system; it is a very complex organ, both from the physiological and the mechanical point of view, and the structure of the heart has been the subject of several research projects in the last century. The most important chamber of the heart is the left ventricle, which pumps blood into the whole body thanks to its contraction, dictated by the shortening of myocardial fibres. The ventricle has a rather complex microstructure, which reflects in the orthotropic mechanical properties of the myocardium: it is composed of a helical network of *muscle fibres*, which are organized into laminar structures, called *sheets*, that are separated by cleavage surfaces. The correct configuration of the fibre and sheet architecture is a key issue for a proper modelling of the electrophysiological properties of the heart: in a clinical perspective, an accurate model which allows to perform a realistic simulation of the heart mechanics could be used as an important diagnostic tool.

In this section, we briefly recall the structure of the heart and the main features of the cardiac cycle. Moreover, we provide a detailed description of the microstructural features of the left ventricle, which have a great influence on the mechanical properties of the myocardium. Last but not least, we introduce a set of *physiological indicators*, which are mechanical and geometrical scalar quantities that can be used to check the proper functionality of the ventricle. For instance, during the post-processing phase of the numerical simulation we compute the thickening of the myocardial wall, the shortening and the torsion of the ventricle, to be compared with the correct physiological values: the main aim of this work is to explore the range of variability of geometrical and mechanical

characteristics of the ventricle that are know with some uncertainty, in order to minimize the discrepancy between these indicators and their real value. In particular, we focus on how they depend on the fibre orientation, on the boundary conditions imposed, and on other parameters of the mechanical model at hand.

1.1 Structure of the heart

Being the core of the circulatory system, the heart is an hollow muscular organ which works as a double pump, transporting blood away from it and back to it. The blood flowing to the right side of the heart is returning from the body and is sent to the lungs in order to receive oxygen; the oxygenated blood is then collected by the left atrium through the pulmonary veins and pumped into the aorta by the left ventricle, supplying the body with oxygen and other important nutrients. The heart is divided into four chambers, two atria and two ventricles: the blood is received by the atria, and during the cardiac cycle their contraction forces the blood into the respective ventricle, which pumps it out of the heart.

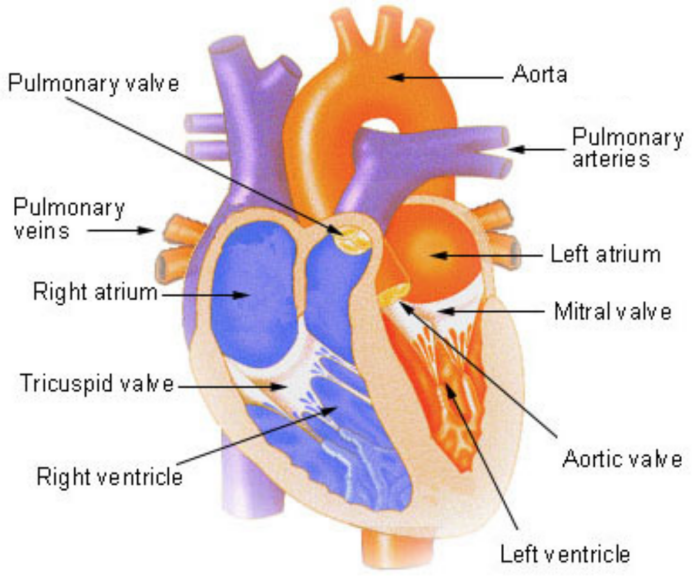

FIGURE 1.1: Chambers and blood vessels in the human heart.

The *pericardium* is a membrane that contains the heart and protects it while keeping it fixed to the surrounding structures and avoiding excessive stretch of the cardiac muscle fibres. It is composed of two different walls: the inner one is the *visceral pericardium*, which is fixed to the heart wall, while the outer one is called the *parietal pericardium*, composed by inelastic connective tissue. Between these two layers, a pericardial fluid acts as a lubricant and allows the sliding of one wall over one other, with minimal friction,

when the heart is moving.

The outer wall of the heart consists of three different layers: the inner and outer one are called *endocardium* and *epicardium*, respectively, and they are thin layers mainly made of connective tissue. The middle and thickest layer is the *myocardium*, composed by muscle tissue and responsible for the contraction of the heart. The thickness of the myocardium varies in the four chambers according to function: the atria are tipically thin, because they only need to deliver blood to the adjacent ventricle, while the ventricles have a thick muscular structure as they need to pump blood over a greater distance. The right ventricle pumps the non-oxygenated blood to the lungs, while the left ventricle has a bigger workload as it pumps blood into the whole body, working against a greater resistance to blood flow: as a result, the left ventricular wall is considerably thicker. At the microstructural level, the myocardium is a very complex muscle: in the ventricles, the orientation of muscular fibres varies in a significant way from the endocardium to the epicardium, and this is a key feature that allows a proper contraction of the chamber.
We also point out that most of the physiological studies on the cardiac mechanics are often performed on the left ventricle alone, because it is the most important chamber of the heart, as it plays a key role during the systolic phase of the cardiac cycle; in this work, we follow the same approach.

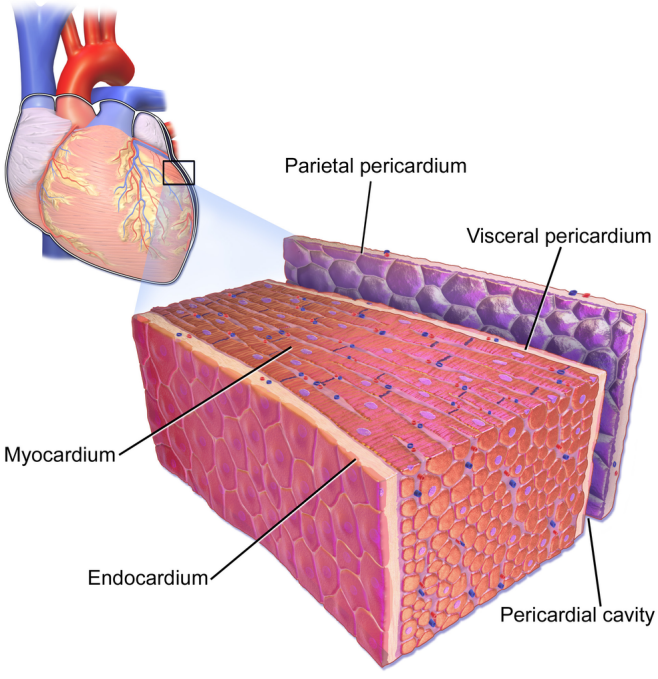

FIGURE 1.2: Structure of the heart wall. The pericardium consists of two thin walls, the parietal and visceral pericardium, separated by a small quantity of pericardial fluid which minimizes friction. The innermost layer, the endocardium, is a thin connective membrane; the thick muscular tissue, the myocardium, has a complex microstructure and is responsible for the contraction of the heart.

For the sake of simplicity, in the following we will often refer to the inner and outer layer of the myocardium as endocardium and epicardium, respectively, while they should properly called sub-endocardial and sub-epicardial portion of the myocardium: we carify here that we always refer to the muscular mass, ignoring the connective tissue around it.

1.2 Cardiac cycle

The heartbeat is triggered and controlled by electrical impulses, which are generated and conducted by specialized myocardial cells in different regions of the heart. The period of time between the activation trigger and the next beat is called a cardiac cycle, which can be divided in four main phase.
Focusing on the left side of the heart, during the passive filling phase, called *diastole*, the aortic valve is closed, while the mitral valve is open, allowing the blood to flow from the atrium to the ventricle: the myocardial wall of the ventricle is relaxed and the chamber

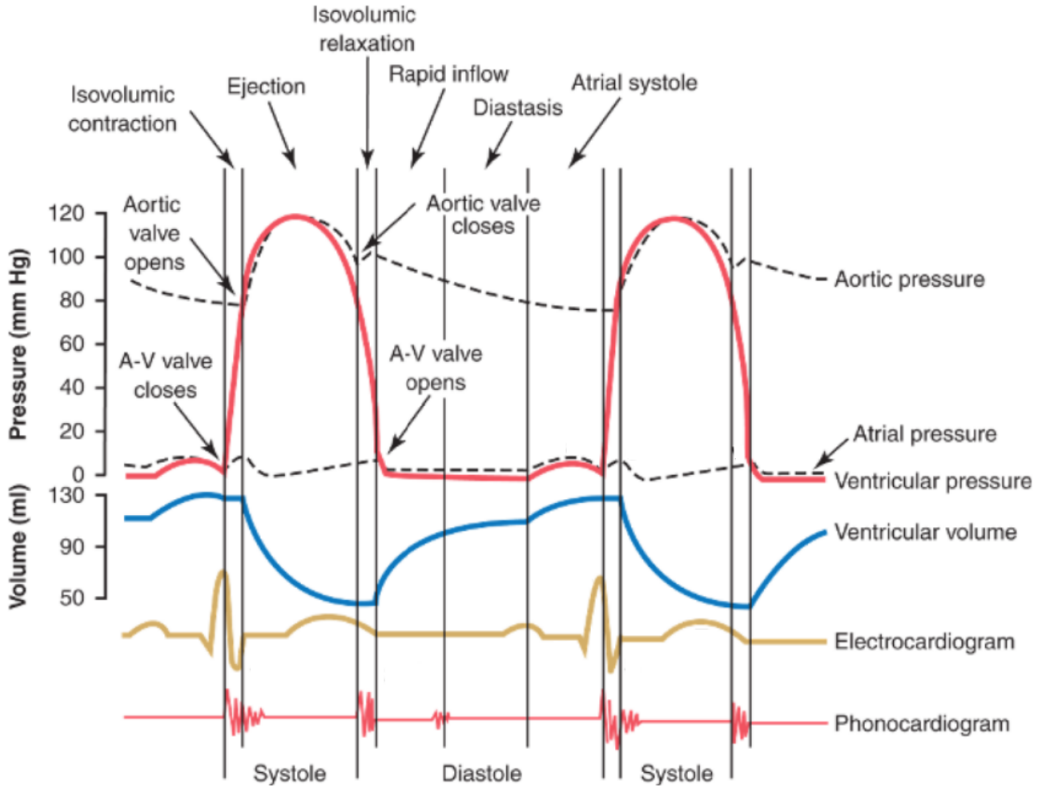

FIGURE 1.3: A complete visualization of the cardiac cycle, with plots for aortic, atrial and ventricular pressure and volume, electrocardiogram and phonocardiogram. A detailed division in phases and sub-phases is included, and the opening and closing of valves can be appreciated. As we can see, the aortic valve does not close immediately when the ventricular pressure becomes lower than the atrial pressure, and this is due to the inertial energy of the blood.

passively fills. When the maximum volume is reached, the aortic valve closes and the ventricle undergoes an *isochoric contraction*: the myocardial fibres begin their active role, starting contraction and slightly shortening the ventricle, while the inner volume of blood remains unchanged. Thus, ventricular pressure raises, until it becomes higher than the aortic pressure and the aortic valve is opened. As a consequence, the ejection phase, or *systole*, starts, and the blood is pumped through the arteries into the whole body thanks to the rapid ventricular contraction, triggered by an electric potential that dictates the shortening of myocardial fibres. When the inner pressure decreases, the aortic valve closes, and the myocardium relaxes, until the mitral valve is opened and a new diastolic phase starts, restarting the cycle.

An important tool for the analysis of the cardiac cycle is the *pressure-volume loop*, which is a plot of the left ventricular pressure versus the left ventricular volume during the whole cardiac cycle, and the enclosed area shows the work done by the myocardium and measures its efficiency. When the ventricle is filling, the pressure remains (almost) unchanged while the inner volume is constantly rising, thus we are moving along an horizontal line in the P-V plane; then, the mitral valve closes, and the isovolumic contraction sharply raises the inner pressure, triggering the opening of the aortic valve: this process is quite complex, because it depends on a number of factors, such as the geometry of the valve and the compliance of the arterial system. The minimum volume of the chamber is reached at the end of systole, when the aortic valve is closed; then, the ventricle undergoes an isochoric relaxation, decreasing pressure while the volume does not change: this phase is represented by a vertical line in the plot.

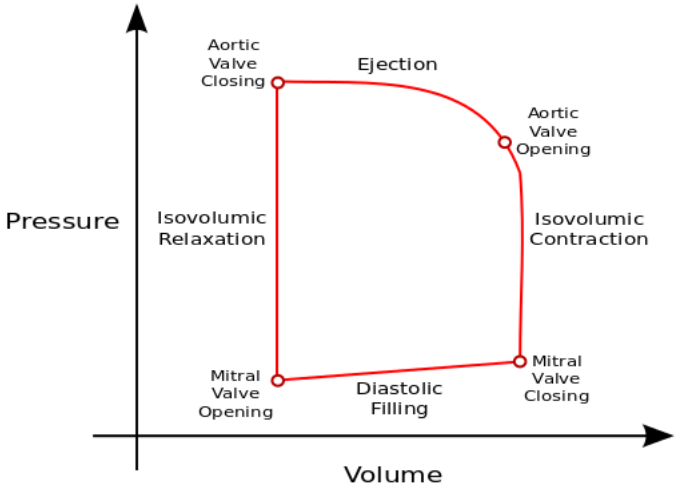

FIGURE 1.4: A schematic representation of the pressure-volume loop.

1.3 Microstructure of the heart

The heart is a quite complex muscle, composed of myocardial fibres which are organized into laminar structures, called sheets. The microstructure of the myocardium has an important role, as it greatly influences the electrophysiology and the mechanical behaviour of the heart. A proper understanding of the cardiac fibre architecture is a key element for the diagnosis and treatment of many cardiac pathologies: as a matter of fact, after a myocardial infarction there is a remodeling of the fibre and laminar structure, resulting in a less effective architecture from a mechanical point of view (Fedak et al. 2005, Helm et al. 2006).

The fibrous structure of the heart has been known for centuries: the first reference dates back to the year 1694, in the correspondence with the members of the royal society in London by the dutch tradesman and scientist Antonie van Leeuwenhoek; nevertheless, this kind of research has often been limited to histological studies. A recently developed technique, the diffusion tensor magnetic resonance imaging (DTMRI), allows the estimation of the diffusion tensor in biological tissues, and it could be the key for an accurate imaging of the cardiac muscle fibres: the eigenvectors of the locally measured diffusion tensor provide the direction of fibres and sheets, according to the magnitude of the eigenvalues. This technique is already widely used in other fields, such as brain imaging; for instance, using proper fibre-tracking algorithm it is possible to provide a three-dimensional high-quality visualization of the fibre field in the whole heart (Rhomer et al. 2007).

In this section, we analyse in detail the cardiac microstructure, providing a brief description of cardiac fibres and how they are organized. In addition, we also discuss the results of the most important research projects on this topic over the course of the last few decades.

1.3.1 Fibrous structure

The muscle tissue of the left ventricle is composed of muscle cells, called *myocytes*, which form three-dimensional muscular fibres. Myocytes are cylindrical cells 80 to 100 μm long with a radius that can vary between 5 and 12 μm; disc junctions link consecutive cells in order to guarantee the conduction of the electric signal along the fibres. Moreover, cardiac cells are embedded in an extracellular collagen matrix, which prevents overstretching, avoids muscle fibre rupture, and, in general, preserves the tissue architecture and the geometry of the chamber in case of large deformations. This extracellular network mainly comprises fibrillar collagens of type I, with a high tensile strength, and type III, which are highly deformable; it is composed of fibrils with a diameter between

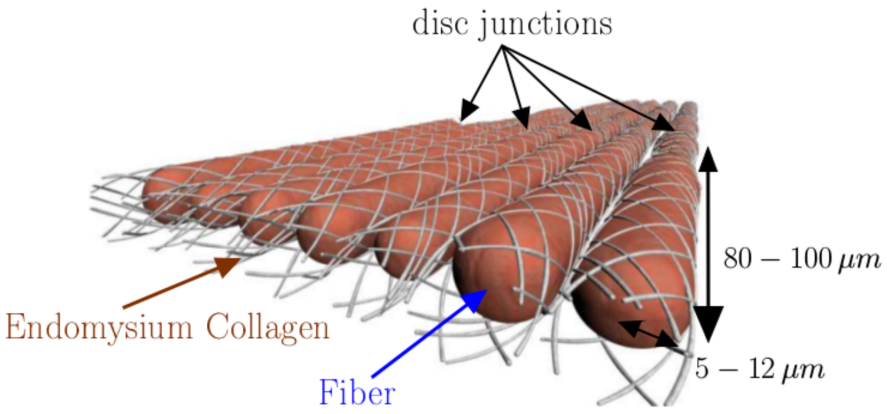

FIGURE 1.5: Fibrous structure and the endomysial collagen network (Rhomer et al. 2006).

120 and 150 nm, primarily aligned in the transverse direction with respect to the cardiac fibres. The collagen network linking two adjacent fibres, mainly consisting of type III collagen, is called *endomysium* (Rhomer et al. 2006). Figure 1.5 provides a detailed representation of the structure of cardiac fibres.

In the following, we focus on the fibre orientation in the left ventricle of a canine heart, which has been widely studied in the literature. Nevertheless, it is worth noting that the microstructure of an animal heart is not too different from the human myocardium: the biggest differences are the geometry and, obviously, dimesions, but the functioning of an healthy heart is similar in all biological species.

The geometry of the left-ventricular cavity can be approximated by a truncated ellipsoid, with a major axis about two times longer than the minor one. This is the most common geometry used for numerical simulations of ventricular mechanics, and a prolate coordinate system is often used.

The myocardial wall may be described as a well-ordered continuum of interconnecting muscle fibres; the spatial orientation of the fibres has a great impact on the ventricular mechanics, in particular on the distribution of stresses inside the wall (Streeter et al. 1969). In order to properly describe the microstructure of the myocardial tissue, we need to define two different angles that fully define the muscle fibre orientation inside the ventricular wall. The so-called *helix angle*, denoted by α_{helix}, is the angle between the local circumferential direction and the projection of the fibre path on the plane perpendicular to the local radial direction. For a complete description of the muscle fibre orientation which has been observed experimentally, the definition of a second angle is needed: the transverse angle α_{trans} is defined as the angle between the local circumferential direction

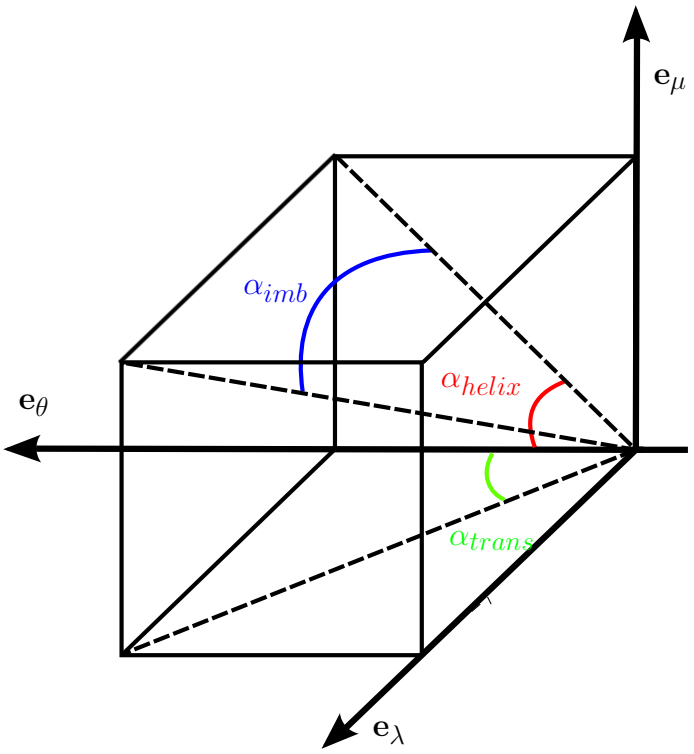

FIGURE 1.6: Definition of the fibre orientation. The versors $\mathbf{e}_\lambda$, $\mathbf{e}_\mu$ and $\mathbf{e}_\theta$ denote the radial, longitudinal and circumferential directions, respectively. The diagonal of the 3D shape denotes the hypotetical local fibre orientation, and the helix, transverse and imbrication angles are shown.

and the projection of the fibre path on the plane perpendicular to the local longitudinal direction (Bovendeerd et al. 1994). If $\alpha_{trans} \neq 0$, the fibre field has a radial component, which means that muscle fibres do not form a sequence radial layers, but they can be ingoing with respect to the ventricular wall, thus creating a more complex structure. In order to describe the fibre configuration in this case, the *imbrication angle* α_{imb} is often introduced: it is defined as the angle between the fibre path and the projection of the fibre path itself on the plane perpendicular to the local radial direction. Figure 1.6 provides a clear representation of the angles taken into account, and clearly shows that the fibre orientation can be fully defined by either the couple $(\alpha_{helix}, \alpha_{trans})$ or $(\alpha_{helix}, \alpha_{imb})$, the former being the most used in the literature (Colli Franzone et al. 1997). In Figure 1.7, a simple model of the complete ventricular microstructure can be appreciated.

In the past, several histological studies have been made in order to fully understand the structure of the myocardium: the most important feature of the muscle tissue is the variation of the helix angle between the sub-epicardial and the sub-endocardial layer of the ventricular wall. As a matter of fact, this is a key aspect in the myocardium mechanics, as it gives rise to ventricular torsion and greatly influences cardiac efficiency. Histological studies show that the helix angle varies from about $-60°$ at the sub-endocardium

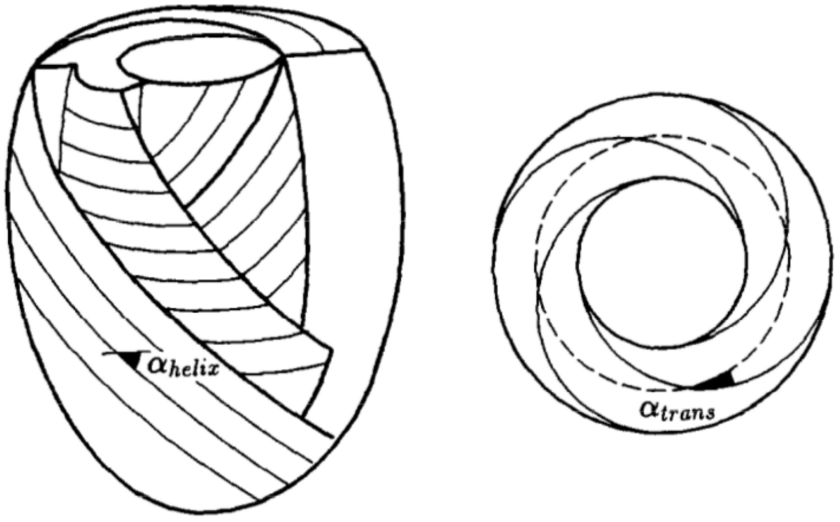

FIGURE 1.7: Fibre angles in the ventricular geometry. On the left, the helix angle α_{helix} is highlighted at the epicardium, while fibres are circumferential at the middle of the wall and have the opposite orientation near the endocardium. On the right, a basal view of the ventricle clearly shows the fibre path and the transverse angle α_{trans}, which is positive at the base, thus representing ingoing fibres (Bovendeerd et al. 1994).

to $+60°$ at the sub-epicardium, where the sign may change depending on the convention used and zero degrees correspond to the circumferential direction. Nevertheless, the nature of the variation of the fibre angle *inside* the myocardium is a very debated sudject: several different results of physiological studies have been reported, and at the same time several different fibre configurations have been used for numerical simulations. A detailed analysis of the mechanical impact of a different helix angle variation inside the ventricular wall is one of the main purposes of this work, and we will show that a different fibre field can greatly affect the ventricular mechanics (see Chapter 3 for details).

One of the most important papers reporting histological studies of the ventricular microstructure dates back to 1969: Daniel D. Streeter determined the fibre orientation in specimens obtained from 18 dog hearts both in diastole and systole. He managed to highlight a continuous distribution with no discrete fibre bundles, with helix angle changing smoothly from about $-90°$ at the endocardium to $+80°$ at the epicardium; nevertheless, he reported that the greatest variation in the fibre angle occurs in the immediate proximity of the endocardial and epicardial surfaces, while the change is almost linear at the middle of the myocardial wall. Thus, he concluded that considering a variation of angle between $-60°$ and $+60°$ is acceptable. Moreover, Streeter stated that almost 90% of the fibres are oriented circumferentially, with an helix angle between -22,5 and 22,5 degrees, while only a small portion of fibres is oriented longitudinally, lying in the sub-endocardial and sub-epicardial layers. In addition, he compared the data obtained from hearts rapidly fixed in situ during systole and diastole, and no significant differences

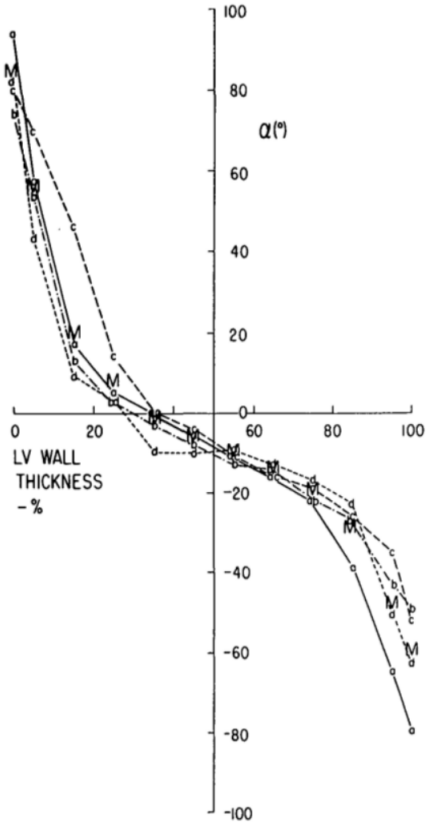

FIGURE 1.8: Original graph for fibre angle distribution from Streeter's histological studies. α denotes the helix angle, with an opposite sign with respect to our definition of α_{helix}; 0% and 100% wall thickness denote the sub-endocardium and the sub-epicardium, respectively. Data taken at four different sampling sites are plotted. The rapid change in angle is evident in the sub-endocardium and in the sub-endocardium, and we point out that at the middle of the myocardial wall the angle is not zero, which means that midwall fibres are not circumferential. (Streeter et al. 1969).

in fibre orientations were reported, despite of a 28% thickening of the ventricular wall at systole.

In the last decades, the DTMRI (Diffusion Tensor Magnetic Resonance Imaging) technology has allowed more accurate studies for fibre tracking, performed in vivo and in a non-invasive way, providing a full three-dimensional representation of the fibre field. This technique is based on the measuring of the random motion of hydrogen atoms in water molecules, due to the effect of diffusion of the fluid; in biological tissues with a fibrous nature, such as skeletal muscle, brain white matter, or, in our case, the myocardium, water diffuses faster in the direction of the fibres. Thus, using proper fibre tracking algorithm, it is possible to reproduce the correct distribution of fibres inside the myocardial wall of the whole cardiac muscle. Exploiting this technique, an outstanding research project has been presented by Rohmer, Sitek & Gullberg in 2006, in which they

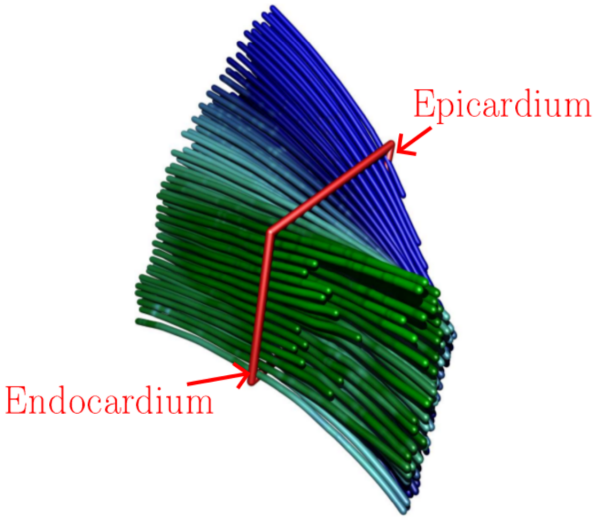

FIGURE 1.9: Variation of the helix angle across the ventricular wall. (Rohmer et al. 2006).

provided an accurate visualization for the whole fibre configuration of the human heart: some high-quality representation from their work can be appreciated in Figures 1.9-1.11. Remarking the extreme complexity of the cardiac microstructure, they confirmed that the fibre orientation rapidly changes near the inner and outer wall of the myocardium, thus agreeing with Streeter's results. In addition, they pointed out that the fibre angle is homogeneous from apex to base, with no significant changes in the longitudinal direction:

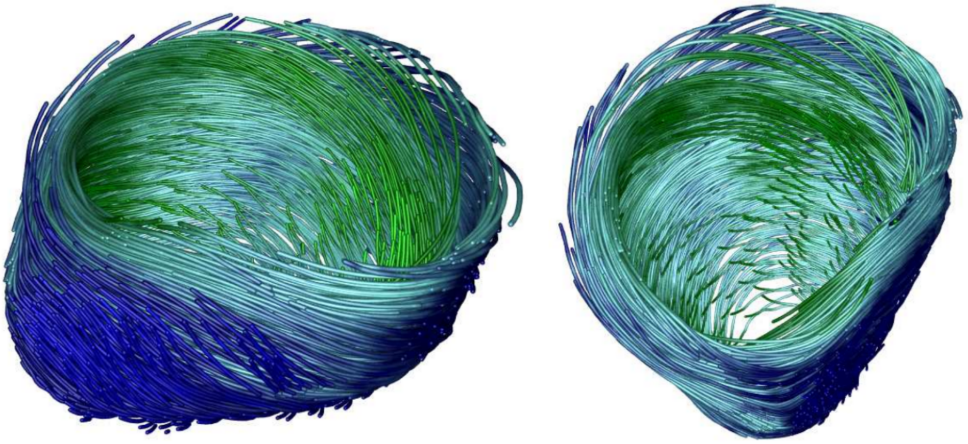

FIGURE 1.10: Visualization of the left ventricular fibre structure. Different colours refer to a different helix angle, and the clockwise to counterclockwise orientation of the fibres from the epicardium to the endocardium can be appreciated. In the visualization on the left, the front wall is the septum, while in the right picture the posterior wall is on the bottom (Rohmer et al. 2006).

as a matter of fact, this assumption is made in most numerical simulations for cardiac mechanics. Last but not least, the authors claim that considering a linear variation of the helix angle between the endocardium and the epicardium is a very rough approximation, and a more accurate model is needed (Rhomer et al. 2006). Nevertheless, their paper does not investigate the nature and the mechanical impact of the transverse angle of the helical network of fibres.

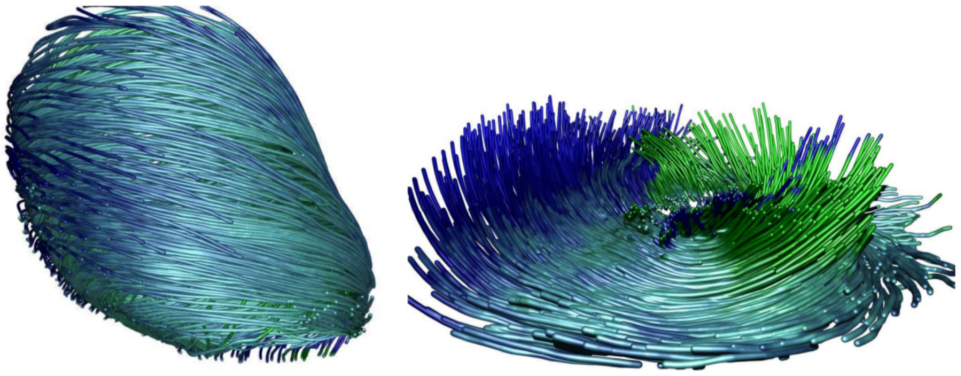

FIGURE 1.11: On the left, an apex-to-base visualization of the fibre structure at the epicardium shows the homegeneity of the fibre orientation. On the right, a representation of the fibre field in proximity of the apex: the twist of the field and the fast change from clockwise to counterclockwise rotation can be appreciated (Rohmer et al. 2006).

In order to properly understand the relationship between myofibre orientation and ventricular mechanics, in particular wall strain, we consider a simplified model of the left ventricle, consisting of a thick-walled cylinder, thus avoiding the complexity of the microstructure in proximity of the apex. In particular, we simply consider the mechanical influence of fibres in the sub-endocardial and sub-epicardial layers, in order to show the importance of their clockwise or counterclockwise orientation. In this way, we are ignoring the myocardial fibres in the proximity of the middle of the wall, which are mostly oriented circumferentially and thus contribute to circumferential strain. On the other hand, fibres with an oblique orientation exert a torque on the ventricular wall, thus contributing to circumferential-radial shear: when activation occurs, sub-endocardial fibres shorten, inducing a clockwise apical rotation (in an apex-to-base view). In contrast, myofibres in the sub-epicardial layer also shorten, causing a counterclockwise rotation at the apex: these opposite effects result in a transmural shear load, which is compensated by shear deformation of the tissue between the two layers. If there is no transverse angle of the fibre, which means $\alpha_{trans} = 0$, the shear load can only be counteracted by the

passive cardiac tissue: mechanical equilibrium is reached only for large circumferential-radial shear strains, because of the low stiffness of the tissue in the radial direction, as fibres are oriented circumferentially. On the contrary, if $\alpha_{trans} \neq 0$, the myofibres that cross over between the inner and outer layer actively participate in the transmission of the shear load, so that the shear deformation is reduced thanks to the higher stiffness of the fibrous structure. Figure 1.12 provides a schematic representation of this argument (Ubbink et al. 2006). Nevertheless, we point out that this is a theoretical and simplified argument: some research studies show that this behaviour does not match the physiological evidence, as the endocardial and epicardial surfaces should both rotate in the same direction. In addition, it has been found that the basal rotation is greater at the endocardium than the epicardium: this is apparently a mechanical paradox, since sub-endocardial fibres should reduce the shear towards the sub-endocardium, not increase it. One possible explanation for this mechanical fact may be that the transverse angle of cardiac fibres can transmit epicardial forces more effectively to the endocardium (Young et al. 2012).

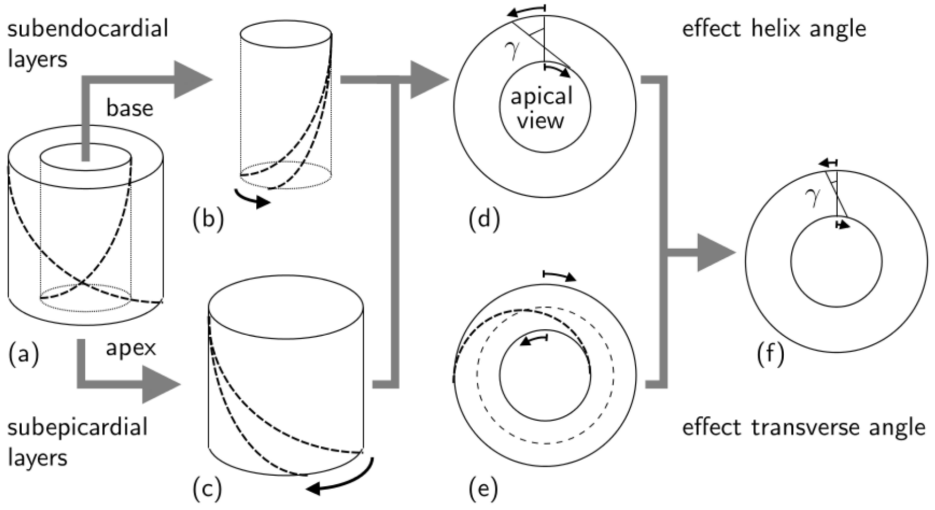

FIGURE 1.12: Influence of helix and transverse angles on the ventricular mechanics, in particular transmural shear, using a simplified model of the left ventricle. Suppose first that the transverse angle is null: thanks to the different orientation of fibres in the inner and outer layers of the ventricular wall (a), the shortening of myofibres causes a clockwise apical rotation of the sub-endocardium (b) and a counterclockwise rotation of the sub-epicardium (c), when viewing from apex to base; the combination of this effects results in a positive circumferential-radial shear, denoted by the shear angle γ (d). If the transverse angle is not null (e), the orientation of fibres between the inner and outer layer causes an additional negative circumferential-radial shear, thus reducing the total shear at the apex (Ubbink et al. 2006).

1.3.2 Laminar structure

In the myocardium, muscle fibres are organized and aligned into three-dimensional structures, called sheets, which are three to four cells thick; this laminar structure is oriented transversally to the heart wall. The orientation of sheets varies spatially inside the myocardium, forming a complex structure, with sheets that can be assimilated to twisted surfaces stacked from apex to base.

From the physiological point of view, the sheets are physically separated by the *perimysium*, a coiled bundle of collagen fibrils, which are oriented parallel to the long axis of the myocytes and mainly consisting of type I collagen, with an high tensile strength; additionally, a network of extracellular collagen fibres provides tight coupling of myocytes within the sheet.

In order to properly define the local geometry of the cleavage plane between the laminae, we denote by $\mathbf{e}_n$ the unit vector normal to the sheet, and we consider the orthonormal basis $(\mathbf{e}_f, \mathbf{e}_s, \mathbf{e}_n)$, where $\mathbf{e}_f$ denotes the fibre direction and $\mathbf{e}_s$ is perpendicular to the myocyte lying into the sheet plan. Consequently, we define the sheet angle β as the angle between $\mathbf{e}_r$ (the radial unit vector) and $\mathbf{e}_s$ (see Figure 1.13). Histological studies show that this angle varies across the myocardial wall, approximately from $+45°$ at the endocardium to $-80°$ at the epicardium, and the distribution also changes from the apical to the basal region (Costa et al. 1999, Rhomer et al. 2006).

The use of histological methods for the reconstruction of the laminar structure of the myocardium is a challenging task, but new technological tools, such as the previously

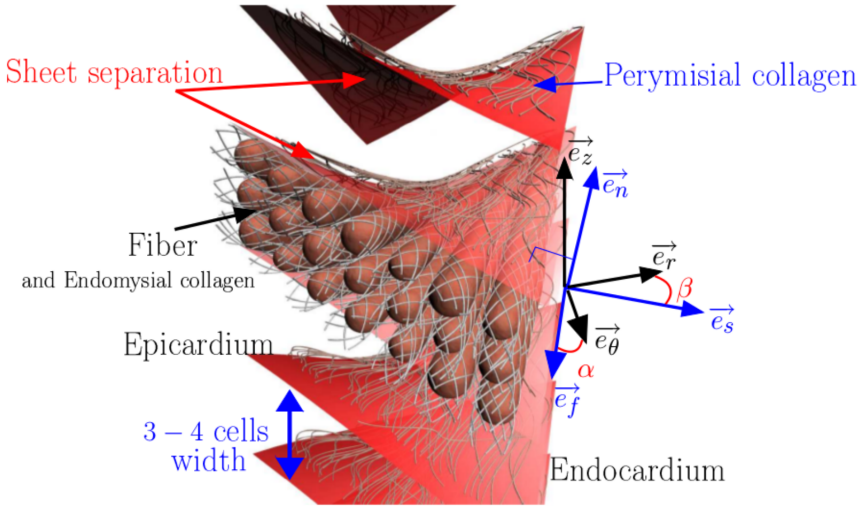

FIGURE 1.13: Laminar structure of the myocardial wall. $(\mathbf{e}_r, \mathbf{e}_\theta, \mathbf{e}_z)$ is the basis for the ventricular geometry, with versors denoting the radial, circumferential and longitudinal direction, respectively; $(\mathbf{e}_f, \mathbf{e}_s, \mathbf{e}_n)$ is the microstructural basis. Helix angle α and sheet angle β are shown. (Rhomer et al. 2006).

mentioned DTMRI, allows for an accurate reconstruction of the sheet structures of the cardiac wall. The representation of the laminar structure is quite complex, because it requires the identification of a surface instead of a line in the case of fibres: for each position in the ventricular wall, it is necessary to find the plane tangent to the sheet. Once again, thanks to the outstanding research project by Rohmer et al. (2006), a high-quality visualization of the laminar structure of the heart is available. The representation of detected planes is consistent with histological measurements, with sheets mainly going across the wall. The structures in the region near the apex have interesting features, including a bigger curvature due to the twisting pattern of fibres.

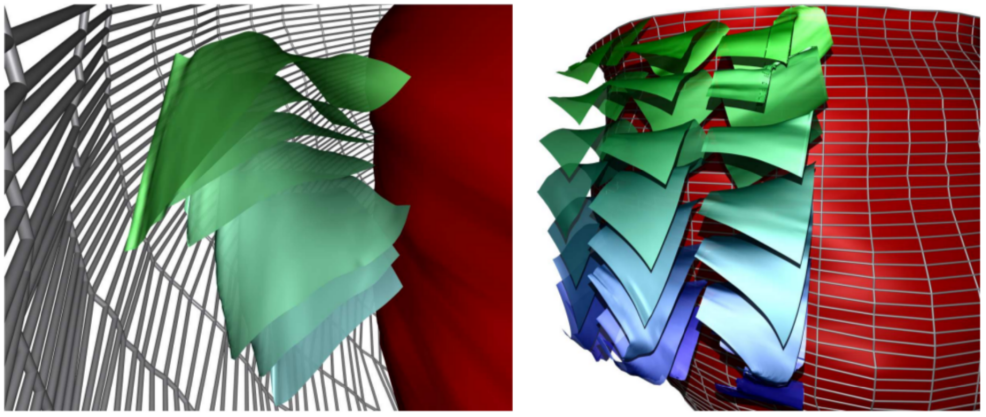

FIGURE 1.14: Sheets reconstruction in the left ventricular wall. On the left, the stacked laminar structure, oriented across the wall, are clearly visible. The red surface is the endocardium, while the epicardium is delimited by the mesh. On the left, a lateral view of the wall microstructure is shown: the global twisting movement across the wall can be appreciated, as well as the variation of the normal orientation of sheets from apex to base (Rohmer et al. 2006).

1.4 Analysis of the ventricular performance

The brief physiological introduction provided above clearly shows the complexity of the left ventricle, both from the structural and functional point of view. In this section, we focus on some mechanical and physiological features that can be used to study the proper functioning of the ventricle. We introduce a set of indicators that can be used in two different ways: first of all, they have a direct clinical application, as they are often used for the identification of cardiac pathologies, such as ischemia or ipertrophy. On the other hand, from the numerical viewpoint, these quantities can be easily calculated during the post-processing step of a numerical simulation, and then compared with real,

physiological values obtained experimentally, in order to determine the suitability of the theoretical model and the numerical method used.
Therefore, we introduce the following set of *physiological indicators*:

- the *stroke volume* is the volume of blood ejected during the systolic phase and it can be computed as the difference between the end-diastolic and the end-systolic volume of the ventricular chamber. Obviously, it can greatly change depending on the size and geometry of the ventricle: the average healthy human heart has a stroke volume around 70 ml, while in the canine ventricle it can be between 20 and 25 ml;

- the *ejection fraction* is the percent of blood pumped by the ventricle during the cardiac cycle, computed as the stroke volume to end-diastolic volume ratio, thus being independent on the heart size. It is a very important quantity that measures the efficiency of the myocardium: a healthy ventricle should have an average ejection fraction above 50%. A lower ejection fraction may reveal the presence of cardiac pathologies, such as damages to the myocardium caused by infarction or atrial fibrillation;

- *cardiac wall thickening* during the systolic phase is another physiological indicator, and it can vary from apex to base. Through histological studies of dog hearts, Streeter and co-workers found a 28% thicker wall during systole (Streeter et al., 1969); for the human heart, data obtained with cardiac magnetic resonance show that the thickening of the wall increases going from base to apex (Conti et al. 2011);

- the *longitudinal shortening* of the ventricle can be measured as the distance between the basal plane and either the apex (on the epicardial surface) or the point of the endocardium farthest from the base, thus effectively measuring the shortening of the ventricular chamber; in a healthy heart, shortening should be close to 20% (Conti et al. 2011) . We also point out that, as the heart tissue is nearly incompressible, ventricular shortening correlates with wall thickening;

- the *ratio between the length of the ventricle and the basal epicardial radius* should be taken into account for numerical models: based on the physiological evidence, this quantity should remain almost constant during the whole cardiac cycle, and we will take care of checking this fact in the numerical simulations performed;

- *left ventricular torsion* is the twisting motion of the ventricle around its long axis, induced by the contraction of the myofibres in the cardiac wall. During the isochoric contraction, both the base and the apex rotate counterclockwise, when viewed from

the apex; in the systolic phase, the base changes its motion and moves clockwise, while the apex continues its counterclockwise rotation. This process stores potential elastic energy in the collagen matrix, and its release causes a rapid untwisting during diastole, which facilitates rapid filling (Russel et al., 2009). Left ventricular torsion can be easily computed by non-invasive imaging techniques, such as CMR (cardiovascular magnetic resonance) tissue tagging or echocardiographic speckle tracking. In the literature, different methods have been used to characterize the torsion of the ventricle: it has been calculated as a relative rotation (degrees), a rotation per length (degrees/mm), a torsional shear angle (degrees) or a shear strain (dimensionless). As a matter of fact, if torsion is computed as the difference in rotation between the apex and the base, problems may arise because it does not take into account the ventricular dimension, in particular its apex-to-base distance. A good example of a proper torsion measurement is provided in Figure 1.15, where the torsional shear angle θ_{CL} is computed: it is a measure of the change in angle between line segments which are initially aligned with the anatomical circumferential and longitudinal axes of the left ventricle. This measurement is independent of ventricular size and can be computed not only between apex and base, but also between any two given slices (Young et al. 2012). Alternatively, torsional shear angle can be computed from axial and shear strains with the following formula

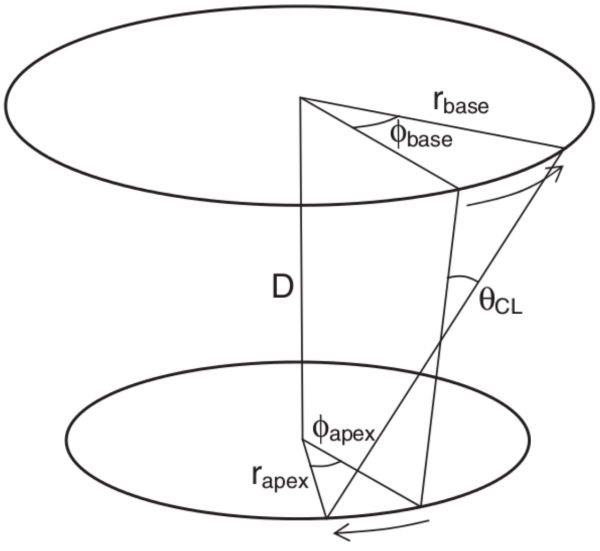

FIGURE 1.15: Computation of torsional shear angle θ_{CL}. D is the distance between the two chosen slices, one near the base and one near the apex, r_{base} and r_{apex} denote the basal and apical radius (taken at the endocardium, at the epicardium or at midwall) while Φ_{base} and Φ_{apex} denote the change in angle with respect to a reference configuration. (Young et al. 2012).

(Russel et al. 2009):

$$\sin\theta_{CL} = \frac{2E_{CL}}{\sqrt{1+2E_{CC}}\,\sqrt{1+2E_{LL}}}$$

where E_{CC} is the circumferential axial strain, E_{LL} is the longitudinal axial strain, and E_{CL} is the circumferential-longitudinal shear. In contrast, one can directly calculate the difference in circumferential displacement:

$$\theta_{CL} = \frac{\phi_{apex} r_{apex} - \phi_{base} r_{base}}{D} \quad .$$

The last two options are perfectly viable, and in our work we will refer to the torsion computed with the second formula. Based on this definition, physiological studies show that the torsion in the healthy left ventricle should be around 10°.

There are several other quantities that can be taken into account for the mechanical study of a healthy left ventricle: for instance, local mechanics can be quantified in terms of deformation and stress. The measuring of local deformation and wall stress has several experimental limitations, but axial and shear strains are key elements for the analysis of a numerical model for ventricular mechanics.

CHAPTER 2

VENTRICULAR MECHANICS

Introduction

In this chapter, we focus on the numerical implementation of a proper mechanical model, which accounts for both the passive properties of the cardiac tissue and the active behaviour of muscle fibres. First, we recall the basis of the classical framework of continuum mechanics, highlighting the main mathematical features that will be used in this work. Next, we present a theoretical model for the passive myocardium, based on Holzapfel and Ogden's work (2009): the cardiac muscle can be described as an inhomogeneous, hyperelastic, orthotropic material, characterized by a complex microstructure that is encoded in the mathematical model. In addition, a proper modelling of the active behaviour of muscle fibres is proposed: both the active stress and the active strain approaches are presented. Next, we introduce an adequate numerical framework for the approximation of the pressure-volume loop, which leads to a non-linear saddle-point problem which can be solved using Newton's linearisation method. The geometrical setting is defined thanks to the use of the prolate coordinate system, which allows for an easy definition of the fibre and sheet orientation. Finally, we discuss the results of a preliminary numerical simulation, focusing on the computed values for the most relevant physiological quantities and on the analysis of the distribution of strain and stress in the ventricular wall.

2.1 Notation and mechanical background

In the continuum mechanics framework, a *configuration* of a continuum body $\mathfrak{B}$ is defined as a function $\chi : \mathbb{R}^3 \subseteq \mathfrak{B} \to \mathbb{R}^3$. We consider a given *reference configuration* χ_0 and an *actual configuration* χ: the reference and actual placements of the body in $\mathbb{R}^3$ are defined as $\Omega_0 := \chi_0(\mathfrak{B})$ and $\Omega := \chi(\mathfrak{B})$, respectively. Thus, given a point $\mathfrak{p} \in \mathfrak{B}$, its placement is $\mathbf{X} = \chi_0(\mathfrak{p})$ in the reference configuration and $\mathbf{x} = \chi(\mathfrak{p})$ in the actual configuration.
A *deformation* is a map from the reference to the actual configuration, which means a map $\boldsymbol{\varphi}$ such that

$$\boldsymbol{\varphi} : \Omega_0 \ni \mathbf{X} \to \mathbf{x} = \chi(\chi_0^{-1}(\mathbf{X})) \in \Omega \ , \quad \boldsymbol{\varphi} = \chi \circ \chi_0^{-1}$$

Assuming that $\boldsymbol{\varphi}$ is a diffeomorphism from Ω_0 to Ω, we can define the *deformation gradient tensor*:

$$\mathsf{F}(\mathbf{X}) := \frac{\partial \boldsymbol{\varphi}}{\partial \mathbf{X}} \ .$$

Denoting by $\mathrm{Lin}(\mathbb{R}^3)$ the vector space of linear transformations from $\mathbb{R}^3$ to $\mathbb{R}^3$, we define the following subsets:

$$\begin{aligned}
\mathrm{Lin}^+(\mathbb{R}^3) &= \Big\{ \ \mathsf{F} \in \mathrm{Lin}(\mathbb{R}^3) : \det\mathsf{F} > 0 \ \Big\}, \\
\mathrm{Sym}^+(\mathbb{R}^3) &= \Big\{ \ \mathsf{C} \in \mathrm{Lin}^+(\mathbb{R}^3) : \mathsf{C}^\mathsf{T} = \mathsf{C} \ \Big\}, \\
\mathrm{Orth}^+(\mathbb{R}^3) &= \Big\{ \ \mathsf{Q} \in \mathrm{Lin}(\mathbb{R}^3) : \mathsf{Q}^{-1} = \mathsf{Q}^\mathsf{T} \Big\}.
\end{aligned}$$

A configuration is *admissible* if $\mathsf{F} \in \mathrm{Lin}^+(\mathbb{R}^3)$, which means that the determinant of the deformation gradient tensor $J := \det\mathsf{F}$ is strictly positive.
Let us consider two open subsets of the boundary Ω_0 (with respect to the induced topology), $\partial_D\Omega_0$ and $\partial_N\Omega_0$, on which essential and natural boundary condition are applied, respectively. We require that

$$\partial\Omega_0 = \overline{\partial_D\Omega_0 \cup \partial_N\Omega_0} \quad \text{and} \quad \partial_D\Omega_0 \cap \partial_N\Omega_0 = \emptyset \ .$$

Then, if $\mathbf{g}(\mathbf{X})$ is a given displacement on $\partial_D\Omega_0$, the set of admissible configurations is defined as

$$\mathcal{C} = \Big\{ \boldsymbol{\varphi} : \Omega_0 \to \Omega : \mathsf{F} \in \mathrm{Lin}^+ \text{ and } \boldsymbol{\varphi}|_{\partial_D\Omega_0} = \mathbf{g} \Big\} \ .$$

The *Cauchy stress tensor* T describes the stress state of the body in the deformed configuration. We also define the following tensors:

- *left Cauchy-Green strain tensor* $\mathsf{B} := \mathsf{F}\mathsf{F}^\mathsf{T}$;

- *right Cauchy-Green strain tensor* $\mathsf{C} := \mathsf{F}^{\mathsf{T}}\mathsf{F}$;
- *Green-Lagrange strain tensor* $\mathsf{E} := \frac{1}{2}(\mathsf{C} - \mathsf{I})$;
- *first Piola-Kirchhoff tensor* $\mathsf{P} := J\mathsf{T}\mathsf{F}^{-\mathsf{T}}$;
- *second Piola-Kirchhoff tensor* $\mathsf{S} := \mathsf{F}^{-1}\mathsf{P} = J\mathsf{F}^{-1}\mathsf{T}\mathsf{F}^{-\mathsf{T}}$;

The relationship between the stress T and the strain F is given by the constitutive model of the material at hand. In our case, we consider a *hyperelastic material*, also called *Green elastic material*: the stress-strain relationship for this category of materials derives from a *strain energy density function*. Thus, there exists a function $\mathcal{W} : \Omega_0 \times \mathrm{Lin}^+ \to \mathbb{R}$ such that

$$\mathsf{P} = \frac{\partial \mathcal{W}}{\partial \mathsf{F}} , \quad \text{or equivalently} \quad \mathsf{S} = 2\frac{\partial \widehat{\mathcal{W}}}{\partial \mathsf{C}} , \tag{2.1}$$

where $\widehat{\mathcal{W}}(\mathbf{X}, \mathsf{C}) = \widehat{\mathcal{W}}(\mathbf{X}, \mathsf{F}^{\mathsf{T}}\mathsf{F}) = \mathcal{W}(\mathbf{X}, \mathsf{Q}\mathsf{F})$. We require the objectivity of the strain energy density function, which means

$$\mathcal{W}(\mathbf{X}, \mathsf{F}) = \mathcal{W}(\mathbf{X}, \mathsf{Q}\mathsf{F}) \quad \text{for all } \mathsf{Q} \in \mathrm{Orth}(\mathbb{R}^3) .$$

Thanks to the *polar decomposition theorem*, it is known that there always exist two tensors $\mathsf{R} \in \mathrm{Orth}(\mathbb{R}^3)$ and U unitary such that $\mathsf{F} = \mathsf{R}\mathsf{U}$ and this decomposition is unique. Thus, requiring the frame invariance of $\mathcal{W}$ is equivalent to state that $\mathcal{W}$ depends on F only through U. Exploiting the polar decomposition, we have

$$\mathsf{C} = \mathsf{F}^{\mathsf{T}}\mathsf{F} = \mathsf{U}^{\mathsf{T}}\mathsf{R}^{\mathsf{T}}\mathsf{R}\mathsf{U} = \mathsf{U}^{\mathsf{T}}\mathsf{U} ,$$

which means that the strain energy density function $\widehat{\mathcal{W}}(\mathbf{X}, \mathsf{C})$ automatically satisfies the objectivity requirement.

In this framework, we consider a hyperelastic material with strain-energy density function $\widehat{\mathcal{W}}(\mathbf{X}, \mathsf{C})$, and we suppose that, for a fixed point $\mathbf{X} \in \Omega_0$,

$$\widehat{\mathcal{W}}(\mathsf{C}) = \widehat{\mathcal{W}}(\mathsf{Q}\mathsf{C}\mathsf{Q}^{\mathsf{T}}) \quad \text{for all } \mathsf{Q} \in \mathcal{G} \subseteq \mathrm{Orth}(\mathbb{R}^3) ,$$

which means that the local invariance property must be satisfied: the strain energy is the same under the change of the reference configuration through the rotation Q, for any given deformation C. If $\mathcal{G} \equiv \mathrm{Orth}(\mathbb{R}^3)$ the material is *isotropic*, which means that its elastic response is the same for every possible $\mathsf{Q} \in \mathrm{Orth}(\mathbb{R}^3)$; on the other hand, if $\mathcal{G}$ is a proper subgroup of $\mathrm{Orth}(\mathbb{R}^3)$ the material is called *anisotropic*.
A generic scalar function of p scalar fields, n vector fields and m tensor fields $\Psi(s_1, ..., s_p,$

$\mathbf{v}_1, ..., \mathbf{v}_n, \mathsf{A}_1, ..., \mathsf{A}_m)$ is said isotropic with respect to these fields if, for every $\mathsf{Q} \in \mathrm{Orth}(\mathbb{R}^3)$,

$$\Psi(s_1, ..., s_p, \mathbf{v}_1, ..., \mathbf{v}_n, \mathsf{A}_1, ..., \mathsf{A}_m) = \psi(s_1, ..., s_p, \mathsf{Q}\mathbf{v}_1, ..., \mathsf{Q}\mathbf{v}_n, \mathsf{Q}\mathsf{A}_1\mathsf{Q}^\mathsf{T}, ..., \mathsf{Q}\mathsf{A}_m)\mathsf{Q}^\mathsf{T} \ .$$

If a function Ψ is invariant with respect to a group

$$\mathcal{H} = \left\{ \mathsf{Q} \in \mathrm{Orth}(\mathbb{R}^3) : \mathsf{Q}\mathbf{v}_i = \mathbf{v}_i \text{ for } i \in \{1, ..., n\}, \ \mathsf{Q}\mathsf{A}_j\mathsf{Q}^\mathsf{T} = \mathsf{A}_j \text{ for } j \in \{1, ..., m\} \right\} \ ,$$

then it always exists an *isotropic representation* of the function Ψ encoding for the invariant group $\mathcal{H}$, which is a function $\widetilde{\Psi}$ of the fields $\mathbf{v}_i$, A_j, s_k, and of the arguments of Ψ, such that $\Psi = \widetilde{\Psi}$.
Thanks to the *spectral theorem*, if a scalar function $\Psi(\mathsf{A})$ of a symmetric matrix A is isotropic, then $\Psi(\mathsf{A}) = \Psi(\mathsf{B})$, where B is a matrix similar to A, which means $\mathsf{B} = \mathsf{P}^{-1}\mathsf{A}\mathsf{P}$ for an invertible change of basis matrix P. Thus, Ψ depends on A only through its eigenvalues, or, in a more general way, it depends only on a set of scalar functions of its eigenvalues: this set is called *invariant set* and it is denoted by the symbol Υ. The invariant set is *irreducible* if it is the smallest one that represents the function Ψ.
Moreover, we introduce an orthonormal ternary $\{\mathbf{f}_0, \mathbf{s}_0, \mathbf{n}_0\}$ in the reference configuration; a material is called *orthotropic* if the strain energy is invariant with respect to rotations around any versor of the triplet. Thus, the material symmetry group is

$$\mathcal{G}_{\mathrm{orth}} = \left\{ \mathsf{Q} \in \mathrm{Orth}(\mathbb{R}^3) : \mathsf{Q}(\mathbf{m} \otimes \mathbf{m})\mathsf{Q}^\mathsf{T} = \mathbf{m} \otimes \mathbf{m}, \text{ for } \mathbf{m} \in \{\mathbf{f}_0, \mathbf{s}_0, \mathbf{n}_0\} \right\} \ .$$

If the strain energy density function $\widehat{\mathcal{W}}(\mathsf{C})$ is invariant with respect to the set $\mathcal{G}_{\mathrm{orth}}$, then, thanks to our previous results, there exists a representation $\widehat{\mathcal{W}}_{\mathrm{orth}}(\mathsf{C})$ such that

$$\widehat{\mathcal{W}}(\mathsf{C}) = \widehat{\mathcal{W}}_{\mathrm{orth}}(\mathsf{C}, \mathbf{f}_0 \otimes \mathbf{f}_0, \mathbf{s}_0 \otimes \mathbf{s}_0, \mathbf{n}_0 \otimes \mathbf{n}_0) \ ,$$

for any $\mathsf{C} \in \mathrm{Sym}^+(\mathbb{R}^3)$, where the function $\widetilde{\mathcal{W}}_{\mathrm{orth}}$ is isotropic with respect to its arguments. We point out that the dependence on $\mathbf{n}_0 \otimes \mathbf{n}_0$ is redundant, as it is obvious that

$$\mathbf{f}_0 \otimes \mathbf{f}_0 + \mathbf{s}_0 \otimes \mathbf{s}_0 + \mathbf{n}_0 \otimes \mathbf{n}_0 = \mathsf{I} \ .$$

The invariant set for an orthotropic material is defined as follows:

$$\Upsilon_{\mathrm{Orth}} = \left\{ \mathrm{tr}\mathsf{C}, \mathrm{tr}\mathsf{C}^2, \mathrm{tr}\mathsf{C}^3, \mathbf{f}_0 \cdot \mathsf{C}\mathbf{f}_0, \mathbf{s}_0 \cdot \mathsf{C}\mathbf{s}_0, \mathbf{f}_0 \cdot \mathsf{C}^2\mathbf{f}_0, \mathbf{s}_0 \cdot \mathsf{C}^2\mathbf{s}_0 \right\} \ .$$

It is possibile to prove that this set is not irreducible, as only six of these seven invariants are independent. As a side note, if $\mathbf{f}_0$ and $\mathbf{s}_0$ are not orthogonal, it is necessary to consider two additional invariants, $(\mathbf{f}_0 \cdot \mathbf{s}_0)\mathbf{f}_0 \cdot \mathsf{C}\mathbf{s}_0$ and $(\mathbf{f}_0 \cdot \mathbf{s}_0)^2$ to take into account the angle

between $\mathbf{f}_0$ and $\mathbf{s}_0$ in the actual and in the reference configuration.

On the other hand, a *transversely isotropic* material is invariant for any rotation around a given vector (for example, $\mathbf{f}_0$), thus we define the material symmetry group

$$\mathcal{G}_{\text{tr}} = \left\{ \mathsf{Q} \in \text{Orth}(\mathbb{R}^3) : \mathsf{Q}\mathbf{f}_0 = \mathbf{f}_0 \right\} .$$

In this case, if the function $\widehat{\mathcal{W}}(\mathsf{C})$ is invariant with respect to $\mathcal{G}_{\text{orth}}$, we can define a transversely isotropic version of the strain energy function. As a consequence, we can define a function $\widehat{\mathcal{W}}_{\text{tr}}$ such that

$$\widehat{\mathcal{W}}(\mathsf{C}) = \widehat{\mathcal{W}}_{\text{tr}}(\mathsf{C}, \mathbf{f}_0)$$

and we can define the set of invariants

$$\Upsilon_{\text{Orth}} = \left\{ \text{tr}\mathsf{C}, \text{tr}\mathsf{C}^2, \text{tr}\mathsf{C}^3, \mathbf{f}_0 \cdot \mathsf{C}\mathbf{f}_0, \mathbf{f}_0 \cdot \mathsf{C}^2\mathbf{f}_0 \right\} .$$

2.2 Holzapfel-Ogden model

Let $\mathbf{a}$ and $\mathbf{b}$ be two orthogonal versors. We define the following scalar functions of the right Cauchy-Green strain tensor:

$$\begin{aligned}
\mathcal{I}_1(\mathsf{C}) &= \text{tr}\mathsf{C} \ , \\
\mathcal{I}_2(\mathsf{C}) &= \frac{1}{2}\left[(\text{tr}\mathsf{C})^2 - \text{tr}\mathsf{C}^2 \right] \ , \\
\mathcal{I}_3(\mathsf{C}) &= \det\mathsf{C} \ , \\
\mathcal{I}_{4,\mathbf{a}}(\mathsf{C}) &= \mathbf{a} \cdot \mathsf{C}\mathbf{a} \ , \\
\mathcal{I}_{5,\mathbf{a}}(\mathsf{C}) &= \mathbf{a} \cdot \mathsf{C}^2\mathbf{a} \ , \\
\mathcal{I}_{8,\mathbf{ab}}(\mathsf{C}) &= \mathbf{a} \cdot \mathsf{C}\mathbf{b} \ .
\end{aligned}$$

Given an orthonormal ternary $\{\mathbf{f}_0, \mathbf{s}_0, \mathbf{n}_0\}$, the set

$$\left\{ \mathcal{I}_1,\ \mathcal{I}_2,\ \mathcal{I}_3,\ \mathcal{I}_{4,\mathbf{f}_0},\ \mathcal{I}_{4,\mathbf{s}_0},\ \mathcal{I}_{5,\mathbf{f}_0},\ \mathcal{I}_{5,\mathbf{s}_0} \right\}$$

is a proper set of invariants for the symmetry group $\mathcal{G}_{\text{orth}}$ and it is equivalent to the set Υ_{orth}. Apart from the widely used invariants $\mathcal{I}_1$, $\mathcal{I}_2$ and $\mathcal{I}_3$, the presence of other invariants is the key to understand the mechanical response of the microstructure of the material at hand. These invariants have a clear physical interpretation: $\mathcal{I}_{4,\mathbf{a}}$ is the square of the local stretch along the direction $\mathbf{a}$, while $\mathcal{I}_{5,\mathbf{a}}$ is related to the variation of infinitesimal cross-area orthogonal to the direction $\mathbf{a}$.

On the other hand, the invariant $\mathcal{I}_{8,\mathbf{ab}}$ represents the angle spanned by the vectors $\mathsf{F}\mathbf{a}$ and $\mathsf{F}\mathbf{b}$ in the actual configuration, assuming that $\mathbf{a}\cdot\mathbf{b}=0$ in the reference configuration. However, $\mathcal{I}_{8,\mathbf{ab}}$ is redundant, because if $\mathbf{a}$ and $\mathbf{b}$ are othogonal, we have

$$\mathcal{I}_{8,\mathbf{ab}}^2 = \mathcal{I}_2 + \mathcal{I}_{4,\mathbf{a}}\,\mathcal{I}_{4,\mathbf{b}} + \mathcal{I}_{5,\mathbf{a}} + \mathcal{I}_{5,\mathbf{b}} - \mathcal{I}_1\,(\mathcal{I}_{4,\mathbf{a}} + \mathcal{I}_{4,\mathbf{b}})\ . \tag{2.2}$$

This statement can be proved recalling that, if $\{\mathbf{a},\mathbf{b},\mathbf{c}\}$ is an orthonormal ternary, then

$$\mathsf{C}\mathbf{a} = (\mathbf{a}\cdot\mathsf{C}\mathbf{a})\,\mathbf{a} + (\mathbf{b}\cdot\mathsf{C}\mathbf{a})\,\mathbf{b} + (\mathbf{c}\cdot\mathsf{C}\mathbf{a})\,\mathbf{c}\ .$$

Multiplying both sides by $\mathsf{C}\mathbf{a}$, we obtain

$$\mathcal{I}_{5,\mathbf{a}} = \mathbf{a}\cdot\mathsf{C}^2\mathbf{a} = (\mathbf{a}\cdot\mathsf{C}\mathbf{a})^2 + (\mathbf{b}\cdot\mathsf{C}\mathbf{a})^2 + (\mathbf{c}\cdot\mathsf{C}\mathbf{a})^2 = \mathcal{I}_{4,\mathbf{a}}^2 + \mathcal{I}_{8,\mathbf{ab}}^2 + \mathcal{I}_{8,\mathbf{ac}}^2\ . \tag{2.3}$$

In a similar way, it is easy to obtain the same result for $\mathsf{C}\mathbf{b}$ and $\mathsf{C}\mathbf{c}$

$$\mathcal{I}_{5,\mathbf{b}} = \mathcal{I}_{4,\mathbf{b}}^2 + \mathcal{I}_{8,\mathbf{ab}}^2 + \mathcal{I}_{8,\mathbf{bc}}^2\ , \tag{2.4}$$

$$\mathcal{I}_{5,\mathbf{c}} = \mathcal{I}_{4,\mathbf{c}}^2 + \mathcal{I}_{8,\mathbf{ac}}^2 + \mathcal{I}_{8,\mathbf{bc}}^2\ . \tag{2.5}$$

Finding the expression for $\mathcal{I}_{8,\mathbf{ac}}^2$ and $\mathcal{I}_{8,\mathbf{bc}}^2$ from (2.4) and (2.5), respectively, we can substitute these terms into (2.5) to find the relationship

$$\mathcal{I}_{5,\mathbf{c}} = \mathcal{I}_{5,\mathbf{a}} + \mathcal{I}_{5,\mathbf{b}} - \mathcal{I}_{4,\mathbf{a}}^2 - \mathcal{I}_{4,\mathbf{b}}^2 + \mathcal{I}_{4,\mathbf{c}}^2 - 2\,\mathcal{I}_{8,\mathbf{ab}}^2\ . \tag{2.6}$$

Recalling that

$$\begin{aligned}\mathcal{I}_1 = \mathrm{tr}\mathsf{C}\ &= \mathcal{I}_{4,\mathbf{a}} + \mathcal{I}_{4,\mathbf{b}} + \mathcal{I}_{4,\mathbf{c}}\ ,\\ \mathcal{I}_1^2 - 2\,\mathcal{I}_2 = \mathrm{tr}\mathsf{C}^2 &= \mathcal{I}_{5,\mathbf{a}} + \mathcal{I}_{5,\mathbf{b}} + \mathcal{I}_{5,\mathbf{c}}\ ,\end{aligned}$$

we obtain the expressions for $\mathcal{I}_{4,\mathbf{c}}^2$ and $\mathcal{I}_{5,\mathbf{c}}$:

$$\begin{aligned}\mathcal{I}_{4,\mathbf{c}}^2 &= (\mathcal{I}_1 - \mathcal{I}_{4,\mathbf{a}} - \mathcal{I}_{4,\mathbf{b}})^2 = \mathcal{I}_1^2 - 2\,\mathcal{I}_1\,(\mathcal{I}_{4,\mathbf{a}} + \mathcal{I}_{4,\mathbf{b}}) + 2\,\mathcal{I}_{4,\mathbf{a}}\,\mathcal{I}_{4,\mathbf{b}}\ ,\\ \mathcal{I}_{5,\mathbf{c}} &= \mathcal{I}_1^2 - 2\,\mathcal{I}_2 - \mathcal{I}_{5,\mathbf{a}} - \mathcal{I}_{5,\mathbf{b}}\ ,\end{aligned}$$

and substituting into (2.6) we have the final result:

$$\mathcal{I}_{8,\mathbf{ab}}^2 = \mathcal{I}_2 + \mathcal{I}_{4,\mathbf{a}}\,\mathcal{I}_{4,\mathbf{b}} + \mathcal{I}_{5,\mathbf{a}} + \mathcal{I}_{5,\mathbf{b}} - \mathcal{I}_1\,(\mathcal{I}_{4,\mathbf{a}} + \mathcal{I}_{4,\mathbf{b}})\ .$$

The Holzapfel-Ogden model considers an incompressible material, which means $\det\mathsf{F}=1$: as a consequence, the invariant $\mathcal{I}_3$ is not needed. Moreover, the model is based on a

reduced set of invariants:

$$\Upsilon_{\mathrm{HO}} = \left\{ \mathcal{I}_1,\ \mathcal{I}_{4,\mathbf{f}_0},\ \mathcal{I}_{4,\mathbf{s}_0},\ \mathcal{I}_{8,\mathbf{f}_0\mathbf{s}_0} \right\} .$$

The invariant $\mathcal{I}_{8,\mathbf{f}_0\mathbf{s}_0}$ is used in place of $\mathcal{I}_2$ and $\mathcal{I}_{5,\cdot}$, thus all the invariants used in this model have a straightforward kinematic interpretation, and quadratic invariants are neglected. Furthermore, we suppose that the strain energy density function can be splitted additively, so that:

$$\begin{aligned}\widehat{\mathcal{W}}(\mathsf{C}) &= \widetilde{\mathcal{W}}(\mathcal{I}_1,\ \mathcal{I}_{4,\mathbf{f}_0},\ \mathcal{I}_{4,\mathbf{s}_0},\ \mathcal{I}_{8,\mathbf{f}_0\mathbf{s}_0}) = \\ &= \widetilde{\mathcal{W}}_1(\mathcal{I}_1) + \widetilde{\mathcal{W}}_{4,\mathbf{f}_0}(\mathcal{I}_{4,\mathbf{f}_0}) + \widetilde{\mathcal{W}}_{4,\mathbf{s}_0}(\mathcal{I}_{4,\mathbf{s}_0}) + \widetilde{\mathcal{W}}_{8,\mathbf{f}_0\mathbf{s}_0}(\mathcal{I}_{8,\mathbf{f}_0\mathbf{s}_0}) .\end{aligned}$$

This approach has an obvious advantage: given that each invariant has a precise physical meaning, material parameters for each term of the strain energy can be easily found from an experiment, changing a term while keeping the others fixed.
In biological tissues, the greater is the strain, the greater is the apparent stiffness. In order to fit this type of response, each term in the strain energy is exponential:

$$\begin{aligned}\widetilde{\mathcal{W}}_1(\mathcal{I}_1) &= \frac{a}{2b}\left[e^{b(\mathcal{I}_1-3)} - 1\right] , \\ \widetilde{\mathcal{W}}_{4,\mathbf{f}_0}(\mathcal{I}_{4,\mathbf{f}_0}) &= \frac{a_f}{2b_f}\left[e^{b_f(\mathcal{I}_{4,\mathbf{f}_0}-1)^2} - 1\right] , \\ \widetilde{\mathcal{W}}_{4,\mathbf{s}_0}(\mathcal{I}_{4,\mathbf{s}_0}) &= \frac{a_s}{2b_s}\left[e^{b_s(\mathcal{I}_{4,\mathbf{s}_0}-1)^2} - 1\right] , \\ \widetilde{\mathcal{W}}_{8,\mathbf{f}_0\mathbf{s}_0}(\mathcal{I}_{8,\mathbf{f}_0\mathbf{s}_0}) &= \frac{a_{fs}}{2b_{fs}}\left[e^{b_{fs}\mathcal{I}^2_{8,\mathbf{f}_0\mathbf{s}_0}} - 1\right] .\end{aligned}$$

Therefore, we can compute the explicit form of the Cauchy stress tensor T. However, we should pay attention to the incompressibility constraint: the variations of deformations must be tangent to the manifold $\{\mathsf{F} \in \mathrm{Lin}^+(\mathbb{R}^3) : \det\mathsf{F} = 1\}$. As a consequence, there exists a scalar function $p : \Omega_0 \to \mathbb{R}$, which denotes the pressure, such that:

$$\mathsf{P} - \frac{\partial \mathcal{W}}{\partial \mathsf{F}} = -p\ \frac{\partial \det}{\partial \mathsf{F}} = -p\ \mathrm{cof}\mathsf{F}$$

where we recall that the cofactor of a tensor F is the unique tensor cofF such that

$$\mathsf{F}\mathbf{u} \wedge \mathsf{F}\mathbf{v} \cdot \mathbf{w} = \mathrm{cof}\mathsf{F}\ \mathbf{u} \wedge \mathbf{v} \cdot \mathbf{w} \quad \text{for every } \mathbf{u}, \mathbf{v}, \mathbf{w} \in \mathbb{R}^3 .$$

It is not difficult to properly compute the derivative of $\mathcal{W}$:

$$\begin{aligned}\mathsf{P} &= \frac{\partial \mathcal{W}}{\partial \mathsf{F}} - p\ \mathrm{cof} = 2\mathsf{F}\frac{\partial \widehat{\mathcal{W}}}{\partial \mathsf{C}} - p\ \mathrm{cof} = \\ &= 2\mathsf{F}\left[\frac{\partial \widetilde{\mathcal{W}}_1}{\partial \mathcal{I}_1}\frac{\partial \mathcal{I}_1}{\partial \mathsf{C}} + \frac{\partial \widetilde{\mathcal{W}}_{4,\mathbf{f}_0}}{\partial \mathcal{I}_{4,\mathbf{f}_0}}\frac{\partial \mathcal{I}_{4,\mathbf{f}_0}}{\partial \mathsf{C}} + \frac{\partial \widetilde{\mathcal{W}}_{4,\mathbf{s}_0}}{\partial \mathcal{I}_{4,\mathbf{s}_0}}\frac{\partial \mathcal{I}_{4,\mathbf{s}_0}}{\partial \mathsf{C}} + \frac{\partial \widetilde{\mathcal{W}}_{8,\mathbf{f}_0\mathbf{s}_0}}{\partial \mathcal{I}_{8,\mathbf{f}_0\mathbf{s}_0}}\frac{\partial \mathcal{I}_{8,\mathbf{f}_0\mathbf{s}_0}}{\partial \mathsf{C}}\right] - p\ \mathrm{cof} ,\end{aligned}$$

where the derivatives of invariants are:

$$\frac{\partial \mathcal{I}_1}{\partial \mathsf{C}} = \mathsf{I} \ , \quad \frac{\partial \mathcal{I}_{4,\mathbf{f}_0}}{\partial \mathsf{C}} = \mathbf{f}_0 \otimes \mathbf{f}_0 \ , \quad \frac{\partial \mathcal{I}_{4,\mathbf{s}_0}}{\partial \mathsf{C}} = \mathbf{s}_0 \otimes \mathbf{s}_0 \ , \quad \frac{\partial \mathcal{I}_{8,\mathbf{f}_0\mathbf{s}_0}}{\partial \mathsf{C}} = \frac{1}{2}(\mathbf{f}_0 \otimes \mathbf{s}_0 + \mathbf{s}_0 \otimes \mathbf{f}_0) \ .$$

In conclusion, defining $\mathbf{f} := \mathsf{F}\mathbf{f}_0$ and $\mathbf{s} := \mathsf{F}\mathbf{s}_0$, the correct form for the Cauchy stress tensor reads:

$$\begin{aligned} \mathsf{T} = {} & a \ e^{b(\mathcal{I}_1 - 3)} \ \mathsf{B} - p\mathsf{I} + \\ & + 2 \ a_f(\mathcal{I}_{4,\mathbf{f}_0} - 1) \ e^{b_f(\mathcal{I}_{4,\mathbf{f}_0} - 1)^2} \ \mathbf{f} \otimes \mathbf{f} + 2 \ a_s(\mathcal{I}_{4,\mathbf{s}_0} - 1) \ e^{b_s(\mathcal{I}_{4,\mathbf{s}_0} - 1)^2} \ \mathbf{s} \otimes \mathbf{s} + \\ & + a_{fs} \ \mathcal{I}_{8,\mathbf{f}_0\mathbf{s}_0} \ e^{b_{fs}\mathcal{I}^2_{8,\mathbf{f}_0\mathbf{s}_0}} \ (\mathbf{f} \otimes \mathbf{s} + \mathbf{s} \otimes \mathbf{f}) \ . \end{aligned}$$

The transversely isotropic version of the model can be obtained by setting $a_s = b_s = a_{fs} = b_{fs} = 0$, while the isotropic model is given by the first two terms.

The Holzapfel-Ogden model reflects the orthotropic underlying microstructure of the myocardium: the vectors $\mathbf{f}_0$ and $\mathbf{s}_0$ denote the fibre and sheet directions at the microscale in the reference configuration. In particular, $\mathbf{f}_0$ represents the local muscle fibre direction, lying within the sheet, while $\mathbf{s}_0$ is locally tangent to the sheet and orthogonal to $\mathbf{f}_0$. By definition, $\mathbf{n}_0 = \mathbf{f}_0 \times \mathbf{s}_0$ is the normal to the local sheet.

It is clear that the tensorial form of the Cauchy stress is strictly related to the mechanical properties of the material, in particular to its microstructure: while the isotropic contribution accounts for the extracellular matrix, the anisotropic terms reproduce the behaviour of fibres and sheets, taking into account the variation of the angle between the two through the invariant $\mathcal{I}_{8,\mathbf{f}_0\mathbf{s}_0}$. In addition, the transversely isotropic version of the model neglects the influence of the sheet structure, as all of the terms related to $\mathbf{s}_0$ are turned off.

Nevertheless, we remark that this model does not behave in the correct way in the compressive regime, due to the different response of fibres with respect to the tensile regime. As a matter of fact, Holzapfel and Ogden suggest to turn off the anisotropic terms associated to $\mathcal{I}_{4,\mathbf{f}_0}$ and $\mathcal{I}_{4,\mathbf{s}_0}$ under compression, which means when $\mathcal{I}_{4,\mathbf{f}_0} < 1$ or $\mathcal{I}_{4,\mathbf{s}_0} < 1$,respectively. Thus, it is sufficient to slightly change the expression for $\widetilde{\mathcal{W}}_{4,\mathbf{f}_0}$ and $\widetilde{\mathcal{W}}_{4,\mathbf{s}_0}$:

$$\begin{aligned} \widetilde{\mathcal{W}}_{4,\mathbf{f}_0}(\mathcal{I}_{4,\mathbf{f}_0}) &= \frac{a_f}{2b_f}\left[e^{b_f(\mathcal{I}_{4,\mathbf{f}_0} - 1)^2_+} - 1\right] \ , \\ \widetilde{\mathcal{W}}_{4,\mathbf{s}_0}(\mathcal{I}_{4,\mathbf{s}_0}) &= \frac{a_s}{2b_s}\left[e^{b_s(\mathcal{I}_{4,\mathbf{s}_0} - 1)^2_+} - 1\right] \ , \end{aligned}$$

where $(\phi)_+$ is equal to ϕ if $\phi > 0$, and zero otherwise. In this case, strong ellipticity of $\widetilde{\mathcal{W}}_{4,\cdot}$ can be proved, thus this modification of the model is favorable both under the mechanical and the mathematical point of view.

2.3 Variational framework

In the continuum mechanics framework, the equation of the balance of the linear momentum in material coordinates reads:

$$-\text{DIV } \mathsf{P} = \rho_0 \mathbf{b}_0$$

where $\mathbf{b}_0$ is an external body force per unit volume and ρ_0 is the density of the body, in the reference configuration; natural boundary conditions are applied on the portion of the boundary $\partial_N \Omega_0$. This equation can be formulated as a minimum problem, and the corresponding functional is

$$\mathcal{F}(\boldsymbol{\varphi}) := \int_{\Omega_0} \mathcal{W}(\mathbf{X}, \mathsf{F}) \, \mathrm{d}V - \int_{\Omega_0} \rho_0 \mathbf{b}_0 \cdot \boldsymbol{\varphi} \, \mathrm{d}V - \int_{\partial_N \Omega_0} \mathbf{t}_0 \cdot \boldsymbol{\varphi} \, \mathrm{d}A \, . \tag{2.7}$$

$\mathbf{t}_0 : \partial_N \Omega_0 \to \mathbb{R}^3$ represents a traction at the boundary, with $\mathbf{t}_0 = \mathsf{P}\mathbf{n}_0$, where $\mathbf{n}_0$ is the outward normal to the boundary $\partial_N \Omega_0$.
The objective is to find the deformation $\boldsymbol{\varphi}$ that minimizes the functional $\mathcal{F}$. Naturally, the minimum has to be admissible, and it has to meet the essential boundary conditions, thus we consider the set

$$\mathcal{C} = \left\{ \boldsymbol{\varphi} : \Omega_0 \to \Omega : \mathsf{F} \in \text{Lin}^+(\mathbb{R}^3) \text{ and } \boldsymbol{\varphi}|_{\partial_D \Omega_0} = \mathbf{g} \right\} .$$

Moreover, we need to make sure that at least a minimum exists. This can be accomplished by restricting the functional space, and a proper choice is to look for $\boldsymbol{\varphi}$ in the Sobolev space $V := \mathcal{C} \cap W^{1,s}(\Omega_0; \mathbb{R}^3)$. The existence of a minimum of the functional is guaranteed by continuity conditions and compactness properties of the space; in addition, if the functional and the space are convex, then the minimum is unique. Nevertheless, in the case of hyperelastic materials, the strain energy density function is convex with respect to F, but the set $\text{Lin}^+(\mathbb{R}^3)$ is not convex.
In order to guarantee the existence of the minimum, in our case, we have to rely on the concept of *polyconvexity*: a function $\mathcal{W} : \text{Lin}^+(\mathbb{R}^3) \to \mathbb{R}$ is polyconvex if there exists a convex function $g : \text{Lin}^+(\mathbb{R}^3) \times \text{Lin}^+(\mathbb{R}^3) \times \mathbb{R}^+ \to \mathbb{R}$ such that

$$\mathcal{W}(\mathsf{F}) = g(\mathsf{F}, \text{cof}\mathsf{F}, \det\mathsf{F}) \quad \text{for every } \mathsf{F} \in \text{Lin}^+(\mathbb{R}^3) \, .$$

For instance, a function $\mathcal{W}(\mathsf{F}) = \mathcal{W}(\det\mathsf{F})$ is convex with respect to $\det\mathsf{F}$, but it cannot be convex with respect to F because the set $\text{Lin}^+(\mathbb{R}^3)$ is not convex; however, $\mathcal{W}$ is polyconvex, because the function $\mathcal{W}(\det\mathsf{F}) = \mathcal{W}(J)$ is convex on $\mathbb{R}^+$. It is possible to prove that if the function $\mathcal{W}$ is polyconvex, then there exists at least one minimum in the space $W^{1,s}(\Omega_0; \mathbb{R}^3)$, with $s > \frac{2}{3}$ and $\frac{1}{s} + \frac{1}{q} < \frac{4}{3}$ and $\text{cof}\mathsf{F} \in L^q(\Omega_0; \text{Lin}^+(\mathbb{R}^3))$.

If we assume that there exists a deformation $\boldsymbol{\varphi} \in \mathcal{C}$ that minimizes the functional $\mathcal{F}$, then it must be a stationary point of $\mathcal{F}$, if the proper regularity hypothesis are met; a variation $\boldsymbol{\eta}$ about $\boldsymbol{\varphi}$ must be admissible, so it belongs to the tangent space of $\mathcal{C}$ at $\boldsymbol{\varphi}$:

$$\mathcal{T}_{\boldsymbol{\varphi}}\mathcal{C} := \left\{ \boldsymbol{\eta} : \Omega \to \mathbb{R}^3 \text{ such that } \boldsymbol{\eta} \circ \boldsymbol{\varphi}|_{\partial_D \Omega_0} = \mathbf{0} \right\} ,$$

which means that we consider a small variation about the deformation $\boldsymbol{\varphi}$, while keeping the essential boundary condition fixed. Defining the material variation $\boldsymbol{\eta}_0 := \boldsymbol{\eta} \circ \boldsymbol{\varphi}$ in the reference configuration, we recall that the *Gâteaux derivative* of a functional $\mathcal{F} : V \to \mathbb{R}$ is defined as

$$\langle D\mathcal{F}(\boldsymbol{\varphi}), \boldsymbol{\eta}_0 \rangle := \frac{\mathrm{d}}{\mathrm{d}\epsilon} \mathcal{F}(\boldsymbol{\varphi} + \epsilon \boldsymbol{\eta}_0) \Big|_{\epsilon=0} = \lim_{\epsilon \to 0} \frac{\mathcal{F}(\boldsymbol{\varphi} + \epsilon \boldsymbol{\eta}_0) - \mathcal{F}(\boldsymbol{\varphi})}{\epsilon} .$$

The minimum of a functional $\mathcal{F}$ is such that its Gâteaux derivative is null; thus, we have

$$\begin{aligned} \frac{\mathrm{d}}{\mathrm{d}\epsilon} \mathsf{F}(\boldsymbol{\varphi} + \epsilon \boldsymbol{\eta} \circ \boldsymbol{\varphi}) \Big|_{\epsilon=0} &= \text{ GRAD } \boldsymbol{\eta}_0 := (\nabla \boldsymbol{\eta} \circ \boldsymbol{\varphi}) \ \mathsf{F}(\boldsymbol{\varphi}) , \\ \frac{\mathrm{d}}{\mathrm{d}\epsilon} \int_{\Omega_0} \mathcal{W}\Big(\mathsf{F}(\boldsymbol{\varphi} + \epsilon \boldsymbol{\eta} \circ \boldsymbol{\varphi})\Big) \ \mathrm{d}V \Big|_{\epsilon=0} &= \int_{\Omega_0} \frac{\partial \mathcal{W}}{\partial \mathsf{F}}\Big(\mathsf{F}(\boldsymbol{\varphi})\Big) : (\nabla \boldsymbol{\eta} \circ \boldsymbol{\varphi}) \ \mathsf{F}(\boldsymbol{\varphi}) \ \mathrm{d}V \\ &= \int_{\Omega_0} \mathsf{P} : \text{GRAD } \boldsymbol{\eta}_0 \ \mathrm{d}V . \end{aligned}$$

The other two terms in equation (2.7) are linear with respect to $\boldsymbol{\varphi}$, thus the Gâteaux derivative is trivially obtained; the final form of the problem in the reference configuration reads:

Find $\boldsymbol{\varphi} \in V$ such that

$$\int_{\Omega_0} \mathsf{P} : \text{GRAD } \boldsymbol{\eta}_0 \ \mathrm{d}V - \int_{\Omega_0} \rho_0 \mathbf{b}_0 \cdot \boldsymbol{\eta}_0 \ \mathrm{d}V - \int_{\partial_N \Omega_0} \mathbf{t}_0 \cdot \boldsymbol{\eta}_0 \ \mathrm{d}A = 0 \quad \text{for each } \boldsymbol{\eta}_0 \in V .$$

Recalling that $\mathbf{x} = \boldsymbol{\varphi}(\mathbf{X})$, exploiting the Piola transformation, we can set the same problem in the actual configuration:

$$\begin{aligned} \int_{\Omega_0} \mathsf{P} : \text{GRAD } \boldsymbol{\eta}_0 \ \mathrm{d}V = \int_{\Omega} \mathsf{P} : \nabla \boldsymbol{\eta} \mathsf{F} \ J^{-1} \ \mathrm{d}v = \int_{\Omega} J^{-1} \mathsf{P}\mathsf{F}^{\mathsf{T}} : \nabla \boldsymbol{\eta} \ \mathrm{d}v = \int_{\Omega} \mathsf{T} : \nabla \boldsymbol{\eta} \ \mathrm{d}v , \\ \int_{\Omega_0} \rho_0 \mathbf{b}_0 \cdot \boldsymbol{\eta}_0 \ \mathrm{d}V = \int_{\Omega} (J^{-1} \rho_0 \mathbf{b}_0) \circ \boldsymbol{\varphi}^{-1} \cdot \boldsymbol{\eta} \ \mathrm{d}v = \int_{\Omega} \rho \mathbf{b} \cdot \boldsymbol{\eta} \ \mathrm{d}v , \\ \int_{\partial_N \Omega_0} \mathbf{t}_0 \cdot \boldsymbol{\eta}_0 \ \mathrm{d}A = \int_{\partial_N \Omega_0} \mathsf{P}\mathbf{n}_0 \cdot \boldsymbol{\eta}_0 \ \mathrm{d}A = \int_{\partial_N \Omega} \mathsf{T}\mathbf{n} \cdot \boldsymbol{\eta} \ \mathrm{d}a = \int_{\partial_N \Omega} \mathbf{t} \cdot \boldsymbol{\eta} \ \mathrm{d}a , \end{aligned}$$

where $\rho = (J^{-1}\rho_0) \circ \boldsymbol{\varphi}^{-1}$, $\mathbf{b} = \mathbf{b}_0 \circ \boldsymbol{\varphi}$. In conclusion, we can write the variational problem set in the actual configuration:

$$\begin{aligned}&\text{Find } \boldsymbol{\varphi} \in V \text{ such that}\\ &\int_\Omega \mathsf{T} : \nabla\boldsymbol{\eta}\, \mathrm{d}v - \int_\Omega \rho\mathbf{b}\cdot\boldsymbol{\eta}\, \mathrm{d}v - \int_{\partial_N\Omega} \mathbf{t}\cdot\boldsymbol{\eta}\, \mathrm{d}a = 0 \quad \text{for each } \boldsymbol{\eta} \in V\ .\end{aligned}$$

2.4 Active Mechanics

The active contraction of cardiac fibres is a key feature of the cardiac mechanics, but the Holzapfel-Ogden model presented in previous sections only encodes the passive properties of the material. In the myocardium, the electric signal is produced by self-excitable cells and triggers the release of intracellular calcium ions. The voltage wave travels along the conduction fibres and dictates the shortening of the cardiomyocytes at the microstructural level, resulting in a macroscopic contraction of the cardiac muscle that allows the pumping of the blood through the arteries. In the literature, there are two different strategies for the mathematical modelling of the active mechanics of the cardiac tissue, including the active tension produced by the contraction of the cardiomyocytes. The *active stress* approach adds an active contribution to the stress of the material, dependent on fibre orientation. On the other hand, an *active strain* approach can be adopted, based on a multiplicative decomposition of the tensor gradient of deformation, providing a constitutive law for the active strain contribution.

2.4.1 Active Stress

During an isometric test, an electrically stimulated cardiomyocyte, kept at a fixed length, produces a reaction constraint that can be associated to an active force. The same constraint can be obtained, in the form of an elastic response, by stretching the cell over its resting length, when no electric stimulus is applied: this is a natural passive response. Thus, it is possible to assume that the total force exerted by the cardiomyocyte can be additively splitted into two contributions: a passive one, representing the mechanical response to external loads, and an active one to take into account the force generated by the cell under the effect of an electric signal (Pezzuto 2013). Thus, we can write the total force exerted by the cell as:

$$f_{total} = f_{active} + f_{passive}\ .$$

As usual, we assume that the mechanical properties of the cardiomyocyte can be described in the hyperelasticity framework. Consequently, if $\mathcal{W}$ is the strain energy density

function, the *passive* Cauchy stress is:

$$\mathsf{T} = (\det\mathsf{F})^{-1}\frac{\partial \mathcal{W}}{\partial \mathsf{F}}\ \mathsf{F}^{\mathsf{T}}\ .$$

If the electric signal has reached the cell, activation is triggered, and an extra term must be added to the elastic stress:

$$\mathsf{T}(\mathsf{F},\xi) = \mathsf{T}_e(\mathsf{F}) + \mathsf{T}_a(\mathsf{F},\xi) = (\det\mathsf{F})^{-1}\frac{\partial \mathcal{W}}{\partial \mathsf{F}}\ \mathsf{F}^{\mathsf{T}} + \mathsf{T}_a(\mathsf{F},\xi)\ .$$

As we can see, the active stress $\mathsf{T}_a(\mathsf{F},\xi)$ depends on an extra variable ξ which takes into account the electrophysiological status of the myocyte, and, in general, also depends on F. If no activation is involved, say for $\xi = \xi_{ref}$ the active contribution vanishes:

$$\mathsf{T}_a(\mathsf{F},\xi_{ref}) = \mathsf{O} \quad \text{for every } \mathsf{F} \in \mathrm{Lin}^+(\mathbb{R}^3)\ .$$

In order to find a proper expression for T, we need to enforce objectivity and the correct symmetries of the microstructure. Considering the second Piola-Kirchhoff tensor associated to T_a

$$\mathsf{S}_a(\mathsf{F},\xi) = (\det\mathsf{F})\ \mathsf{F}^{-1}\ \mathsf{T}_a(\mathsf{F},\xi_{ref})\ \mathsf{F}^{-\mathsf{T}}\ ,$$

the requirement of objectivity means that, thanks to the polar decomposition theorem, S_a depends on F only through U, where $\mathsf{F} = \mathsf{RU}$. Thus, we can consider:

$$\widehat{\mathsf{S}}_a(\mathsf{C},\xi) = \widehat{\mathsf{S}}_a(\mathsf{F}^{\mathsf{T}}\mathsf{F},\xi) = \mathsf{S}_a(\mathsf{F},\xi)\ .$$

In addition, the tensor $\widehat{\mathsf{S}}_a$ should be transversely isotropic, because the active stress acts in the fibre direction $\mathbf{f}_0$, while no activation occurs in the sheet direction $\mathbf{s}_0$. As a consequence, we have

$$\widehat{\mathsf{S}}_a(\mathsf{C},\xi) = s_1\ \mathsf{I} + s_2\ \mathsf{C} + s_4\ \mathbf{f}_0\otimes\mathbf{f}_0 + s_5\ \mathrm{sym}(\mathsf{C}\mathbf{f}_0\otimes\mathbf{f}_0)\ ,$$

where s_1, s_2, s_4 and s_5 are scalar function depending on ξ and on the invariants

$$\Upsilon = \left\{\mathrm{tr}\mathsf{C},\ \mathrm{tr}\mathsf{C}^2,\ \mathbf{f}_0\cdot\mathsf{C}\mathbf{f}_0,\ \mathbf{f}_0\cdot\mathsf{C}^2\mathbf{f}_0\right\}\ .$$

Usually, both the trace and the quadratic invariants are neglected, thus we have

$$\widehat{\mathsf{S}}_a(\mathsf{C},\xi) = s_a(\mathcal{I}_{4,\mathbf{f}_0},\xi)\ \mathbf{f}_0\otimes\mathbf{f}_0\ \ ,$$

which means, in terms of physical stress

$$\mathsf{T}_a(\mathsf{C},\xi) = s_a(\mathcal{I}_{4,\mathbf{f}_0},\xi)\ \mathsf{F}\mathbf{f}_0\otimes\mathsf{F}\mathbf{f}_0\ \ . \tag{2.8}$$

This expression has a very straightforward interpretation: the active stress acts in the fibre direction, with a magnitude that nonlinearly depends on the current stretch of the fibre. The scalar factor s_a, which is dimensionally a force per unit area, has to be related to the active force f_{active}, can be obtained by considering a test case, such as the contraction of a rod along its axis:

$$\mathsf{F} = \lambda\ \mathbf{f}_0 \otimes \mathbf{f}_0 + \frac{1}{\sqrt{\lambda}}(\mathsf{I} - \mathbf{f}_0 \otimes \mathbf{f}_0)\ .$$

Thus, from (2.8) we have

$$\mathsf{T}_a(\lambda, \xi) = s_a(\lambda^2, \xi)\ \lambda^2 = f_{active} A_0 \lambda\ , \quad \text{and, simplifying,} \quad f_{active}(\lambda, \xi) = \frac{\lambda}{A_0} s_a(\lambda^2, \xi)\ ,$$

where A_0 is the initial cross area. Observing that $\lambda^2 = \mathcal{I}_{4,\mathbf{f}_0}$, the force is independent from λ if

$$s_a(\mathcal{I}_{4,\mathbf{f}_0}, \xi) = A_0 \frac{f_{active}(\xi)}{\sqrt{\mathcal{I}_{4,\mathbf{f}_0}}}$$

For example, if the cross section does not remain orthogonal to $\mathbf{f}_0$ in the deformation, a choice could be

$$\overline{s}_a(\mathcal{I}_{4,\mathbf{f}_0}, \xi) = A_0 \frac{f_{active}(\xi)}{|\mathsf{C}^{-1}\mathbf{f}_0 \cdot \mathbf{f}_0|}\ .$$

2.4.2 Active Strain

The active strain approach is based on a multiplicative decomposition of the deformation gradient tensor in an elastic deformation $\mathsf{F_e}$ and an active distortion $\mathsf{F_a}$:

$$\mathsf{F} = \mathsf{F_e}\mathsf{F_a}\ .$$

The biochemical status of the fibres induces an inelastic deformation, changing the length and the shape of the fibres; then, an elastic deformation accommodates the active strain distortion in order to preserve the compatibility. There is a deep physiological meaning for this approach: the sarcomeres shorten because of the sliding filaments of the actin-myosin molecular motor, and this shortening is encoded by $\mathsf{F_a}$; then, starting from this deformed configuration, the elastic deformation occurs (Pezzuto 2013).
We remark that the strain energy density is a function of $\mathsf{F_e}$ only, while $\mathsf{F_a}$ is fully dissipative. The objective is to find the deformation that minimizes the total elastic energy with respect to all the admissible configurations:

$$\min_{\boldsymbol{\varphi} \in \mathcal{C}} \int_{\Omega_0} \mathcal{W}(\mathsf{F}\mathsf{F_a}^{-1})\ \mathrm{det}\mathsf{F_a}\ \mathrm{d}V - \langle \mathbf{f}^{ext}, \boldsymbol{\varphi} \rangle\ . \tag{2.9}$$

In the case $\mathbf{f}^{ext} = \mathbf{0}$, it would be reasonable to argue that $\mathsf{F} = \mathsf{F_a}$, since $\mathsf{F_e} = \mathsf{I}$ is a local minimum of $\mathcal{W}$. Nevertheless, the existence of a deformation $\boldsymbol{\varphi}$ such that GRAD $\boldsymbol{\varphi} = \mathsf{F_a}$ is not guaranteed.

We suppose that a minimum exists for (2.9): thus, the first variation of the functional must be null, which means

$$\int_{\Omega_0} \det\mathsf{F_a}\, \frac{\partial \mathcal{W}(\mathsf{F_e})}{\partial \mathsf{F_e}}\, \mathsf{F_a^{-T}} : \mathrm{GRAD}\boldsymbol{\eta}_0 \, \mathrm{d}V - \langle \mathbf{f}^{ext}, \boldsymbol{\eta}_0 \rangle \; = 0 \; .$$

In this case, the first Piola-Kirchhoff and the Cauchy stress tensors are

$$\mathsf{P} = \det\mathsf{F_a}\, \frac{\partial \mathcal{W}(\mathsf{F_e})}{\partial \mathsf{F_e}}\, \mathsf{F_a^{-T}} \quad \text{and} \quad \mathsf{T} = (\det\mathsf{F_e})^{-1}\, \frac{\partial \mathcal{W}(\mathsf{F_e})}{\partial \mathsf{F_e}}\, \mathsf{F_e^T} \; .$$

If the activation is not triggered, we have $\mathsf{F_a} = \mathsf{I}$ and $\mathsf{F_e} = \mathsf{F}$, thus the passive behaviour of the material is recovered. If no deformation occurs, $\mathsf{F} = \mathsf{I}$ and $\mathsf{F_e} = \mathsf{F_a^{-1}}$, we can see the Cauchy stress tensor as a purely active response:

$$\mathsf{T} = \det\mathsf{F_a}\, \frac{\partial \mathcal{W}(\mathsf{F_e})}{\partial \mathsf{F_e}} \bigg|_{\mathsf{F_e}=\mathsf{F_a^{-1}}} \mathsf{F_a^T} \; .$$

The tensorial form of the active Cauchy stress can be computed through the usual strain energy approach. It is necessary to define the expression for the active distortion $\mathsf{F_a}$, and a transversely isotropic and isochoric constitutive law is

$$\mathsf{F_a} = (1-\gamma)\, \mathbf{f}_0 \otimes \mathbf{f}_0 + \frac{1}{\sqrt{1-\gamma}} \left(\mathsf{I} - \mathbf{f}_0 \otimes \mathbf{f}_0 \right) \; . \tag{2.10}$$

Naturally, activation occurs only in the direction of fibres, and the choice of an isochoric model is supported by the physiological fact that myocytes do not change their volume in a significant way during contraction. The parameter γ triggers activation, since we have $\mathsf{F_a} = \mathsf{I}$ if $\gamma = 0$, and depends on the electrophysiological status of the cell, encoded by the previously introduced variable ξ; furthermore, we assume it does not depend on the strain. This hypothesis is based on a physiological argument: it has been shown that cells activated at different levels of prestretch produce a different force to reach almost the same activated elongation of the sarcomeres (Peterson et al. 2013).

In order to obtain the correct formulation for the active strain model, we have to substitute F with $\mathsf{F_e}$ in the strain energy density function, thus the energy $\mathcal{W}$ will be a function of $\mathsf{F_e} = \mathsf{F}\mathsf{F_a^{-1}}$. For instance, the left and right Chauchy-Green tensors will be, respectively:

$$\mathsf{B_e} = \mathsf{F_e}\mathsf{F_e^T} = \mathsf{F}\mathsf{F_a^{-1}}\mathsf{F_a^{-T}}\mathsf{F^T} \quad \text{and} \quad \mathsf{C_e} = \mathsf{F_e^T}\mathsf{F_e} = \mathsf{F_a^{-T}}\mathsf{F^T}\mathsf{F}\mathsf{F_a^{-1}} \; .$$

Considering an active strain tensor $\mathsf{F_a}$ in the form (1.9), we can compute the explicit expression for the strain tensors:

$$\mathsf{B_e} = \gamma \mathsf{B} + \frac{1-\gamma^3}{\gamma^2}\, \mathsf{F}\mathbf{f}_0 \otimes \mathsf{F}\mathbf{f}_0 \ ,$$
$$\mathsf{C_e} = \gamma \mathsf{C} + (\gamma^{-2} - 2\gamma^{-\frac{1}{2}} + \gamma)\, \mathcal{I}_{4,\mathbf{f}_0} \mathbf{f}_0 \otimes \mathbf{f}_0 + 2\,(\gamma^{-\frac{1}{2}} - \gamma)\, \mathsf{F}\mathbf{f}_0 \otimes \mathsf{F}\mathbf{f}_0 \ .$$

2.5 Numerical approximation of the pressure-volume loop

Thanks to the mechanical framework and the variational formulation introduced in previous sections, it is now possible to introduce a proper functional and numerical model for the simulation of a complete PV loop, focusing on the left ventricle of the heart.
First of all, we need to add the active contribution to the variational formulation introduced in Section 2.3: in order to achieve this, it is sufficient to see the strain energy density $\mathcal{W}$ as a function of $\mathsf{F_e} = \mathsf{F}\mathsf{F_a}^{-1}$, where the exact form for $\mathsf{F_a}$ is known and depends on the activation parameter γ.
In addition, we have to consider other physiological aspects of the cardiac cycle. The systolic phase starts when the electric signal, produced by self-excitable cells, reaches the myocytes and triggers the twitch of the sarcomeres. This happens near the end-diastolic point (EDP) of the pressure-volume loop, just after that the blood has been pushed inside the ventricle through the mitral valve. The contraction of the fibres suddenly increases the pressure in the cavity, closing the mitral valve: this is an *isochoric contraction*, because the incompressibility of the blood preserves the chamber volume. In this phase, the inner pressure raises from the end-diastolic value (*preload*) to the arterial one (*afterload*), inducing the opening of the aortic valve, which allows the blood to be pumped in the whole body.
Let $\mathcal{V}_{inner}(\boldsymbol{\varphi})$ be the volume of the chamber computed from the deformation; during the isochoric contraction phase, the inner volume is constant, thus in the variational formulation we would like to impose the following:

$$\mathcal{V}_{inner}(\boldsymbol{\varphi}) = V_{EDP} \ . \tag{2.11}$$

The explicit form of $\mathcal{V}_{inner}$ can be computed as follows:

$$\mathcal{V}_{inner}(\boldsymbol{\varphi}) = \int_{\boldsymbol{\varphi}(\Omega_{inner})} \mathrm{d}v = \frac{1}{3}\int_{\partial\boldsymbol{\varphi}(\Omega_{inner})} \mathbf{x}\cdot\mathbf{n}\ \mathrm{d}a = -\frac{1}{3}\int_{\partial\boldsymbol{\varphi}(\Gamma_{endo})} \mathbf{x}\cdot\mathbf{n}\ \mathrm{d}a \ ,$$

where Ω_{inner} is the volume of the chamber, Γ_{endo} is the surface of the endocardium and $\mathbf{n}$ is the outward unit vector. As a consequence, taking into account the incompressibility

of the material, the Lagrangian formulation reads:

$$\mathcal{L}(\boldsymbol{\varphi}, p, \xi; \gamma) := \int_{\Omega_0} \mathcal{W}\big(\mathsf{F}(\boldsymbol{\varphi})\mathsf{F}_{\mathsf{a}}^{-1}(\gamma)\big)\ \mathrm{d}V - \int_{\Omega_0} p\ (J-1)\ \mathrm{d}V - p_{inner}(\mathcal{V}_{inner}(\boldsymbol{\varphi}) - V_{EDP})\ ,$$

where the Lagrangian multiplier p_{inner} has been introduced to impose (2.11), and the activation parameter γ is usually a hat function with the maximum at the end-systolic point. Taking the first variation at $(\boldsymbol{\varphi}, p, p_{inner})$, it is easy to obtain the saddle-point problem for the functional $\mathcal{L}$:

$$\begin{cases} \langle D_{\boldsymbol{\varphi}}\mathcal{L}, \boldsymbol{\eta}\rangle & = \displaystyle\int_{\Omega_0} \big(\mathsf{P}(\mathsf{F}\mathsf{F}_{\mathsf{a}}^{-1})\mathsf{F}_{\mathsf{a}}^{-\mathsf{T}} - p\ \mathrm{cof}\mathsf{F}\big) : \mathrm{GRAD}\boldsymbol{\eta}\ \mathrm{d}V\ + \\ & \quad - p_{inner}\displaystyle\int_{\Omega_0} D_{\boldsymbol{\varphi}}\mathcal{V}_{inner}\cdot\boldsymbol{\eta}\ \mathrm{d}V = 0\ , \\ \langle D_p\mathcal{L}, q\rangle & = -\displaystyle\int_{\Omega_0} q\ (J-1)\ \mathrm{d}V\ = 0\ , \\ \langle D_{p_{inner}}\mathcal{L}, q_{inner}\rangle & = -\ q_{inner}(\mathcal{V}_{inner}(\boldsymbol{\varphi}) - V_{EDP}) = 0\ , \end{cases} \tag{2.12}$$

for all $(\boldsymbol{\eta}, q, q_{inner}) \in V \times Q \times \mathbb{R}$, with $V \subseteq \mathcal{T}_{\boldsymbol{\varphi}}\mathcal{C}$ and $Q = L^2(\Omega_0)$. We point out that ξ is the (unknown) inner pressure to be applied in order to keep the inner volume constant. The explicit form for the second term in the first equation in (2.12) is:

$$\int_{\Omega_0} D_{\boldsymbol{\varphi}}\mathcal{V}_{inner}\cdot\boldsymbol{\eta}\ \mathrm{d}V = \int_{\Omega_0} \mathrm{cof}\mathsf{F} : \mathrm{GRAD}\boldsymbol{\eta}\ \mathrm{d}V = -\int_{\partial\boldsymbol{\varphi}(\Gamma_{endo})} (\boldsymbol{\eta}\circ\boldsymbol{\varphi})\cdot\mathbf{n}\ \mathrm{d}a\ .$$

In order to solve the non-linear saddle-point problem at hand, *Newton's linearisation method* is used. Let W be a Banach space and W^* its dual; given a generic functional $\mathcal{G} : W \to W^*$ with Gâteaux derivative $\mathrm{D}\mathcal{G} \in \mathcal{L}(W, W^*)$, we set an appropriate initial solution $x^0 \in W$, and for each iteration we find δx such that

$$\mathrm{D}\mathcal{G}(x^k)\ \delta x = -\mathcal{G}(x^k)\ , \tag{2.13}$$

which is the so-called tangent problem. Then, we compute $x^{k+1} = x^k + \delta x$ and repeat this process until a proper convergence criteria is satisfied: for instance, we can check that both the increment δx and the residual $\mathcal{G}(x^k)$ are smaller than a given tolerance in a suitable norm. In our case, we have $W = V \times Q \times R$ and $\delta x = (\delta\boldsymbol{\varphi},\ \delta p,\ \delta p_{inner})$.
For a the numerical solution of the problem at hand, the finite element method is used: given a proper computational mesh $\mathcal{T}_h$, we consider two finite dimensional spaces V_h and Q_h, which are subspaces of the functional spaces V and Q, respectively, so that we obtain the Galerkin formulation for the tangent problem. A proper choice for tetrahedral meshes is $V_h = \big[\mathbb{CG}^2\big]^3$ (displacement) and $Q_h = \mathbb{CG}^1$ (pressure), where

$$\mathbb{CG}^p(\Omega_0) := \Big\{u \in \mathcal{C}(\Omega_0) : u|_K \text{ is a polynomial of degree } p, \text{ for each element } K \in \mathcal{T}_h\Big\}\ .$$

The numerical simulation starts at the fictitious time $t = 0$ with the isovolumic contraction previously described: in this phase of the cardiac cycle, both the mitral and the aortic valve are closed; when the inner pressure is high enough to open the aortic valve, the ejection phase starts, and the blood is pumped into the arterial system. We point out that in our work we neglect the effects of the opening of the aortic valve: in the ejection phase, the variation of the inner volume and pressure is quite complex, depending on several physical effects such as the geometry of the valve, the arterial compliance and the resistance of the circulatory system. For the sake of simplicity, we set a fixed end-systolic pressure, which is kept constant during the whole systolic phase, and compute the volume from the corresponding deformation.
The diastolic phase is implemented in a similar way: when the activation parameter γ reaches its peak, the aortic valve closes and the ventricle undergoes an isochoric relaxation; the volume is kept constant and the fibres are not activated, until the ventricular pressure is less than the preload pressure $p_{preload}$. At this point, the mitral valve opens, and the ventricle is filled while keeping the pressure at a fixed value.

2.6 Geometry and definition of the microstructure

As discussed in Section 1.3, when performing a numerical simulation of the ventricular mechanics, a truncated ellipsoid is the most common computational geometry for the left ventricular cavity. The size and shape of the chamber may vary among biological species, and in this work we consider a canine ventricle: it is smaller than the human ventricle and its major axis is about two times longer than its minor one.
A common choice in the literature is the use of the *prolate coordinate system*: the position of a point in this coordinate system is given by the triplet (λ, μ, θ), where

$$\begin{cases} x &= d \sinh\lambda \sin\mu \cos\theta \ , \\ y &= d \sinh\lambda \sin\mu \sin\theta \ , \\ z &= d \cosh\lambda \cos\mu \ , \end{cases} \tag{2.14}$$

where d is the focal length, the coordinate $\lambda \geq 0$ denotes the distance from the longitudinal axis of the ventricle along an hyperbola, $\mu \in [0, \pi)$ is an angle that specifies the distance from the apex, and $\theta \in (0, 2\pi]$ is the circumferential coordinate. For a fixed value of λ, we get an ellipsoidal surface spanned by μ and θ, with major and minor axes equal to $d\cosh\lambda$ and $d\sinh\lambda$, respectively.
The apex is the only point in the geometry having $\mu = 0$, while the base is identified by $\mu = \frac{2}{3}\pi$ and the plane with $\mu = \frac{\pi}{2}$ is called *equator*. Additionally, we use the parameters $\lambda_{endo} = 0.4$ and $\lambda_{epi} = 0.7$, while the focal length for our canine geometry is $d = 3.7$ cm.

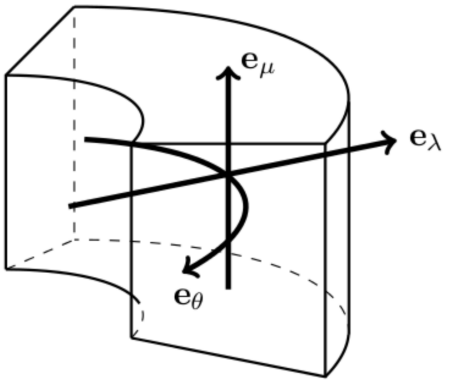

FIGURE 2.1: Local orthonormal basis in the prolate coordinate system.

Considering the domain,

$$\widetilde{\Omega}_0 := \left\{ (\lambda, \mu, \theta) : \lambda_{endo} < \lambda < \lambda_{epi}, 0 < \mu < \mu_{base}, 0 \leq \theta < 2\pi \right\} ,$$

the computational domain Ω_0, which is the ventricle in the reference configuration, is obtained by translating $\widetilde{\Omega}_0$ in order to have the basal plane at $z = 0$: the base is defined by $\Gamma_{base} = \overline{\Omega}_0 \cap \{z = 0\}$. In order to properly encode the distribution of fibres and sheets, we define the local orthonormal base $\left\{ \mathbf{e}_\lambda, \mathbf{e}_\mu, \mathbf{e}_\theta \right\}$ at a given point (λ, μ, θ) in the prolate coordinate system; the ventricular microstructure can be defined by linear combinations of $\mathbf{e}_\lambda$, $\mathbf{e}_\mu$ and $\mathbf{e}_\theta$. First, we introduce the normalized coordinate $\lambda_* \in [0, 1]$ which denotes the wall depth according to the definition:

$$\lambda_* := \frac{\lambda - \lambda_{endo}}{\lambda_{epi} - \lambda_{endo}} ,$$

so that $\lambda_* = 0$ denotes the endocardium and $\lambda_* = 1$ the epicardium. We introduce the helix angle $\alpha_{helix} : [0, 1] \to [-\frac{\pi}{2}, \frac{\pi}{2}]$, which is a function of λ_* due to the change of fibre orientation depending on the position in the myocardial wall, as explained in detail in Chapter 1. Consequently, we define the versor $\mathbf{f}_0$ that denotes the fibre orientation as follows:

$$\mathbf{f}_0 = \cos \alpha_{helix}(\lambda_*) \ \mathbf{e}_\theta + \sin \alpha_{helix}(\lambda_*) \ \mathbf{e}_\mu \ . \tag{2.15}$$

We point out that, in this case, the transverse angle of fibres is neglected, as $\mathbf{f}_0$ has no component along the radial direction $\mathbf{e}_\lambda$. The complete model for the ventricular microstructure will be discussed in detail in Chapter 3. In this chapter, we consider the simplest fibre angle configuration: the helix angle is $-60°$ at the endocardium, $+60°$ at

the epicardium, changes linearly inside the wall and is zero for $\lambda = \frac{1}{2}$. Thus, we have

$$\alpha_{helix}(\lambda_*) = \alpha_{endo}(1 - \lambda_*) + \alpha_{epi}\lambda_* \ , \tag{2.16}$$

where $\alpha_{endo} = -\frac{\pi}{3}$ and $\alpha_{epi} = \frac{\pi}{3}$. The sheets orientation can be defined in a similar way:

$$\mathbf{s}_0 = \sin\beta(\lambda_*)\ \Big(\sin\alpha_{helix}(\lambda_*)\ \mathbf{e}_\theta - \cos\alpha_{helix}(\lambda_*)\ \mathbf{e}_\mu\Big) + \cos\beta(\lambda_*)\ \mathbf{e}_\lambda \ , \tag{2.17}$$

recalling that the sheets must always be orthogonal to the fibres direction in each point. A commonly used expression for $\beta(\lambda_*)$ is

$$\beta(\lambda_*) = \beta_{endo}(1 - \lambda_*) + \beta_{epi}\lambda_* \ , \tag{2.18}$$

which is similar to the formula for the helix angle. Nevertheless, we point out that a simple, but viable choice is $\beta(\lambda_*) = 0$ for each λ_*: this means that $\mathbf{s}_0 = \mathbf{e}_\lambda$, and the myofibres are radially organized in laminar structures, referred to as *radial sheets*.

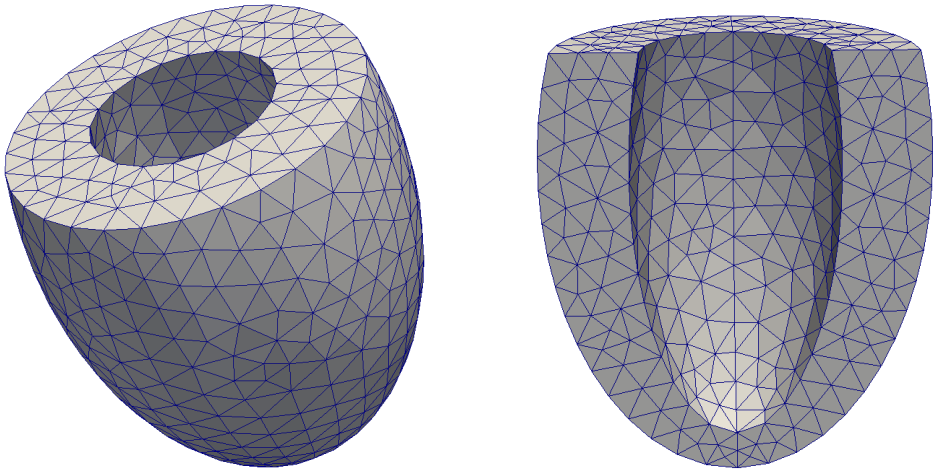

FIGURE 2.2: A simple computational mesh for the left ventricle: complete view and section.

2.7 Numerical results: reference configuration

In this section, we illustrate the results of a numerical simulation with a set of parameters that we take as a reference dataset; the mechanical model previously showcased has been implemented using the tools provided by the FEniCS project, a collection of software for the solution of partial differential equation through the finite element method (see Logg et al. 2012 for details).

The material parameters for the Holzapfel-Ogden model are the set of parameters proposed by Wang et al. (2013), reported in Table 2.1.

Parameters	a (kPa)	b	a_f (kPa)	b_f	a_w (kPa)	b_w	a_{fs} (kPa)	b_{fs}
Wang et al.	0.2362	10.810	20.037	14.154	3.7245	5.1645	0.4108	11.300

TABLE 2.1: Wang et al. (2013) material parameters.

The numerical simulations start with a passive inflation step, from the reference configuration up to the end-diastolic pressure $p_{preload} = 1$kPa; from this point, a complete cardiac cycle is performed. We start linearly increasing the activation parameter γ from 0 up to 0,2, reaching the end-systolic point with a pressure $p_{afterload} = 10$ kPa; then, γ is linearly decreased back to its starting value, and the cycle is completed.
In this simulation, we consider the simplest possible microstructure for the ventricle: the fibres have no transverse angle, thus their spatial configuration is described by (2.15); the helix angle is linear inside the wall, changing from $-60°$ at the endocardium to $+60°$ at the epicardium, as described in the previous section; sheets are radial, so that their orientation is given by $\mathbf{s}_0 = \mathbf{e}_\lambda$ and the sheet angle β is null in the whole wall. This basic microstructural configuration has been widely used in the literature, and it is considered to be an appropriate approximation for the ventricular structure.
Obviously, boundary conditions play an important role in the numerical model: in this case, we make the simplest choice, imposing zero mean rotation and zero mean translation in the whole computational domain, in order to avoid rigid motion. For a detailed discussion on how these conditions are applied, see Section 4.2. Additionally, we impose homogeneous Dirichlet boundary condition on the vertical displacement of the basal plane, so that the base remains fixed in the z-direction, while being free to displace in the $x - y$ plane.

Cardiac phase	**Volume**	**Pressure**	$\boldsymbol{\gamma}$
Reference configuration	32,37 ml	0,0 mmHg	0,0
End-Diastolic Point	40,32 ml	7,5 mmHg	0,0
Aortic Valve Opening	40,32 ml	75,0 mmHg	0,085
End-Systolic Point	17,75 ml	75,0 mmHg	0,2
Mitral Valve Opening	17,75 ml	7,5 mmHg	0,165

TABLE 2.2: A global picture of the cardiac cycle, with values for volume, pressure and activation parameter at key points of the pressure-volume loop for the reference simulation.

Table 2.2 reports the values of ventricular volume, inner pressure and activation parameter γ at key points of the cardiac cycle: in each phase, either the pressure or the volume

is kept constant, as we do not take into account the complex valve opening effect. Moreover, the variation of the activation parameter from 0 to 0,2 (at the end of systole) and back to 0 can be appreciated.

Indicator	**Value**
Stroke Volume	22,57 ml
Ejection Fraction	55,97 %
Thickening Base	27,91 %
Thickening Apex	31,17 %
Shortening	3,79 %
Height/Radius Ratio EDP	2,54 %
Height/Radius Ratio ESP	2,61 %
Torsion	10,03°

TABLE 2.3: Set of physiological indicators for the reference simulation.

In order to evaluate the consistency of the mathematical model with the physiological evidence, the set of physiological indicators introduced in Chapter 1 is an important element in our analysis. The values of physiological quantities computed in the post-processing step of the simulation is reported in Table 2.3.

During the systolic phase, the inner volume of the ventricle decreases from 40,32 ml to 17,75 ml, yielding a stroke volume of 22,57 ml and a corresponding ejection fraction of 55,97%, a value well within the physiological range for a healthy heart.

The thickening of the wall is another important quantity, as it is one of the most important indicators of the cardiac mechanics. It is computed in two different transverse sections: one close to the base and one close to the apex, and a higher apical thickening is registered. These values are close to the ones computed by Streeter et al. (1969) for a canine heart, but higher thickening measures have been reported in the literature (Conti et al. 2011).

On the other hand, the computed ventricular shortening is far from reported data, as the physiological evidence shows that it should reach 20% or higher. We point out that volume conservation relates shortening and wall thickening, because we are considering an incompressible model for the cardiac tissue. In addition, shortening can be greatly influenced by the fibre orientation in the myocardium, as we will discuss in detail in the next chapter.

The ratio between the height of the ventricle and the basal radius is also considered, as it should remain almost constant during the whole cycle: we report the values at the end-diastolic and end-systolic point, assuming that a variation within the 10% range is acceptable.

The ventricular torsion is computed according to the following formula:

$$\theta = \frac{\phi_{apex} r_{apex} - \phi_{base} r_{base}}{D} \quad .$$

Given one basal and one apical section of the ventricle, separated by a distance D, we select one point per section, $\mathbf{X}_{base}$ and $\mathbf{X}_{apex}$, which are aligned in the reference configuration. Considering their actual placement $\mathbf{x}_{base}$ and $\mathbf{x}_{apex}$, respectively, we can compute for both sections:

$$R = \|\mathbf{X} - (\mathbf{X} \cdot \mathbf{e}_3)\ \mathbf{X}\| \ , \quad r = \|\mathbf{x} - (\mathbf{x} \cdot \mathbf{e}_3)\ \mathbf{x}\| \ , \quad \sin\phi = \frac{\mathbf{x} \wedge \mathbf{X} \cdot \mathbf{e}_3}{rR} \ ,$$

and, consequently, the torsion. The value reported in the table is computed at the end-systolic point with $\mathbf{X}$ on the epicardium, and it falls in the physiological range.

Figure 2.3 provides quite a complete view on the mechanical behaviour of the ventricle during the whole cardiac cycle, thanks to the graphic visualization of Green-Lagrange strain and Cauchy stress at different transmural positions. The radial strain $E_{\lambda\lambda}$ is notably higher at the sub-endocardium with respect to the sub-epicardium, because during the systolic phase the inner volume greatly decreases, even if the radial strain at the sub-epicardium is smaller, and the difference between the two strains provides a measure of the wall thickening effect; in a similar way, the longitudinal strain $E_{\mu\mu}$ is closely related to the shortening of the ventricle. On the other hand, the circumferential strain $E_{\theta\theta}$ has a relevant transmural variation, being about ten times bigger at the endocardium than at the epicardium. Regarding the off-diagonal components of the strain, the most important one is the circumferential-longitudinal shear $E_{\mu\theta}$, which is often used as a measure of the torsion and has an important role in ventricular mechanics: as a matter of fact, it usually takes high values, around -10%. Moreover, the analysis of the stress distribution in the myocardial wall shows a peak at the end-systolic point, as a result of the exponential form of the strain energy encoded in the Holzapfel-Ogden model.

Furthermore, the plots of the principal strain invariants provide additional informations on the mechanical state of the ventricle during the cardiac cycle (Figure 2.4): all of them exhibit a peak at the end of systole, as expected. For instance, the plot for $\mathcal{I}_{4,\mathbf{f}_0}$ is particularly meaningful, as this invariant is closely related to the stretch of myofibres: as we can see, sub-epicardial fibres undergo a slightly higher shortening with respect to sub-endocardial ones, but this behaviour has no physiological validation. We point out that, during the isochoric contraction phase, between the end-diastolic point and the aortic valve opening, we find $\mathcal{I}_{4,\mathbf{f}_0} > 0$, which means that fibres are in tensile regime, stretching over their resting length, as a result of the passive expansion of the ventricle during the filling phase. As a matter of fact, we find a possible issue in this phase of the

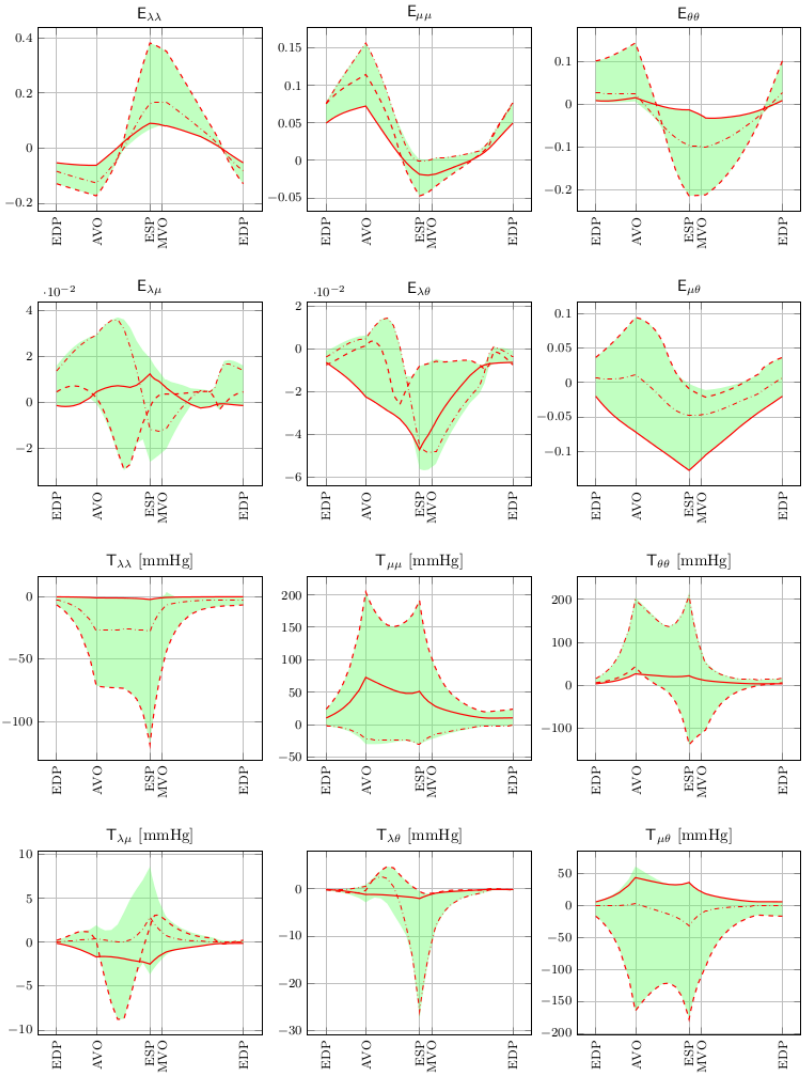

FIGURE 2.3: Plot of Green-Lagrange strain (first two rows) and Cauchy stress (last two rows) components during the cardiac cycle for the reference simulation. The lines refer to the sub-epicardium (solid line), sub-endocardium (dashed line), and mid-myocardium (dash-dotted line). The green area represents the range of values spanned in the radial direction. The data are taken in a mid-axis section of the ellipsoid.

cardiac cycle: the graph for the height of the ventricle (computed as the distance from apex to base) shows that the ventricle elongates during the isochoric contraction (Figure 2.5); this behaviour has no physiological basis, because in this phase the longitudinal length of the ventricle should remain almost unchanged, with at most a slight shortening of the chamber.

Last but not least, the plots for strain-energy density show that $\mathcal{W}_{4,\mathbf{f}_0}$ is the dominant term, while $\mathcal{W}_1$ and $\mathcal{W}_{4,\mathbf{s}_0}$ only show relevant peaks at the end of systole, taking values one order of magnitude lower than $\mathcal{W}_{4,\mathbf{f}_0}$; $\mathcal{W}_{8,\mathbf{f}_0\mathbf{s}_0}$ takes very low values, too, and this confirms the fact that the fibrous structure plays the most important role in the cardiac mechanics (Figure 2.4).

The analysis of the cardiac mechanics can be tackled from a different perspective, related

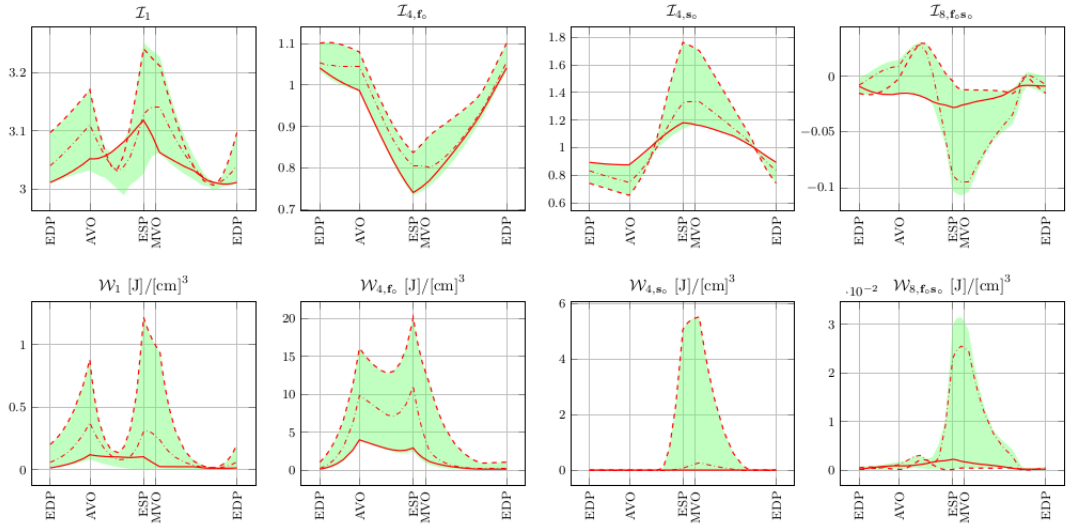

FIGURE 2.4: Plot of invariants and their corresponding strain-energy density during the cardiac cycle for the reference simulation. The lines refer to the sub-epicardium (solid line), sub-endocardium (dashed line), and mid-myocardium (dash-dotted line). The green area represents the range of values spanned in the radial direction. The data are taken in a mid-axis section of the ellipsoid.

to the rotation of the endocardial and epicardial surfaces during the PV-loop. This approach is closely related to the nature of two different shear deformations:

- *longitudinal torsion* : the rotation of the apex with respect to the base, associated to the circumferential-longitudinal shear stress $\mathsf{T}_{\theta\mu}$;
- *transmural shear* : the rotation of the endocardium with respect to the epicardium, associated to the circumferential-radial shear stress $\mathsf{T}_{\theta\lambda}$.

They are both generated by the asymmetric distribution of the fibres, as the activation of epicardial fibres induces a rotation opposite to the one of endocardial fibres, thanks to their opposite orientation (see Chapter 1, Figure 1.12 for an effective visual representation); obviously, the epicardial fibres have a longer arm, so the force balance is in their favour.

An effective way for a general view on shear deformations is provided by Figure 2.6, where the rotation for several points on the epicardial surface is reported at key points of the PV-loop. In addition, the transmural shear is depicted for two different axial sections, an apical and a basal one. During the systole, the apex rotates counterclockwise, while the base performs a clockwise rotation; on the other hand, near the basal plane, the epicardium rotates clockwise and the endocardium moves in the opposite direction: this behaviour is consistent with the theoretical analysis proposed by Ubbink et al. (2009), and makes sense from the mechanical point of view. Nevertheless, the transverse shear reported in the physiological literature (for instance, Young et al. 2009) is quite different:

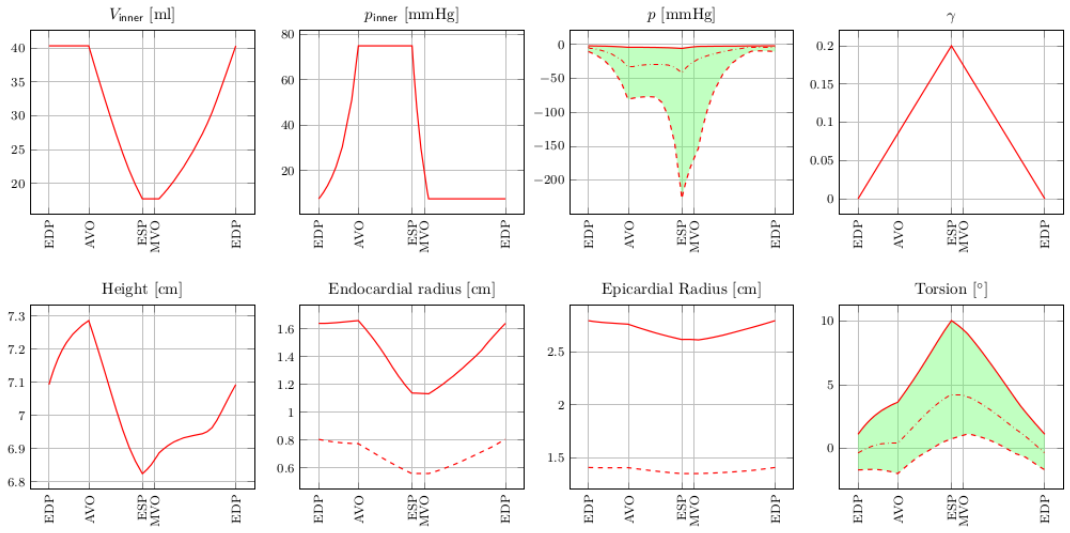

FIGURE 2.5: Plot of ventricular volume, pressure, activation parameter, ventricular height, endocardial and epicardial radius, and torsion during the cardiac cycle for the reference simulation. In the plots for the radii, the solid and dashed line refer to a basal and an apical section, respectively. In the case of pressure and torsion, the lines refer to the sub-epicardium (solid line), sub-endocardium (dashed line), and mid-myocardium (dash-dotted line), and the green area represents the range of values spanned in the radial direction.

the rotation in a given axial plane of inner and outer points should occur in the same direction, and in addition a greater endocardial rotation is registered. Apparently, this is a mechanical paradox, as sub-epicardial fibres have a longer arm, and thus should dictate the ventricular rotation and torsion: as a consequence, a larger epicardial rotation should

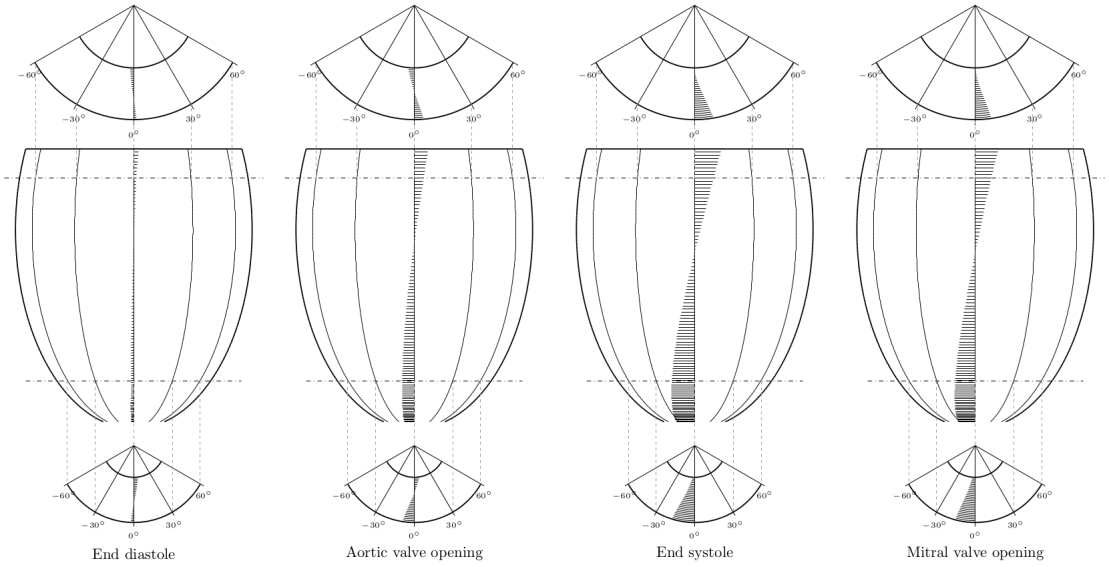

FIGURE 2.6: Ventricular torsion in four different phases of the cardiac cycle for the reference simulation. Top and bottom figures represent the in-plane transversal rotation in a basal and apical section, while the figures in the middle strip refers to the epicardial rotation.

be observed.
Pezzuto et al. (2014) suggested that the mechanical explanation of this result could lie in the laminar structure, as the fibres have a circumferential component and sheets are radial, so that the transverse shear is measured by the eight invariant $\mathcal{I}_{8,\mathbf{f}_0\mathbf{s}_0}$. On the other hand, according to Bovendeerd et al. (2009), this mechanical behaviour could be explained by the presence of a non-zero transverse fibre angle.

In summary, in this chapter we have discussed a mechanical and numerical model for the ventricular mechanics and we have performed and analysed a simple simulation under reference conditions, obtaining results that mostly fit the physiological evidence; however, some mechanical features deserve to be further investigated. In the following chapter, we try to refine this model, focusing on the microstructure of the myocardium, which is the key of the mechanical behaviour of the ventricle during the cardiac cycle.

CHAPTER 3

MICROSTRUCTURAL MODELLING

Introduction

The nature of the myocardial microstructure has a notable impact on the ventricular mechanics, as the contraction of fibres dictates the twitch and determines most physiological quantities of the cardiac cycle, such as ejection fraction and wall thickening. Crucial issues are not only the fibre orientation at the sub-endocardium and at the sub-epicardium, but also the variation of the fibre angle across the wall thickness: as a matter of fact, the fibre distribution can even be asymmetric, the variation of the fibre angle can be faster in the proximity of the endocardial and epicardial surface, or, in contrast, the highest variation could be in the proximity of the midwall, with an almost constant fibre angle near myocardial borders. In this chapter, we focus on the analysis of the effects of the configuration of fibre angle on the strain and stress distribution in the myocardial tissue using a finite element scheme; another purpose is to find which fibre distribution results in the most accurate reproduction for physiological quantities registered from medical studies on healthy ventricles, based on the set of indicators of the ventricular performance previously introduced. In order to accomplish this task, we neglect the mechanical influence of the laminar structure: this is a common choice for numerical models found in the literature, as it has been shown that the sheet structure does not have a noticeable impact on physiological quantities. In addition, the laminar structure has a complex variability, and the presence of two difference populations of laminar sheets has been found in the human heart (Lombaert et al. 2012); as a consequence, the modelling of the distribution of sheets in the myocardium could be quite challenging. In addition, it has been shown that the solution of the mechanical model is not particularly sensitive on the variability of sheets (Pezzuto et al. 2014). Thus, we first consider a set a simulations

based on the transversely isotropic mechanical model, in order to properly analyse the impact of the fibre distribution on the cardiac cycle; then, we evaluate the mechanical influence of the addition of the laminar structure, using the full orthotropic model.

3.1 The transversely isotropic model

In the present section, we discuss a numerical simulation based on the transversely isotropic version of Holzapfel-Ogden model, which can be simply obtained by setting the material parameters $a_s = b_s = a_{fs} = b_{fs} = 0$, so that the invariants associated with the laminar structure $\mathcal{I}_{4,\mathbf{s}_0}$ and $\mathcal{I}_{8,\mathbf{f}_0\mathbf{s}_0}$ are neglected in the mechanical model; thus, the strain-energy density function depends on $\mathcal{I}_1$ and $\mathcal{I}_{4,\mathbf{f}_0}$, and the ventricular microstructure is fully determined by the muscle fibre orientation. This is a common approach for the application of numerical models using the finite element method, because it provides a simple but effective overview on the mechanical influence of fibre distribution on the ventricular mechanics (see, for instance, Bovendeerd et al. 1994).
Our starting point is a linear distribution of the helix angle, with no transverse angle. Thus, the microstructural configuration is described by the fibre angle and orientation as follows:

$$\alpha_{helix}(\lambda_*) = \alpha_{endo}(1 - \lambda_*) + \alpha_{epi}\lambda_* \ ,$$
$$\mathbf{f}_0 = \cos\alpha_{helix}(\lambda_*)\ \mathbf{e}_\theta + \sin\alpha_{helix}(\lambda_*)\ \mathbf{e}_\mu \ ,$$

where $\alpha_{endo} = -\frac{\pi}{3}$ and $\alpha_{epi} = \frac{\pi}{3}$. This configuration is similar to the fibre configuration used for the simulation presented in the previous chapter: we are simply using the transversely isotropic model instead of the orthotropic one. As a matter of fact, a direct comparison with the reference simulation can provide useful informations on the role of the laminar structure in myocardial mechanics.

Cardiac phase	**Volume**	**Pressure**	γ
Reference configuration	32,37 ml	0,0 mmHg	0,0
End-Diastolic Point	41,07 ml	7,5 mmHg	0,0
Aortic Valve Opening	41,07 ml	75,0 mmHg	0,085
End-Systolic Point	17,30 ml	75,0 mmHg	0,2
Mitral Valve Opening	17,30 ml	7,5 mmHg	0,141

TABLE 3.1: A global picture of the cardiac cycle, with values for volume, pressure and activation parameter at key point of the PV-loop for the transversely isotropic simulation.

A comparison of Tables 3.1 and 2.2 reveals that the lack of the laminar structure produces a slightly higher volume after the initial inflation (41,07 ml instead of 40,32 ml), and both the stroke volume (23,77 ml) and the ejection fraction (57,87%) are notably higher, resulting in a more efficient ventricle. As a matter of fact, it is clear that the addition of laminar sheets that are constituted by fibres along the radial direction increases the stiffness of the ventricle, and without such structures the contraction of the ventricle is facilitated.

Indicator	**Value**
Stroke Volume	23,77 ml
Ejection Fraction	57,87 %
Thickening Base	30,22 %
Thickening Apex	32,69 %
Shortening	4,64 %
Height/Radius Ratio EDP	2,54 %
Height/Radius Ratio ESP	2,59 %
Torsion	10,57°

TABLE 3.2: Set of physiological indicators for the transversely isotropic simulation.

While the value for torsion exhibits no significant differences with respect to the orthotropic case, the wall thickening is higher near the base and notably lower in the proximity of the apex. Additionally, an increase of ventricular shortening during the cardiac cycle is registered.

The transversely isotropic model implies that there is no strain energy associated with the sheet structure, and, as a consequence, the energy related other invariants must be higher; in fact, the value of $\mathcal{W}_1$ at the end-systolic point is higher than the energy density registered in the orthotropic case. On the other hand, the temporal variation of the strain energy associated to $\mathcal{I}_{4,\mathbf{f}_0}$ is interesting: while the peak at the end of the isochoric

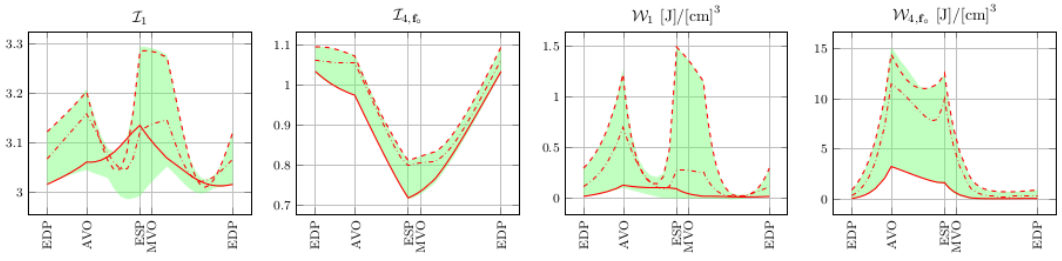

FIGURE 3.1: Plot of invariants and their corresponding strain-energy density during the cardiac cycle for the transversely isotropic case. The lines refer to the sub-epicardium (solid line), sub-endocardium (dashed line), and mid-myocardium (dash-dotted line). The green area represents the range of values spanned in the radial direction. The data are taken in a mid-axis section of the ellipsoid.

contraction phase is comparable with the one registered in the orthotropic simulation, the end-systolic peak is notably lower, and results in an almost constant strain-energy density in the whole ejection phase.
In conclusion, the small influence of the sheet structure on the mechanical behaviour of the left ventricle during the cardiac cycle can be confirmed: the spatial orientation of myofibres is the principal determinant of the distribution of deformation and stress in the left ventricle.

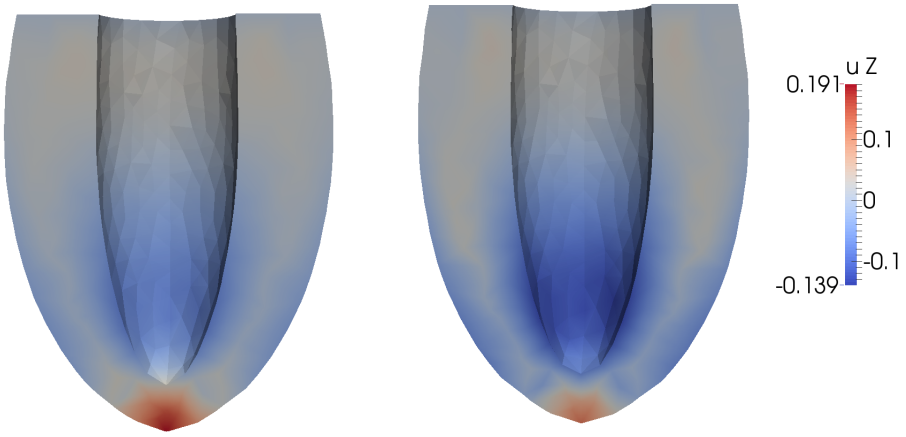

FIGURE 3.2: Vertical displacement in a section of the left ventricle at end systole for the transversely isotropic case. There are no relevant differences between the orthotropic case (on the left) and transversely isotropic case (on the right).

3.2 Helix angle distribution

In previous works, a sensitivity analysis for the fibre configuration has been performed, but only in the case of a linear distribution of fibre angle, considering different endocardial and epicardial values (Pezzuto et al. 2014). In contrast, our purpose is to evaluate the mechanical impact of a different variation of the helix angle across the myocardial wall: in order to do this, we keep the endocardial and epicardial values of α_{helix} fixed and equal to $-\frac{\pi}{3}$ and $\frac{\pi}{3}$, respectively. Then, we change the law of fibre orientation, considering three different forms on non-linearity for the helix angle in the wall thickness: an asymmetric distribution which results in a non-zero helix angle at the middle of the wall, an high variation in the sub-endocardial and sub-epicardial regions, and an high variation in the proximity of the midwall, referred to as bimodal distribution of fibres.

3.2.1 Asymmetric distribution

In order to study the effects of an asymmetric fibrous structure, a 'quasi-linear' variation of the helix angle across the wall thickness is considered: in this case, fibres at the midwall are not circumferential, which means they have a non-zero helix angle. Thus, myofibres have a prevalent right-handed or left-handed orientation, which can greatly affect the ventricular mechanics.
Thus, the helix angle, which is a function of the normalized radial coordinate λ_*, is here defined as follows:

$$\alpha_{helix}(\lambda_*) = \alpha_{mid} + \alpha_{epi}(2\lambda_* - 1) - \begin{cases} 4\ \alpha_{mid}(2\lambda_* - 0.5)^2 & 0 \leq \lambda_* \leq 0.25 \\ 0 & 0.25 < \lambda_* \leq 0.75 \\ 4\ \alpha_{mid}(2\lambda_* - 1.5)^2 & 0.75 < \lambda_* \leq 1 \end{cases} \tag{3.1}$$

where $\alpha_{epi} = \frac{\pi}{3}$ is the epicardial fibre angle, while the helix angle at the epicardium takes the same value with an opposite sign. On the other hand, α_{mid} denotes helix angle at the middle of the myocardial wall: we choose four different values for this parameter, ranging from $-15°$ to $+15°$. Note that for $\alpha_{mid} = 0$ the linear distribution of the fibre angle is recovered. A negative value for α_{mid} means that, at midwall, fibres have a right-handed orientation, similarly to the sub-endocardial layer, while if $\alpha_{mid} > 0$ myofibres are left-handed. The variation of the helix angle in the middle half of the ventricular wall is linear, while the function is quadratic in the sub-endocardial and sub-epicardial layers in order to match the values at the borders (Figure 3.3).

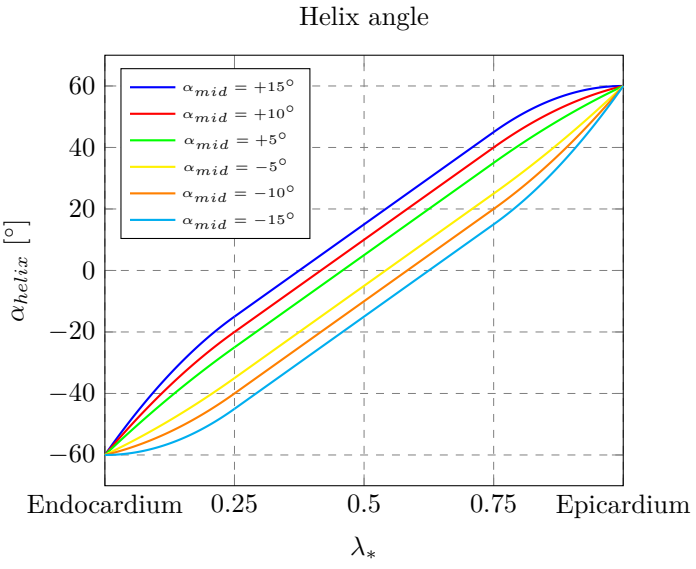

FIGURE 3.3: Transmural variation of helix angle for an asymmetric distribution for different values of α_{mid}.

This particular fibre configuration has been validated both by physiological and numerical researches: a similar distribution of fibres was used by Bovendeerd and co-workers in a number of numerical projects (Bovendeerd et al. 1994), and the non-circumferential orientation of fibres at the middle of the cardiac wall has been reported in several histological studies (Streeter et al. 1979). In these cases, the fibre angle was considered to be positive at the midwall, while in other works (such as Streeter et al. 1969) it had an opposite sign: in order to fully analyse the influence on cardiac mechanics, we test both cases.

Indicator	$\alpha_{mid} = -15°$	$\alpha_{mid} = -10°$	$\alpha_{mid} = -5°$	$\alpha_{mid} = 5°$	$\alpha_{mid} = 10°$	$\alpha_{mid} = 15°$
Stroke Volume	26,49 ml	25,55 ml	24,64 ml	22,96 ml	22,22 ml	21,55 ml
Ejection Fraction	62,52 %	60,98 %	59,42 %	56,40 %	55,09 %	53,78 %
Base Thickening	33,93 %	32,59 %	31,33 %	29,32 %	28,65 %	28,22 %
Apex Thickening	34,94 %	34,36 %	33,64 %	31,52 %	30,15 %	28,64 %
Shortening	3,13 %	3,43 %	3,94 %	5,52 %	6,57 %	7,75 %
Torsion	7,20°	8,31°	9,44°	11,70°	12,79°	13,83°

TABLE 3.3: Set of physiological indicators for the set of simulations with a quasi-linear helix angle configuration.

First of all, we notice that, for $\alpha_{mid} < 0$, stroke volume and ejection fraction are higher, resulting in a more efficient ventricle: as a matter of fact, if this fibre configuration is considered, there are more right-handed fibres than the left-handed one, and their shortening facilitates the contraction of the inner chamber. On the other hand, if there are more left-handed fibres, which means that α_{mid} is positive, stroke volume and ejection fraction are reduced.

The thickening of the ventricular wall does not undergo significant variations with the change of orientation, slightly decreasing (around 5% lower) for positive α_{mid} at the base, and similarly in the apical region. On the contrary, the ventricular shortening is considerably higher with the increase of the angle at midwall, reaching values close to the shortening observed in healthy heart for the highest value of α_{mid}: we point out that, in this case, the ventricle experiences only a slight lengthening in the isochoric contraction phase, thus producing an overall higher shortening computed between the end-diastolic and the end-systolic point; nevertheless, there is no physiological validation for an increase of ventricular longitudinal length during the isovolumic contraction.

As expected, the torsion is greatly affected by the change of fibre angle: as a matter of fact, the circumferential-longitudinal shear is generated by the asymmetric distribution of fibres, and the biggest contribution comes from epicardial fibres, due to their longer arm. If the majority of fibres have a positive helix angle, the ventricle undergoes a relevant epicardial rotation, resulting in high values of $E_{\mu\theta}$ especially at the end of systole.

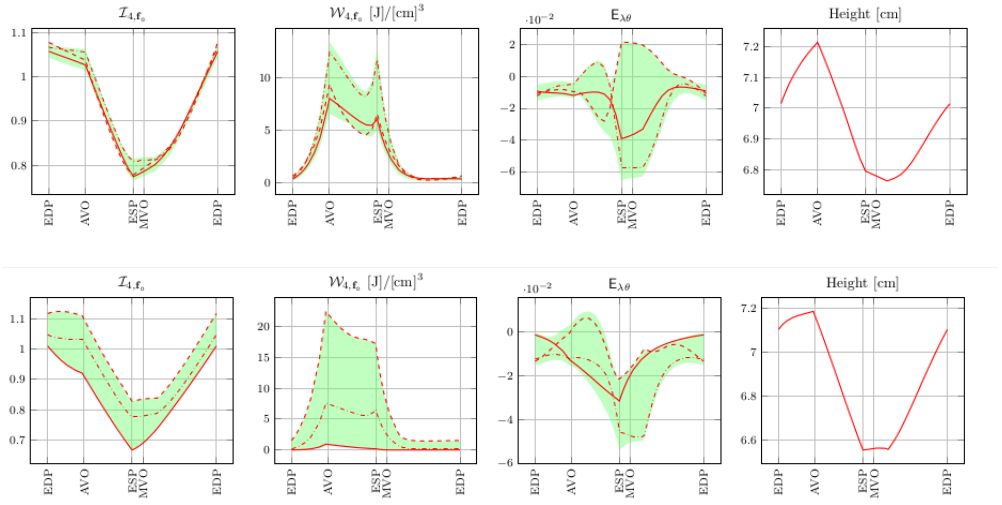

FIGURE 3.4: Plots for the fourth invariant and the corresponding strain-energy, circumferential-radial strain, and ventricular height for an asymmetric fibre distribution with $\alpha_{mid} = -15°$ (top row) and $\alpha_{mid} = +15°$ (bottom row). The lines refer to the sub-epicardium (solid line), sub-endocardium (dashed line), and mid-myocardium (dash-dotted line). The green area represents the range of values spanned in the radial direction. The data are taken in a mid-axis section of the ellipsoid.

This phenomenon is particularly noticeable from the graphic representation of epicardial rotation, reported for the lowest and highest values for α_{mid} (Figure 3.5). In addition, a similar impact is registered in the circumferential-radial shear $E_{\lambda\theta}$: the endocardial rotation in the proximity of the apex is found to be clockwise for $\alpha_{mid} = -15°$ and counterclockwise for $\alpha_{mid} = +15°$, as viewed from the apex.

Another important difference in the results is found in the spatial distribution of the

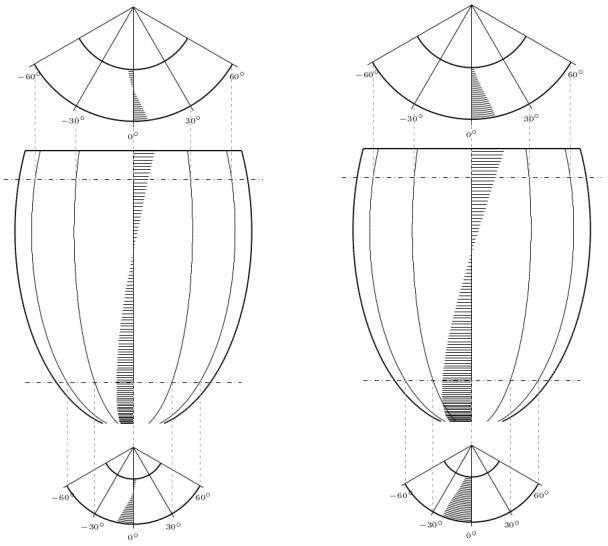

FIGURE 3.5: End-systolic torsion for an asymmetric fibre distribution with $\alpha_{mid} = -15°$ (on the left) and $\alpha_{mid} = +15°$ (on the right).

fourth invariant $\mathcal{I}_{4,\mathbf{f}_0}$, which accounts for the fibre shortening: activated epicardial fibres perform a higher shortening if the midwall helix angle is positive, being approximatively 20% shorter than endocardial fibres at end systole for $\alpha_{mid} = +15°$. In contrast, in the case $\alpha_{mid} = -15°$ the fibre contraction has almost the same magnitude in the entire wall, with a slightly higher endocardial shortening. A similar trend is found in the spatial variation of the strain-energy density associated with $\mathcal{I}_{4,\mathbf{f}_0}$ (Figure 3.4).

3.2.2 High variation of helix angle near myocardial borders

Several physiological researches registered a fast variation of fibre angle in the sub-endocardial and sub-epicardial layers of the myocardium, and such myofibre distribution can greatly affect the ventricular mechanics, as, in this configuration, the majority of muscle fibres are oriented circumferentially (Streeter et al. 1969).

In this section, the variation of the helix angle in the myocardial wall is set according to the following formula:

$$\alpha_{helix}(\lambda_*) = \alpha_{epi}(2\lambda_* - 1)^n \ , \tag{3.2}$$

where α_{epi} is the epicardial fibre angle, equal to $\frac{\pi}{3}$ as usual, whereas the helix angle at the endocardium is equal to $-\alpha_{epi} = -\frac{\pi}{3}$. The parameter n is an odd integer that specifies the steepness of α_{helix} near the myocardial borders: the higher n, the faster is the spatial variation of the helix angle in the sub-endocardium and in the sub-epicardium; as a consequence, for high values of n the distribution of fibre angle is almost constant near the middle of the myocardial wall and characterized by a high percent of circumferential

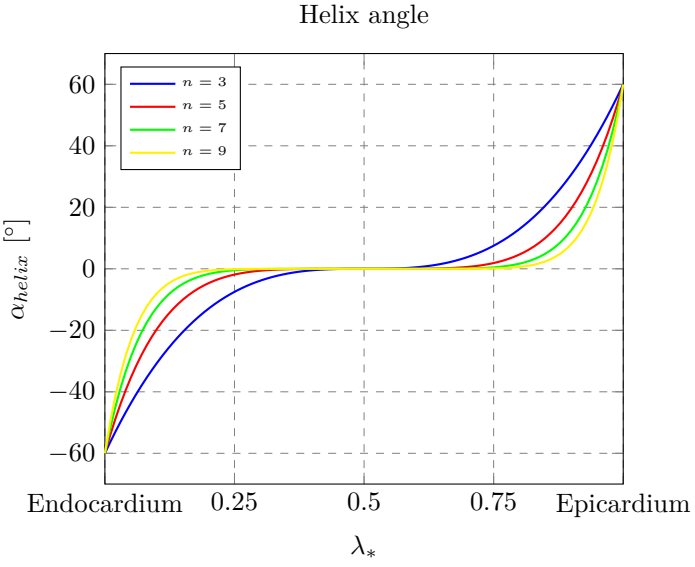

FIGURE 3.6: Transmural variation of helix angle for a fibre configuration characterized by an high variation of angle near myocardial borders for different values of n.

fibres. We point out that, if $n = 1$, the distribution of the helix angle is linear. In our case n is chosen in the set $\{3, 5, 7, 9\}$, and for $n = 9$ fibres are almost circumferential for $0.2 < \lambda_* < 0.8$ (Figure 3.6).

Indicator	$n = 3$	$n = 5$	$n = 7$	$n = 9$
Stroke Volume	23,39 ml	23,50 ml	23,64 ml	23,77 ml
Ejection Fraction	55,74 %	55,69 %	55,97 %	56,30 %
Base Thickening	25,77 %	25,08 %	25,30 %	25,63 %
Apex Thickening	18,88 %	12,10 %	8,65 %	6,61 %
Shortening	3,41 %	3,92 %	4,47 %	4,97 %
Torsion	10,78°	9,91°	9,10°	8,46°

TABLE 3.4: Set of physiological indicators for the simulations with an high variation of helix angle at the sub-endocardium and sub-epicardium.

No significant changes in stroke volume and ejection fraction are registered: in this case, in fact, circumferential fibres induce the contraction of the ventricular cavity, and the ventricular pump retains its efficiency even for high values of n. The same trend is found in basal wall thickening, with no particular increasing or decreasing trend with the increase of n. On the other hand, the thickening in the apical zone is notably lower with respect to the simulation discussed in Section 3.1: the value for wall thickening is about 6% for $n = 9$, which highlights the non-physiological behaviour reported this indicator; this effect could be due to the lowering of the portion of oblique fibres which causes a

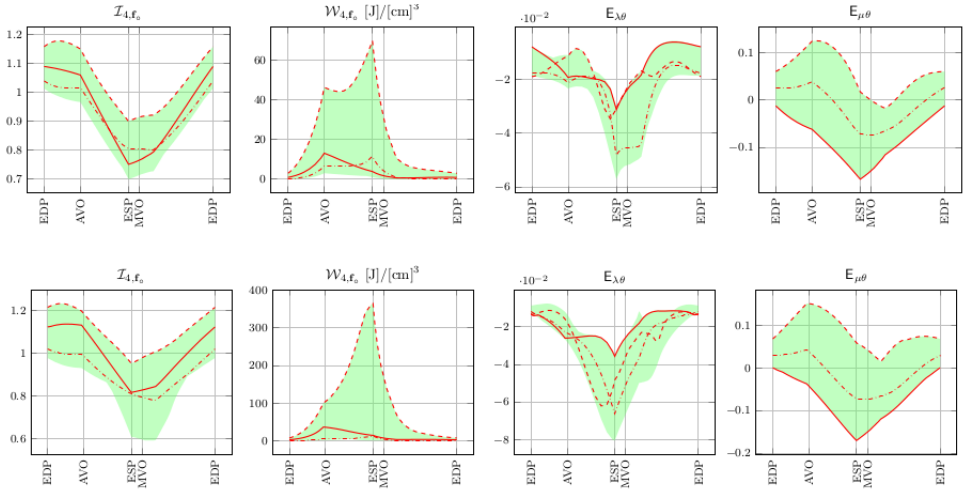

FIGURE 3.7: Plots for the fourth invariant and the corresponding strain-energy, circumferential-radial strain, and circumferential-longitudinal strain for $n = 3$ (top row) and $n = 9$. (bottom row). The lines refer to the sub-epicardium (solid line), sub-endocardium (dashed line), and mid-myocardium (dash-dotted line). The green area represents the range of values spanned in the radial direction. The data are taken in a mid-axis section of the ellipsoid.

stiffness reduction in the longitudinal direction. In contrast, the shortening of the ventricular chamber is insufficient from the physiological point of view, similarly to the case with a linear distribution of α_{helix}; this indicator only experiences a slight increase (up to 1,5%) for higher values of n.

In a similar way, torsion exhibits a moderate decrease for increasing n: the ventricular twitch is generated by the contraction of oblique fibres, in particular left-handed epicardial fibres which take advantage of their longer arm; as a consequence, if most fibres are oriented circumferentially, a lower number of longitudinal fibres produces a reduced twist. Intuitively, the less oblique fibres (higher n), the lower the ventricular torsion.

The reported values for the invariant $\mathcal{I}_{4,\mathbf{f}_0}$ show that the maximum fibre shortening is registered in the proximity of the middle of the ventricular wall (Figure 3.7): the circumferential fibres experience the higher length reduction. Higher values are registered for the strain-energy density associated to the fibrous structure, with notable end-sistolic peaks (more than 300 J/cm^3 for $n = 9$) located in the endocardial region.

As a side note, Figure 3.8 (referred to the case $n = 9$) shows that the endocardial rotation is higher than the epicardial rotation, but only in the diastolic phase: this physiological behaviour has been widely reported in the literature (Young et al. 2012). Nevertheless, this behaviour should also occur in the end-systolic phase, while our model yielded opposite rotations.

In conclusion, this fibre configuration does not lead to an improvement of the mechanical behaviour of the model: it does not significantly change the ventricular efficiency, while it yields a reduction of apical wall thickening and ventricular torsion. In addition, features that do not agree with the physiological evidence are not improved: the shortening value

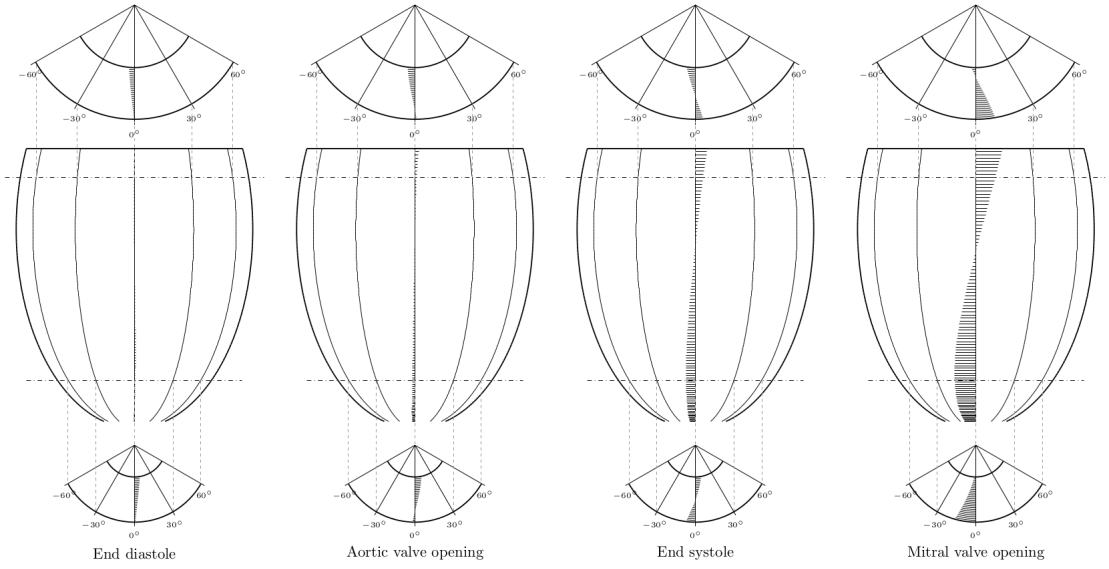

FIGURE 3.8: Ventricular torsion in four different phases of the cardiac cycle for $n = 9$. Top and bottom figures represent the in-plane transversal rotation in a basal and apical section, while the figures in the middle strip refers to the epicardial rotation.

is below the physiological level, and the lengthening of the ventricular chamber during the isochoric contraction phase is still registered.

3.2.3 Bimodal helix angle distribution

In this section, we test a different fibre configuration, characterized by a higher number of oblique (longitudinal) fibres with respect to circumferential ones. This particular myofibre distribution is not widely supported by histological researches, but has already been used for a numerical model of the cardiac mechanics (see, for instance, Carapella et al. 2014). In particular, we conjecture that this particular fibre architecture can greatly improve the ventricular efficiency, due to a greater longitudinal stiffness of the myocardial tissue.
We consider a fibre distribution described by the helix angle defined as follows:

$$\alpha_{helix}(\lambda_*) = \alpha_{epi}(2\lambda_* - 1)^{\frac{1}{n}} \ , \tag{3.3}$$

where $\alpha_{epi} = -\alpha_{endo} = \frac{\pi}{3}$ as usual. With this fibre configuration, there are very few circumferential fibres, as the change in helix angle is high at the midwall: we have a *bimodal* fibre distribution, as most cardiac fibres are left-handed or right-handed. The higher n, the faster the variation of orientation, and for high values of n more than 90% of the fibres have $\alpha_{helix} < -40°$ (in the sub-endocardium) or $\alpha_{helix} > 40°$ (in the sub-epicardium).

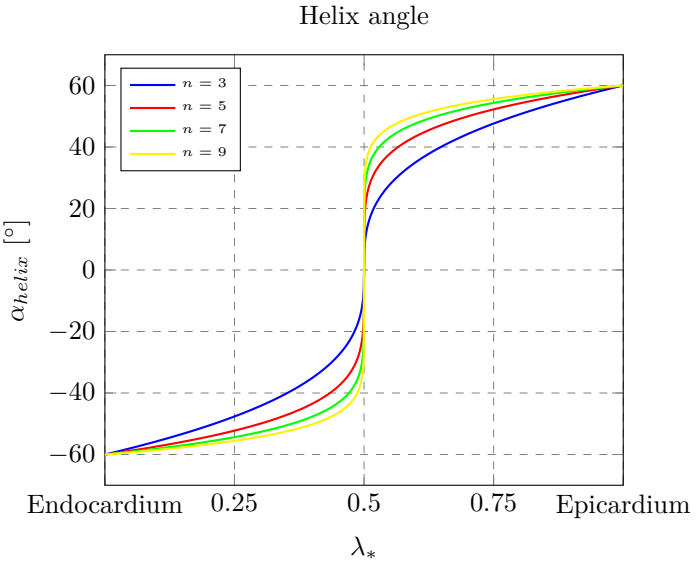

FIGURE 3.9: Transmural variation of helix angle for a bimodal fibre distribution for different values of n.

Indicator	$n = 3$	$n = 5$	$n = 7$	$n = 9$
Stroke Volume	25,79 ml	27,53 ml	28,36 ml	28,21 ml
Ejection Fraction	61,30 %	61,39 %	59,85 %	57,36 %
Base Thickening	35,12 %	36,80 %	37,23 %	36,82 %
Apex Thickening	41,90 %	44,42 %	43,84 %	41,28 %
Shortening	8,42 %	10,02 %	11,32 %	12,87 %
Torsion	8,42°	7,69°	7,40°	7,32°

TABLE 3.5: Set of physiological indicators for the simulations with a bimodal helix angle distribution.

The most relevant feature of the bimodal configuration is that, as most muscle fibre are oriented with an high helix angle, they provide a strong longitudinal reinforcement, resulting in a stiffer ventricle in the longitudinal direction. This effect is particularly evident from the plot of the height of the ventricle during the cardiac cycle: the end-diastolic value is lower than 6,7 cm for every n, while in the case with a linear helix angle (Section 3.1) the starting point is about 7,1 cm. In addition, we have a completely different behaviour in the isochoric contraction phase: the ventricle undergoes a slight shortening, with a non-linear decrease in height (Figure 3.10). This is an important improvement with respect to previous simulations, as this fact is supported by physiological studies. Moreover, the magnitude of the shortening during systole is of the order of the one obtained from previous simulations, resulting in a notably shorter ventricle at the end-systolic points, with values as low as about 5,3 centimetres for $n = 9$. As a consequence, a shorter ventricle with a similar variation in height during systole means that percent shortening values are significantly higher: these values range from 8,42%

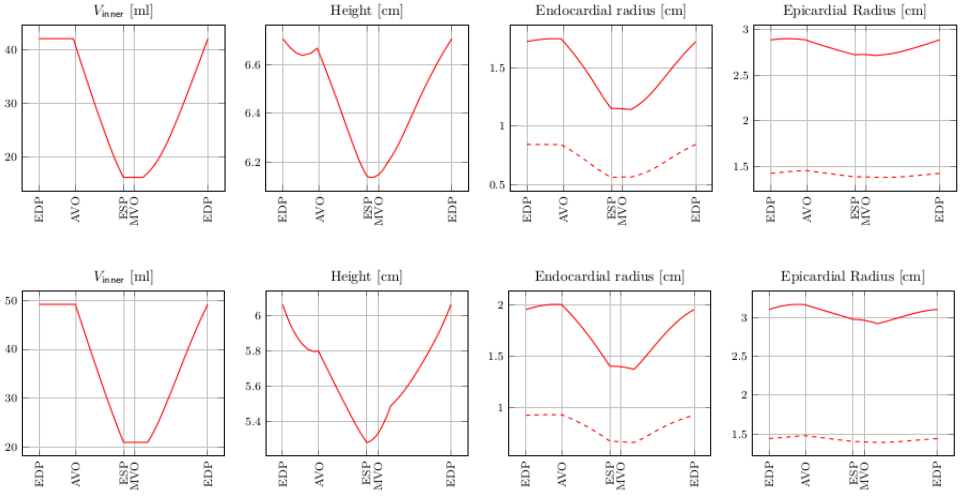

FIGURE 3.10: Plots for inner volume, ventricular height, endocardial and epicardial radius for $n = 3$ (top row) and $n = 9$ (bottom row). In the plots for the radii, the solid and dashed line refer to a basal and an apical section, respectively.

for $n = 3$ to 12,87% for $n = 9$, thus being close to physiological measures.
Correspondingly, higher values for the endocardial radius are registered, together with an improved end-diastolic ventricular volume, as high as 49,18 millimetres for $n = 9$. As a consequence, the efficiency of the ventricle is greatly improved, with a stroke volume of more than 28 millimetres and a significantly higher ejection fraction, about 61% for $n = 3$ and slightly decreasing for higher values of the parameter.
Given the incompressibility of the myocardial tissue, a more relevant ventricular shortening generates an higher wall thickening, both in the basal and apical region; even if the thickening percent does not reach values as high as 50%, as reported in some physiological studies, we can state that this fibre configuration provides a relevant improvement to the microstructural model. Nevertheless, values for torsion was slightly reduced.

In addition, the shortening of fibres due to their activation is higher in the sub-endocardial and sub-epicardial layers, in contrast with the results of the simulation presented in Section 3.2.1; similarly, the greatest strain-energy density is localized near the middle of the myocardial wall.
As a side note, we point out that the relative difference between the ventricular height to radius ratio measured at the end of diastole and at the end of systole was higher than 10% for $n = 9$, and this could undermine the significance of this specific value of n.

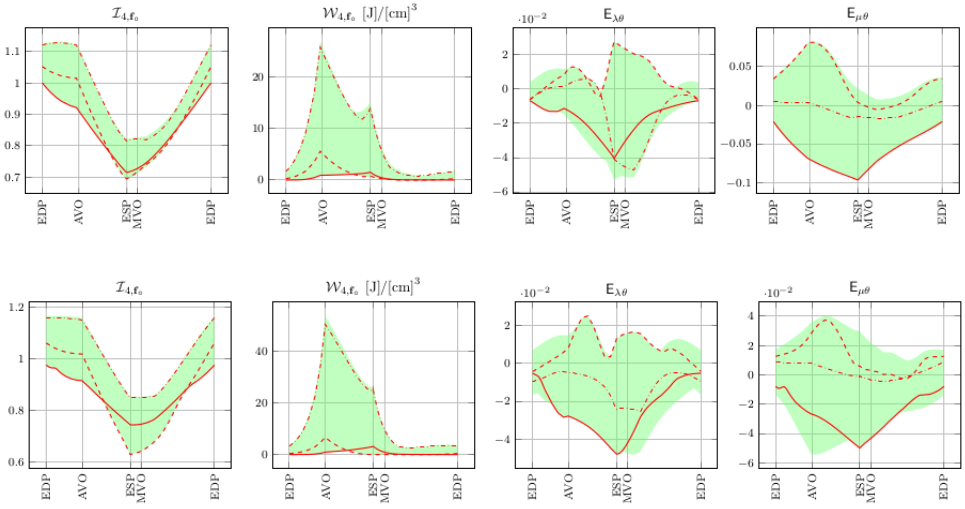

FIGURE 3.11: Plots for the fourth invariant and the corresponding strain-energy, circumferential-radial strain, and circumferential-longitudinal strain for a bimodal fibre distribution with $n = 3$ (top row) and $n = 9$. (bottom row). The lines refer to the sub-epicardium (solid line), sub-endocardium (dashed line), and mid-myocardium (dash-dotted line). The green area represents the range of values spanned in the radial direction. The data are taken in a mid-axis section of the ellipsoid.

3.2.4 Asymmetric bimodal distribution

On the basis of the set of physiological indicators adopted for the analysis of the output of our numerical model, the bimodal distribution of fibre angle yields results that are in good accordance with the physiological evidence. On the other hand, the asymmetry of the distribution of fibres has been reported in several histological researches. In this section, we conjecture a particular fibre distribution that includes both microstructural features.

We consider that the fibre angle configuration defined by:

$$\alpha_{helix}(\lambda_*) = \begin{cases} \frac{1}{\sqrt[n]{0.9}}\ \alpha_{epi}\ (2\lambda_* - 0.9)^{\frac{1}{n}} & 0 \leq \lambda_* \leq 0.45 \\ \frac{1}{\sqrt[n]{1.1}}\ \alpha_{epi}\ (2\lambda_* - 0.9)^{\frac{1}{n}} & 0.45 < \lambda_* \leq 1 \end{cases} \tag{3.4}$$

where, as usual, $\alpha_{epi} = -\alpha_{endo} = \frac{\pi}{3}$ and $n \in \{3, 5, 7, 9\}$. The helix angle is 0 for $\lambda_* = 0.45$, which means that at the middle of the wall fibres have a positive helix angle, and are thus left-handed: this particular feature has a great impact on ventricular mechanics, similarly to the case with a 'quasi-linear' asymmetric distribution of fibres presented in Section 3.2.1. We point out that the derivative of the function $\alpha_{helix}(\lambda_*)$ is not continuous in $\lambda_* = 0.45$, but this fact has no relevant impact on the mechanics, as the fibre field is only evaluated in quadrature nodes.

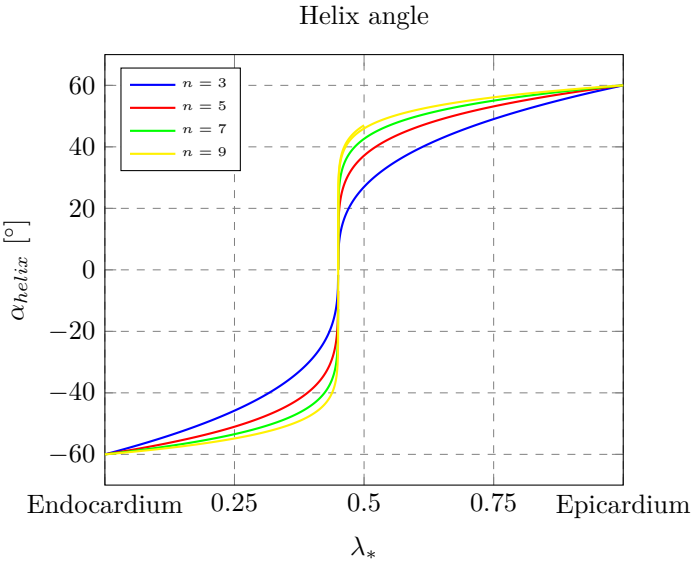

FIGURE 3.12: Transmural variation of helix angle for an asymmetric bimodal fibre distribution for different values of n.

Indicator	$n = 3$	$n = 5$	$n = 7$	$n = 9$
Stroke Volume	24,78 ml	26,25 ml	26,89 ml	26,67 ml
Ejection Fraction	59,51 %	59,11 %	57,24 %	54,66 %
Base Thickening (%)	34,27 %	35,75 %	36,23 %	36,07 %
Apex Thickening (%)	40,81 %	42,64 %	41,91 %	39,50 %
Shortening (%)	9,27 %	10,82 %	12,06 %	13,50 %
Torsion	9,37°	8,51°	8,14°	7,95°

TABLE 3.6: Set of physiological indicators for the simulation with an asymmetric bimodal helix angle configuration.

The asymmetric distribution with a positive helix angle at midwall reduces the efficiency of the ventricle: the values of stroke volume and ejection fraction are lower than the ones obtained in the simulation with a symmetric bimodal fibre orientation, although they remain within the physiological range.

As both the asymmetry and the bimodal configuration improve the ventricular shortening during the diastolic phase, we obtain values higher than in the reference linear configuration, thus improving the accordance with results from physiological studies; the same argument holds for both basal and apical wall thickening. On the other hand, the presence of a bigger portion of left-handed myofibres increases the twist of the ventricle, so that the values for torsion are higher with respect to the case with no asymmetry (Section 3.2.3).

In conclusion, we can state that in the case with $n = 3$ we obtain the best results,

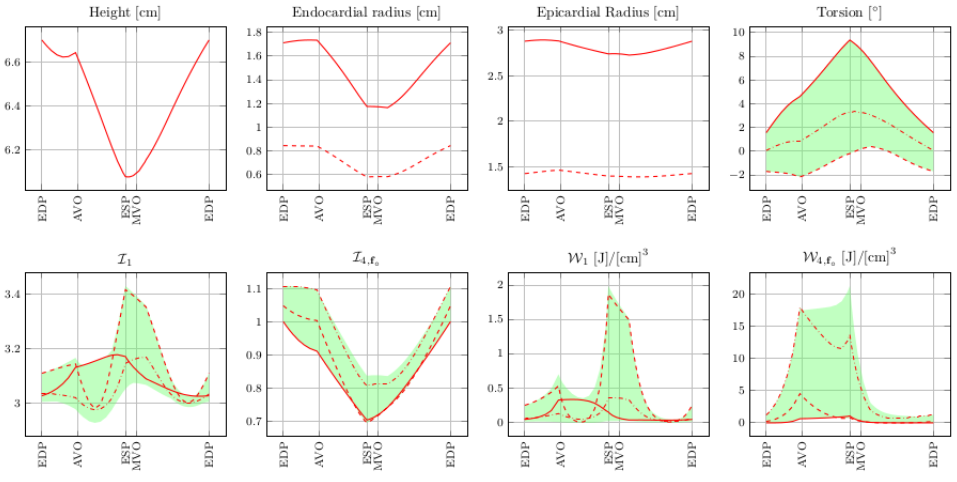

FIGURE 3.13: Plot of ventricular height, endocardial and epicardial radius, torsion, invariants and their corresponding strain-energy during the cardiac cycle for an asymmetric bimodal fibre distribution with $n = 3$. In the plots for the radii, the solid and dashed line refer to a basal and an apical section, respectively. In the case of torsion, invariants and strain-energy, the lines refer to the sub-epicardium (solid line), sub-endocardium (dashed line), and mid-myocardium (dash-dotted line), and the green area represents the range of values spanned in the radial direction.

where most of the considered mechanical indicators take values that fall in the physiological range for healthy hearts. For this value of the parameter, we provide the plots for the most important mechanical quantities obtained in the post-processing step of the numerical simulation (Figures 3.13 and 3.14).

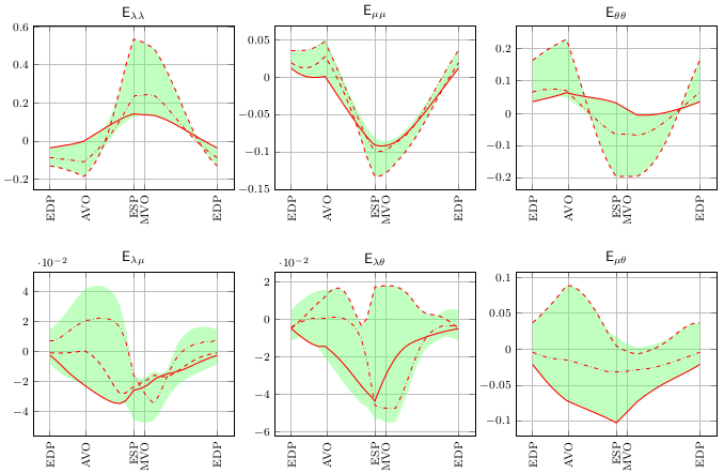

FIGURE 3.14: Plot of Green-Lagrange strain components during the cardiac cycle for an asymmetric bimodal fibre distribution with $n = 3$. The lines refer to the sub-epicardium (solid line), sub-endocardium (dashed line), and mid-myocardium (dash-dotted line). The green area represents the range of values spanned in the radial direction. The data are taken in a mid-axis section of the ellipsoid.

3.3 Transverse angle distribution

If the fibre distribution is completely defined by the helix angle, muscle fibres in the myocardial wall are assumed to be parallel to the endocardial and epicardial surfaces; however, several anatomical researches show that myofibres are wrapped between the sub-endocardial and sub-epicardial layer (Torrent-Guasp 1973, Streeter et al. 1979). In order to provide a complete three-dimensional description of the experimentally observed muscle fibre architecture, we introduce a second angle, the transverse angle α_{trans}: it can be defined as the angle between the local circumferential direction and the projection of the fibre path on the plane perpendicular to the local longitudinal direction (Bovendeerd et al. 1994). The presence of a non-zero transverse angle means that fibres are oriented from the endocardium to the epicardium, and thus the fibre field has a radial component: this microstructural feature can greatly affect the ventricular mechanics, as, in particular, it introduces a mechanical coupling between the sub-endocardial and sub-epicardial layers.
In order to include the presence of the transverse angle into our mechanical model, we re-define the fibre direction as:

$$\mathbf{f}_0 = \cos\alpha_{imb}\ (\lambda_*, \mu)\Big(\cos\ \alpha_{helix}(\lambda_*)\ \mathbf{e}_\theta + \sin\ \alpha_{helix}(\lambda_*)\ \mathbf{e}_\mu\Big) - \sin\alpha_{imb}(\lambda_*, \mu)\ \mathbf{e}_\lambda$$

where α_{imb} denotes the imbrication angle, which is defined by

$$\alpha_{imb}(\lambda_*, \mu) = \arctan\Big(\cos\alpha_{helix}(\lambda_*)\ \tan\alpha_{trans}(\lambda_*, \mu)\Big)\ .$$

An effective visual representation of transverse and imbrication angles has already been provided in Chapter 1 (Figures 1.6 and 1.7). Histological studies show that the transverse angle is positive in the basal half and negative in the apical half of the ventricle (Torrent-Guasp 1973). According to Streeter and co-workers (1979), the value of α_{trans} averaged across the wall thickness was found to be $-4,6 \pm 0.8°$ in the apical region and $-3,5 \pm 0.6°$ halfway between equator and apex; later, a simplified model was proposed, with a transverse angle equal to $+3°$ in the basal half and $-3°$ in the apical half. In our work, we follow the approach proposed by Bovendeerd and co-workers (1994): the transmural variaton of α_{trans} is supposed to be quadratic, with a maximum at the middle of the myocardial wall. The transverse angle is null on the whole equatorial plane (identified by $\mu = \frac{\pi}{2}$), it is positive for $\mu > \frac{\pi}{2}$, which denotes the basal region, and negative for $\mu < \frac{\pi}{2}$, which means in the proximity of the apex. Additionally, the transverse angle is zero at the endocardial and the epicardial surfaces, since muscle fibres are not supposed to end at these surfaces. Thus, the transverse fibre angle must depend both on λ_* and

on μ, and its explicit expression reads:

$$\alpha_{trans}(\lambda_*, \mu) = \begin{cases} 4\ \alpha_{t,apex}(\lambda_* - \lambda_*^2)\ (\frac{2\mu}{\pi} - 1)^2 & \mu \leq \frac{\pi}{2} \\ 36\ \alpha_{t,base}(\lambda_* - \lambda_*^2)\ (\frac{2\mu}{\pi} - 1)^2 & \mu > \frac{\pi}{2} \end{cases} \tag{3.5}$$

where $\alpha_{t,apex}$ and $\alpha_{t,base}$ denote the value of the basal and apical transverse angle at midwall, respectively.

In this section, we will consider the simplest configuration for the helix angle, characterized by a linear variation of α_{helix} from $-60°$ at the endocardium to $60°$ at the epicardium, which is the same helix angle distribution used in Section 3.1; in addition, the transversely isotropic model is used. A complete model including a more complex helix angle distribution will be discussed in Section 3.3.3.

3.3.1 Symmetric transverse angle

In this section, we consider a symmetric transverse angle distribution, which means that $\alpha_{t,base} = -\alpha_{t,apex}$ and $\alpha_{trans}(\lambda_*, \frac{\pi}{2}) = 0$. However, defining this distribution as symmetric may seem inappropriate for a prolate ellipsoid, because the apex and the base are located at a different distance from the equator: in fact, there is no real geometrical symmetry.

We consider four different values for $\alpha_{t,base}$, ranging from $4,5°$ to $18°$. Figure 3.15 provides a visual representation of the transverse angle variation, both between the endocardial and epicardial surfaces, and between the apical and basal regions. In particular, the plot on the right provides a plot of the value of the transverse angle at the middle of the myocardial wall, for each different value of $\alpha_{t,base}$.

The introduction of a non-zero transverse angle yields a slightly increased stroke volume with respect to the simulation discussed in Section 3.1; although, no relevant changes in stroke volume are registered for different values of the parameter. On the other hand, ejection fraction increases for an higher transverse angle, up to 61,30% for $\alpha_{t,base} = 18°$.

Indicator	$\alpha_{t,base} = 4,5°$	$\alpha_{t,base} = 9°$	$\alpha_{t,base} = 13,5°$	$\alpha_{t,base} = 18°$
Stroke Volume	24,00 ml	24,17 ml	24,18 ml	24,07 ml
Ejection Fraction	59,16 %	60,31 %	61,05 %	61,30 %
Base Thickening	31,02 %	31,96 %	32,90 %	33,19 %
Apex Thickening	32,39 %	31,77 %	30,94 %	29,90 %
Shortening	4,65 %	4,68 %	4,78 %	4,95 %
Torsion	10,44°	10,10°	9,41°	8,51°

TABLE 3.7: Set of physiological indicators for different values of $\alpha_{t,base}$.

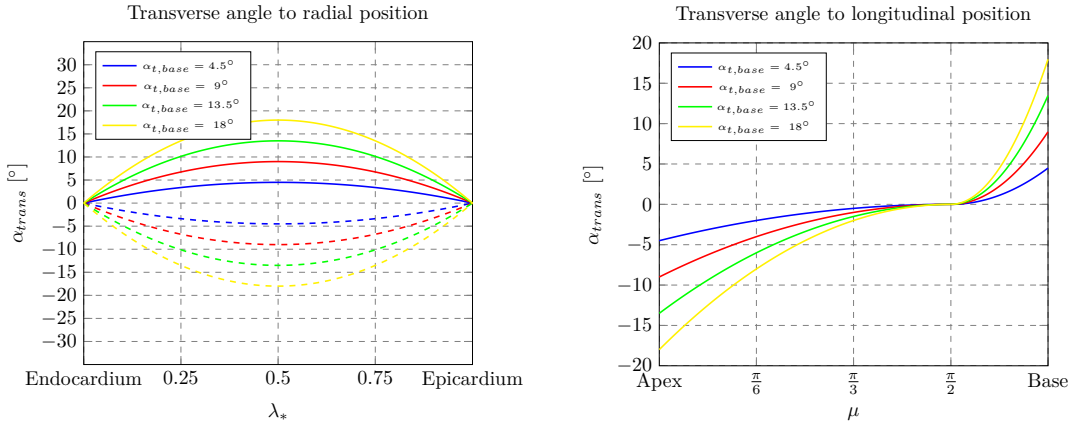

FIGURE 3.15: Transmural (left) and longitudinal (right) transverse angle distribution for different values of $\alpha_{t,base}$. In the plot on the left, the solid lines refer to the base, while the dashed lines refer to the apical transverse angle. The plot on the right reports the transverse angle at midwall.

In addition, for increasing values of $\alpha_{t,base}$, we find that the wall thickening is increasing in the basal region while decreasing in apical region: this behaviour is the result of change of the transverse angle in the longitudinal direction, and provides a proof of the influence of the imbrication of fibres on the thickening of the myocardial wall during the cardiac cycle. Nevertheless, another notable effect is the reduction of ventricular torsion for higher values of the transverse angle.

In contrast with the findings of Bovendeerd and co-workers (1994) as a results of their

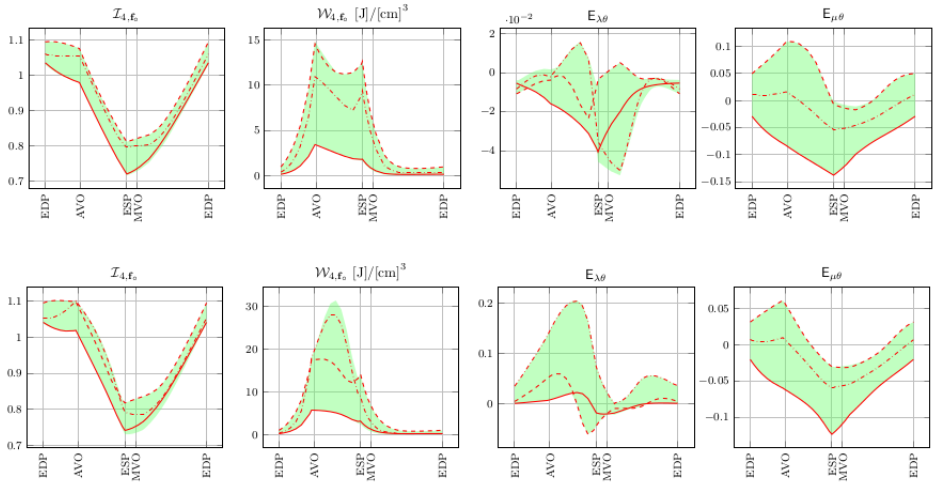

FIGURE 3.16: Plots for the fourth invariant and the corresponding strain-energy, circumferential-radial strain, and circumferential-longitudinal strain for a fibre distribution with transverse angle $\alpha_{t,base} = 4,5°$ (top row) and $\alpha_{t,base} = 18°$ (bottom row). The lines refer to the sub-epicardium (solid line), sub-endocardium (dashed line), and mid-myocardium (dash-dotted line). The green area represents the range of values spanned in the radial direction. The data are taken in a mid-axis section of the ellipsoid.

numerical methods, no significant changes in basal wall thickness and in basal ventricular diameter are registered. Bovendeerd assumed that the circumferential lengthening was due to the fact that muscle fibres, which provide a greater stiffness along their direction, are no longer circumferentially oriented.

The most evident effect of the introduction of a transverse fibre angle is the reduction of the transmural difference in the angle of rotation, both in the apical and in the basal regions (Figure 3.17). As a matter of fact, for $\alpha_{t,base} = 18°$ we obtain a small difference in end-systolic rotation between the endocardium and the epicardium: this behaviour is confirmed by physiological studies that report a transmural difference of around 0° at

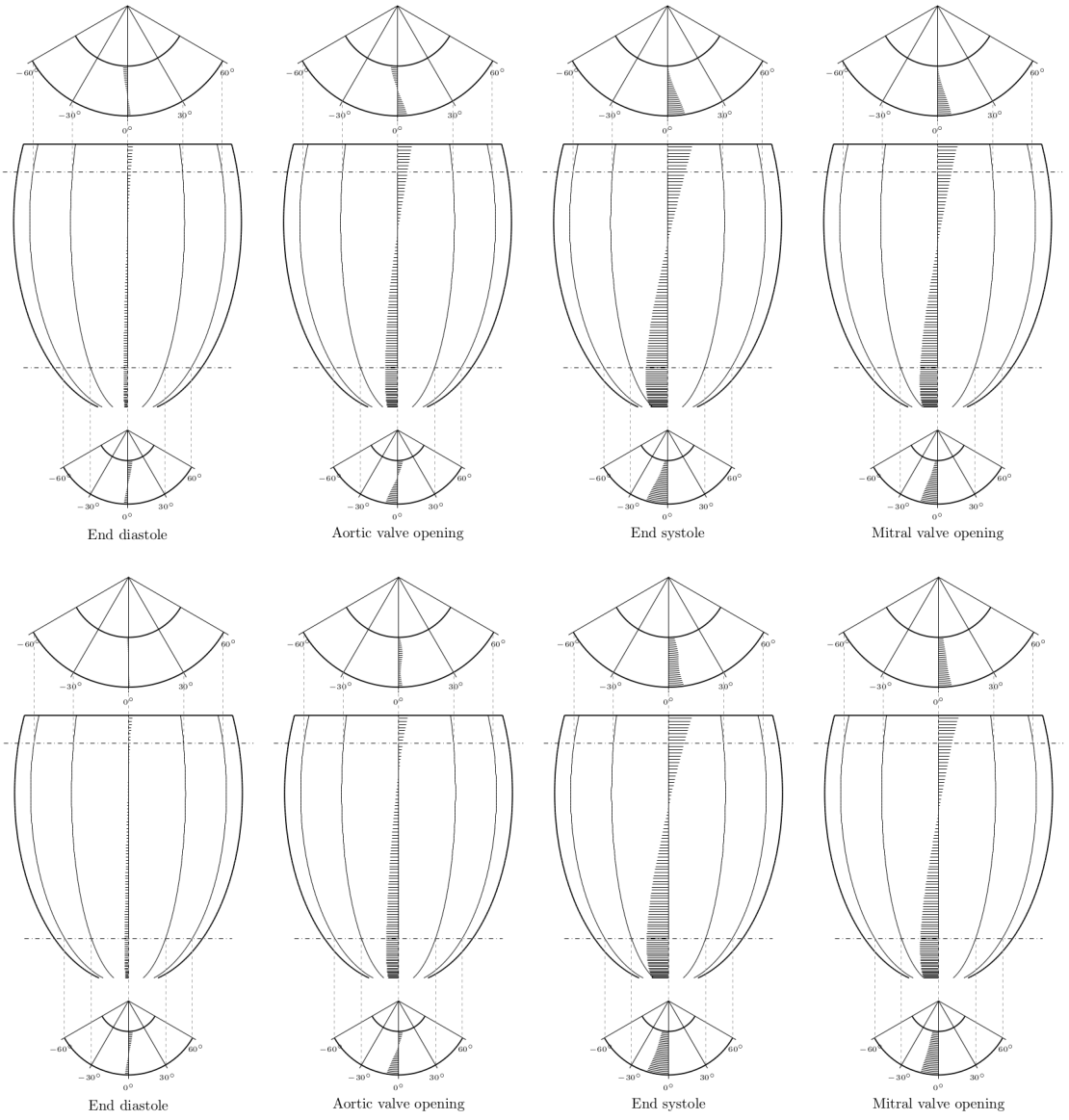

FIGURE 3.17: Ventricular torsion in four different phases of the cardiac cycle for $\alpha_{t,base} = 4,5°$ (top) and $\alpha_{t,base} = 18°$ (bottom). For each case, top and bottom figures represent the in-plane transversal rotation in a basal and apical section, while the figures in the middle strip refers to the epicardial rotation.

the base and 8° at the apex (Buchalter et al. 1990); thus, we can state that a non-zero transverse angle can provide realistic results in this regard. Nevertheless, other researches reported an higher endocardial rotation with respect to the epicardial one (Young et al. 2012), but this fact is not confirmed by our numerical implementation of the model.
We point out that the presence of a transverse angle means that the orientation of myofibres induces a stronger mechanical coupling between the sub-endocardial and sub-epicardial layers beyond the merely isotropic one due to the first invariant. Since muscle fibres are stiffer than the passive myocardial tissue, transmural shear deformation is strongly reduced when myofibres are oriented in a direction that has a non-zero transverse component: as we can see from Figure 3.16, in the simulations performed the modulus of the end-systolic value of the circumferential-radial strain $E_{\lambda\theta}$ at the epicardium decreases from about 0.04 for $\alpha_{t,base} = 4,5°$ to less than 0.01 for $\alpha_{t,base} = 18°$. In conclusion, a fibre configuration with a non-zero transverse angle causes a reduced shear deformation, which reflects a reduced shear loading of the passive tissue.

3.3.2 Asymmetric transverse angle

In the previous section, we have analysed the numerical results obtained using a fibre orientation characterized by the same transverse angle both at the apex and at the base. However, in several numerical studies (such as Bovendeerd et al. 2009) a non-symmetric angle distribution in the longitudinal direction was considered: in particular, the fibrous structure has a higher apical transverse angle. This assumption can be easily understood from the geometrical point of view: the transverse angle is zero in the equatorial plane, and increases with the distance from it; as a consequence, it should take different values at the apex and at the base, based on their distance from the equator. Nevertheless, there is no confirmation for this fact based on physiological studies, as the fibre field in the proximity of the apical region has a complex orientation.

As a side note, we point out that Bovendeerd and co-workers considered and high transverse angle at the apex, close to $-50°$. Our model and its corresponding implementation exhibits some numerical problems with high transverse angles, yielding high stress peaks at the end of systole and other non-physiological behaviours. As a consequence, we only study the mechanical impact of a transverse angle configuration based on the usual formula (3.5) with an apical angle of $-18°$ or $-27°$ while keeping $\alpha_{t,base}$ fixed at $13,5°$, and we compare the results with a symmetric simulation with a transverse angle configuration with parameters $\alpha_{t,apex} = -13,5°$ and $\alpha_{t,base} = 13,5°$ (Figure 3.18).

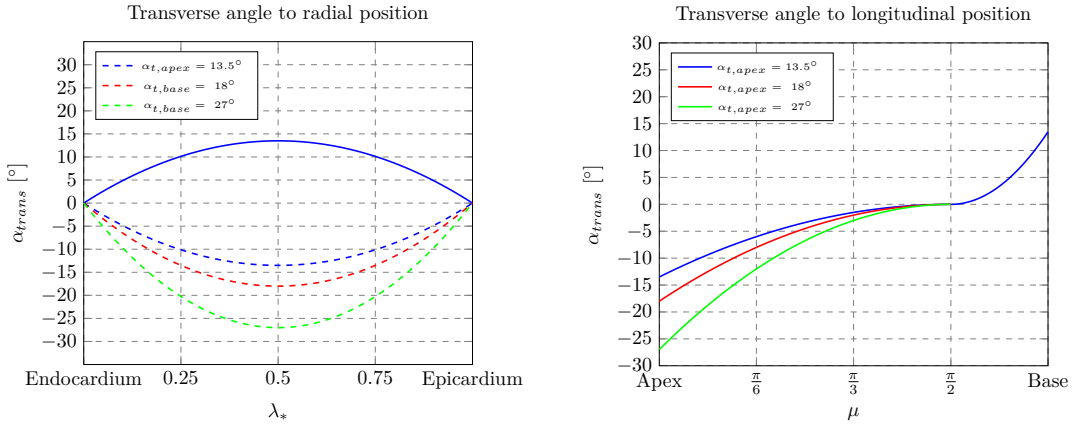

FIGURE 3.18: Transmural (left) and longitudinal (right) transverse angle asymmetric distribution for different values of $\alpha_{t,apex}$. In the plot on the left, the solid lines refer to the base, while the dashed lines refer to the apical transverse angle. The plot on the right reports the transverse angle at midwall.

Indicator	$\alpha_{t,apex} = -13,5°$	$\alpha_{t,apex} = -18°$	$\alpha_{t,apex} = -27°$
Stroke Volume	24,18 ml	24,25 ml	24,31 ml
Ejection Fraction	61,05 %	61,49 %	62,15 %
Base Thickening	32,90 %	33,10 %	33,70 %
Apex Thickening	30,94 %	29,51 %	26,81 %
Shortening	4,78 %	4,99 %	5,91
Torsion	9,41°	9,17°	8,47°

TABLE 3.8: Set of physiological indicators for different values of $\alpha_{t,apex}$ and fixed $\alpha_{t,base}$.

Regarding the physiological indicators, only a slight increase in the ventricular efficiency is registered, with higher stroke volume and ejection fraction for higher apical transverse angles. However, a notable effect is the decrease of the wall thickening in the proximity of the apex, caused by the negative transverse angle: in the case $\alpha_{t,apex} = -27°$, the apical thickening is reduced to 26,81%.

Even if we report higher values for ventricular shortening during the cardiac cycle, torsion is greatly reduced for a high apical transverse angle, reaching values below the physiological twitch for healthy hearts. Additionally, no significant differences are found in the distribution of strain and stress in the myocardial wall during the cardiac activity.

The most relevant effect resulting from a higher apical transverse angle is the reduced transmural shear in the apical region: as a matter of fact, we register an higher endocardial rotation with respect to the epicardial one at the end of systole for $\alpha_{t,apex} = -27°$, while the basal rotation is similar (Figure 3.19): from this point of view, this particular transverse angle configuration fits the physiological results (Buchalter et al. 1990).

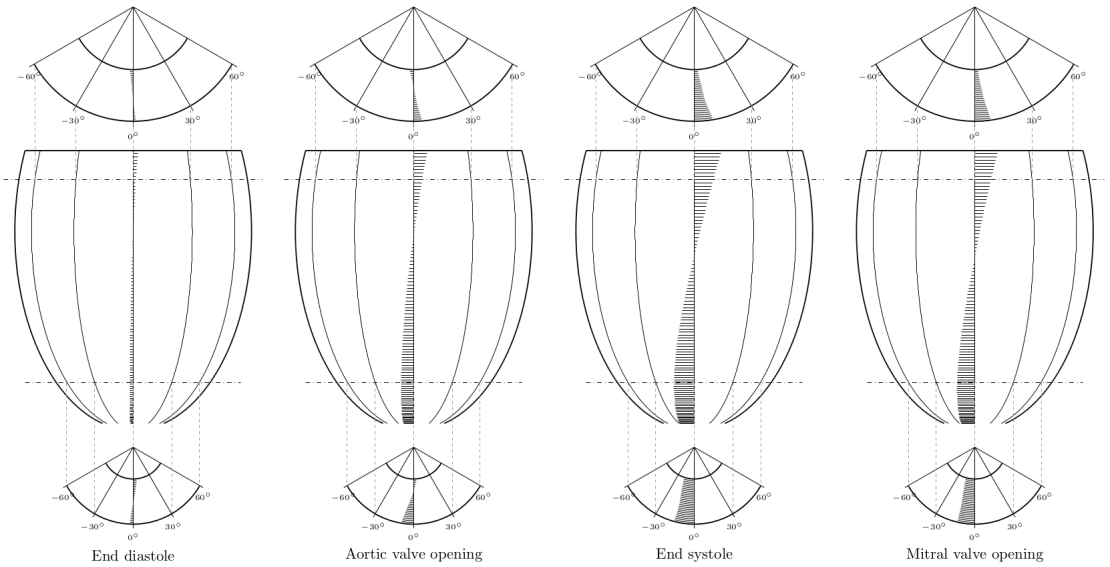

FIGURE 3.19: Ventricular torsion in four different phases of the cardiac cycle for $\alpha_{t,apex} = -27°$. Top and bottom figures represent the in-plane transversal rotation in a basal and apical section, while the figures in the middle strip refers to the epicardial rotation.

3.3.3 Complete fibre architecture

In this section, we consider a complete model for the fibrous microstructure, taking into account the mechanical impact of the variation of helix angle inside the myocardial wall and the influence of the transverse angle on the most important physiological quantities computed during the cardiac cycle. Our choice is to use the bimodal asymmetric distribution for the helix angle and a symmetric transverse angle configuration; as above, we consider the transversely isotropic version of the Holzapfel-Ogden model.
In summary, the tissue microstructure is determined by the fibre orientation $\mathbf{f}_0$, which is defined by

$$\mathbf{f}_0 = \cos\alpha_{imb}(\lambda_*,\mu)\,\Big(\cos\ \alpha_{helix}(\lambda_*)\ \mathbf{e}_\theta + \sin\ \alpha_{helix}(\lambda_*)\ \mathbf{e}_\mu\Big) - \sin\alpha_{imb}(\lambda_*,\mu)\ \mathbf{e}_\lambda\ ,$$

where the imbrication angle α_{imb} is defined by:

$$\alpha_{imb}(\lambda_*,\mu) = \arctan\Big(\cos\alpha_{helix}(\lambda_*)\ \tan\alpha_{trans}(\lambda_*,\mu)\Big)\ .$$

Additionally, we define the helix and transverse angle by

$$\alpha_{helix}(\lambda_*) = \begin{cases} \frac{1}{\sqrt[3]{0.9}}\ \alpha_{epi}\ (2\lambda_* - 0.9)^{\frac{1}{3}} & 0 \le \lambda_* \le 0.45 \\ \frac{1}{\sqrt[3]{1.1}}\ \alpha_{epi}\ (2\lambda_* - 0.9)^{\frac{1}{3}} & 0.45 < \lambda_* \le 1 \end{cases} ,$$

$$\alpha_{trans}(\lambda_*, \mu) = \begin{cases} 4\ \alpha_{t,apex}(\lambda_* - \lambda_*^2)\ (\frac{2\mu}{\pi} - 1)^2 & \mu \le \frac{\pi}{2} \\ 36\ \alpha_{t,base}(\lambda_* - \lambda_*^2)\ (\frac{2\mu}{\pi} - 1)^2 & \mu > \frac{\pi}{2} \end{cases} ,$$

respectively; the choice for modelling parameters, expressed in degrees, is

$$\alpha_{epi} = 60^\circ\ , \quad \alpha_{t,apex} = -13,5^\circ\ , \quad \alpha_{t,base} = +13,5^\circ\ .$$

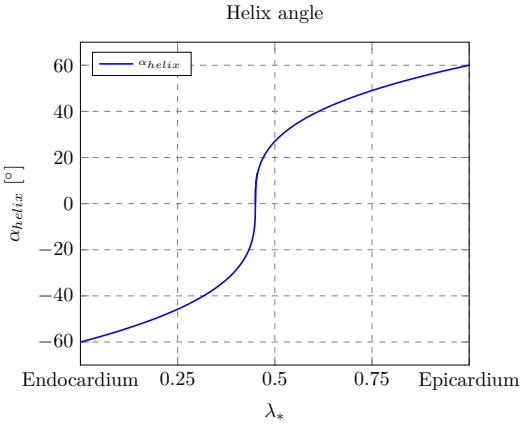

FIGURE 3.20: Helix angle for the complete fibre architecture.

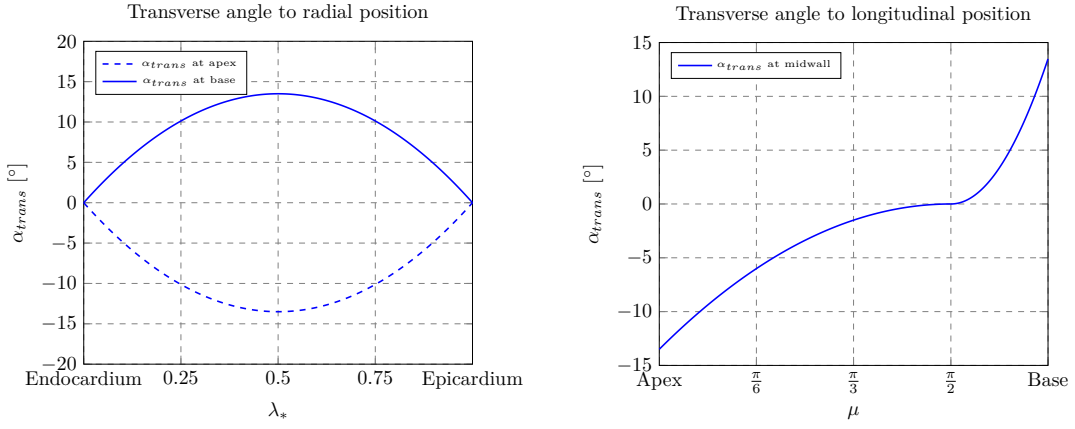

FIGURE 3.21: Transmural (left) and longitudinal (right) transverse angle asymmetric distribution the complete fibre architecture. In the plot on the left, the solid line refers to the base, while the dashed line refers to the apical transverse angle. The plot on the right reports the transverse angle at midwall.

Indicator	Value
Stroke Volume	24,92 ml
Ejection Fraction	61,87 %
Thickening Base	33,50 %
Thickening Apex	40,63 %
Shortening	9,16 %
Height/Radius Ratio EDP	2,32 %
Height/Radius Ratio ESP	2,21 %
Torsion	7,88°

TABLE 3.9: Set of physiological indicators for the complete fibrous structure with an asymmetric bimodal distribution of helix angle and a symmetric transverse angle.

The plots in Figure 3.20 and Figure 3.21 provide an effective visual representation of the spatial variation of fibre angles.

We resume the main improvements to the ventricular mechanics provided by this particular myofibre configuration, comparing the results obtained from the post-processing step with the ones from the transversely isotropic simulation presented in Section 3.1, which featured a simple linear helix angle configuration and zero transverse angle:

- the ventricular efficiency is notably higher, as the current fibre configuration provided a 4% increase in ejection fraction;

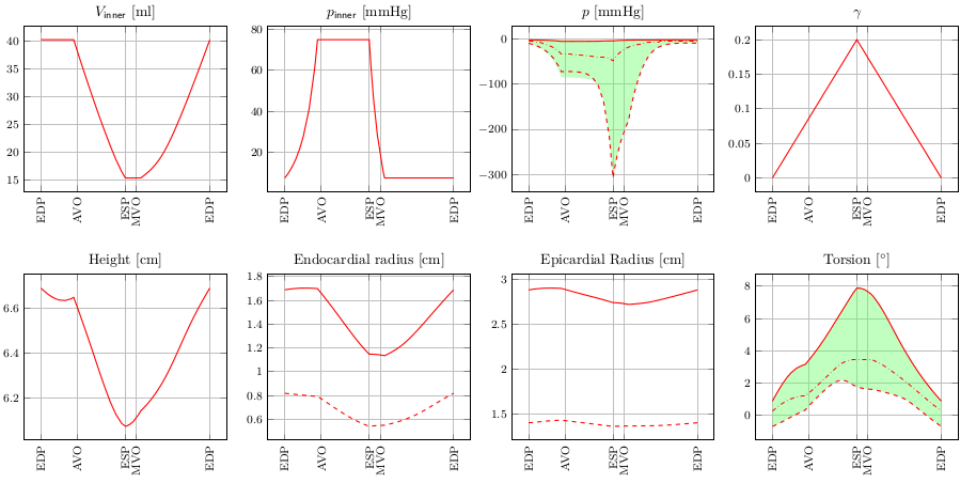

FIGURE 3.22: Plot of ventricular volume, pressure, activation parameter, ventricular height, endocardial and epicardial radius, and torsion during the cardiac cycle for a complete fibre architecture. In the plots for the radii, the solid and dashed line refer to a basal and an apical section, respectively. In the case of pressure and torsion, the lines refer to the sub-epicardium (solid line), sub-endocardium (dashed line), and mid-myocardium (dash-dotted line), and the green area represents the range of values spanned in the radial direction.

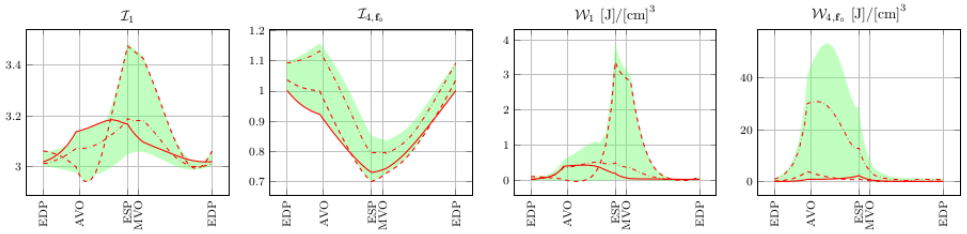

FIGURE 3.23: Plot of invariants and their corresponding strain-energy density during the cardiac cycle for a complete fibrous structure. The lines refer to the sub-epicardium (solid line), sub-endocardium (dashed line), and mid-myocardium (dash-dotted line). The green area represents the range of values spanned in the radial direction. The data are taken in a mid-axis section of the ellipsoid.

- the wall thickening during the cardiac cycle is closer to the value registered from healthy hearts; in particular, the higher apical thickening can be confirmed;
- ventricular shortening at the end of the systolic phase is greatly increased, but it does not reach the value reported in physiological researches, which is close to 20%;
- as a negative note, the reduced torsion is mainly due to the transverse angle of fibres: from this point of view, we do not register a significative increment in physiological quantities resulting from the introduction of the imbrication angle;
- the correct physiological behaviour of the ventricle during the isochoric contraction phase is an important achievement: in fact, in this phase we registered a slight shortening of the ventricle, consistently with physiological data; in contrast, we recall that in the numerical simulations characterized by a linear variation of the

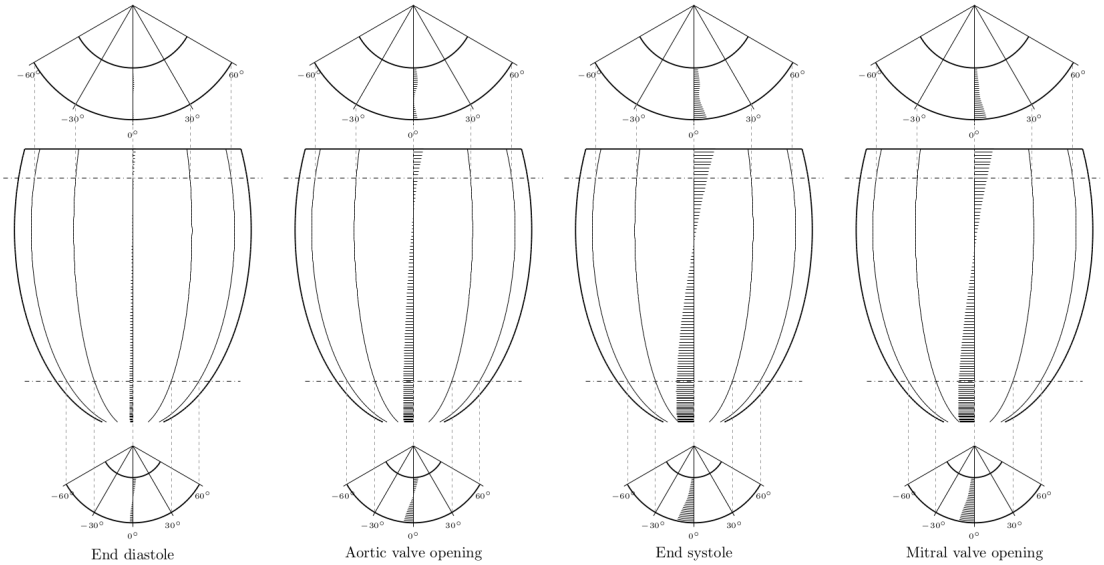

FIGURE 3.24: Ventricular torsion in four different phases of the cardiac cycle for a complete fibrous structure. Top and bottom figures represent the in-plane transversal rotation in a basal and apical section, while the figures in the middle strip refers to the epicardial rotation.

helix angle we reported a non-physiological increment in ventricular height during this cardiac phase;

- the introduction of a non-zero transverse angle induces lower values for circumferential-radial shear at the end of systole, and similar endocardial and epicardial rotations both in the basal and apical regions.

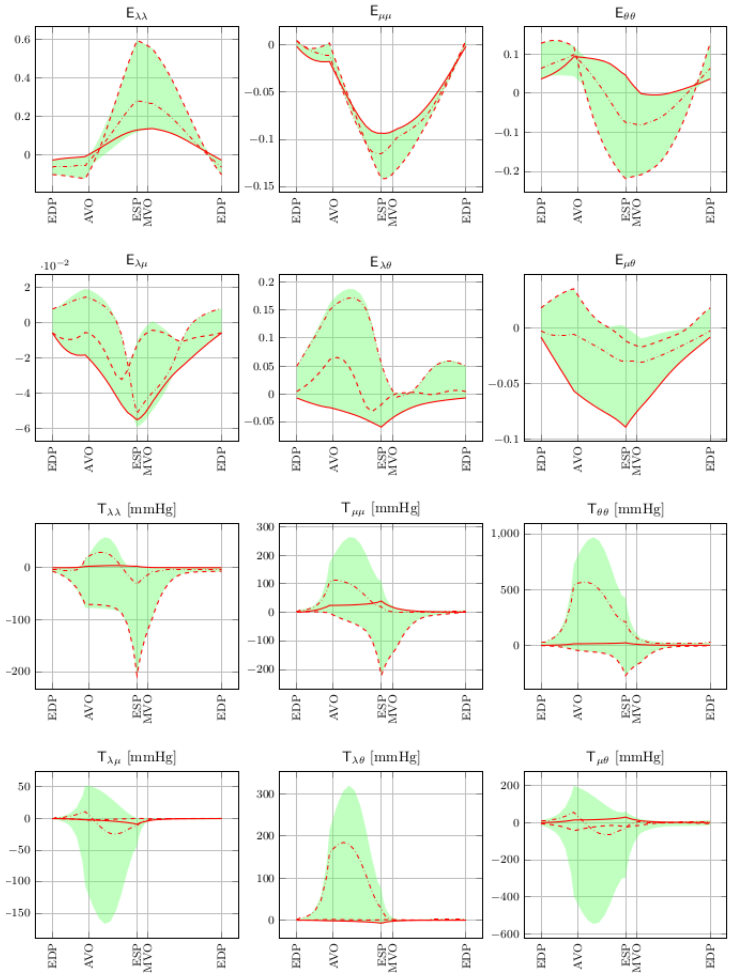

FIGURE 3.25: Plot of Green-Lagrange strain (first two rows) and Cauchy stress (last two rows) components during the cardiac cycle for a complete fibrous structure. The lines refer to the sub-epicardium (solid line), sub-endocardium (dashed line), and mid-myocardium (dash-dotted line). The green area represents the range of values spanned in the radial direction. The data are taken in a mid-axis section of the ellipsoid.

3.4 Laminar structure

Physiological studies on the myocardial muscle reveal that myocytes are organized in laminar sheets, which are approximately four cells thick and stacked from apex to base; the coupling between myocytes in the same laminar structure is provided by a network of extracellular collagen fibres. However, the mechanical function of the myocardial laminar architecture is still not well understood: LeGrice and co-workers (1995) conjectured that the sheet structure allows rearrangement of myofibre bundles by sliding along cleavage planes during the cardiac cycle, improving systolic wall thickening; as a matter of fact, the increase in diameter of the sarcomeres cannot be fully responsible of the myocardial thickening physiologically observed (Costa et al. 1999).
In the numerical modelling of the cardiac mechanics, several different sheet configurations have been used: radial sheets, a linear change of sheet angle from the endocardium to the epicardium but with no differences from apex to base, or different apical and basal configurations. Nevertheless, the low sensitivity of the most important physiological parameters to changes in the laminar structure has been reported (Pezzuto et al. 2014). As a matter of fact, the numerical results resumed in Section 3.1 prove that the removal of energetic terms associated to the sheet architecture results in no substantial differences in terms of the most important physiological parameters of the cardiac activity.
Given the minor relevance of the laminar structure in the cardiac mechanics, we consider the orthotropic version of the Holzapfel-Ogden model with a simple sheet configuration, characterized by a sheet angle β that spans the $(-80°; 80°)$ interval and changes linearly from the endocardium to the epicardium. Thus, the sheet orientation is defined by:

$$\begin{aligned}
&\mathbf{s}_0 = \sin\beta(\lambda_*)\,\Big(\sin\alpha_{helix}(\lambda_*)\;\mathbf{e}_\theta - \cos\alpha_{helix}(\lambda_*)\;\mathbf{e}_\mu\Big) + \cos\beta(\lambda_*)\;\mathbf{e}_\lambda\;,\\
&\beta(\lambda_*) = \beta_{endo}\;(1-\lambda_*) + \beta_{epi}\;\lambda_*\;,
\end{aligned}$$

where $\beta_{endo} = -\frac{4}{9}\pi$ and $\beta_{epi} = \frac{4}{9}\pi$. For the sake of simplicity, we consider a linear configuration of fibre angle in the cardiac wall, and we directly compare the results with the output of the simulation performed in Section 2.7, characterized by a radial distribution of sheets, which corresponds to the choice $\beta_{endo} = \beta_{epi} = 0$.

Indicator	Radial sheets	Linear sheets
Stroke Volume	22,57 ml	23,04 ml
Ejection Fraction	55,97 %	57,53 %
Thickening Base	27,91 %	29,58 %
Thickening Apex	31,17 %	31,90 %
Shortening	3,79 %	4,12 %
Torsion	10,03°	10,33°

TABLE 3.10: Set of physiological indicators for the radial and linear sheet architecture.

Based on our results, we can confirm that a different laminar structure has almost no effect on the most important physiological quantities: the ventricular efficiency seems to be slightly increased by a linear distribution of sheets; as a matter of fact, the radial sheet structure is only a rough approximation of the laminar architecture.

Naturally, the main differences between the two configurations can be found in the spa-

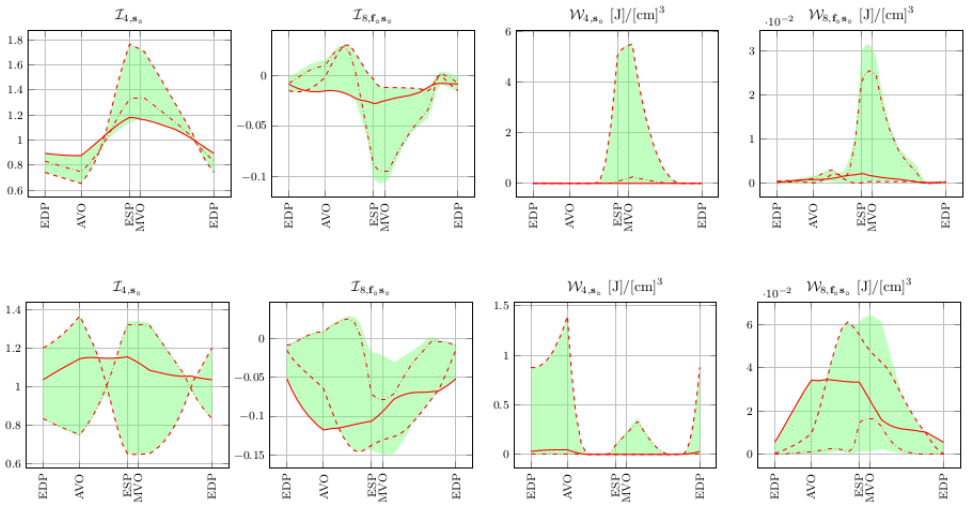

FIGURE 3.26: Plots for the fourth and eight invariant and the corresponding strain-energy for a radial (top row) and linear sheet architecture (bottom row). The lines refer to the sub-epicardium (solid line), sub-endocardium (dashed line), and mid-myocardium (dash-dotted line). The green area represents the range of values spanned in the radial direction. The data are taken in a mid-axis section of the ellipsoid.

tial and temporal trend of invariants associated to the sheet orientation, $\mathcal{I}_{4,\mathbf{s}_0}$ and $\mathcal{I}_{8,\mathbf{f}_0\mathbf{s}_0}$, and the corresponding strain-energy density (Figure 3.26). The value for the invariants at the middle of the ventricular wall does not seem to experience a noticeable change, as in both cases $\beta = 0$ for $\lambda_* = \frac{1}{2}$. On the other hand, in the linear case sheets at the endocardium seem to be under traction ($\mathcal{I}_{4,\mathbf{s}_0} > 1$) during the isochoric contraction and early systole, thus contributing to the elastic energy, as clearly shown by the plot for $\mathcal{W}_{4,\mathbf{s}_0}$. Similarly, $\mathcal{I}_{8,\mathbf{f}_0\mathbf{s}_0}$ took higher values and provided an higher contribution to the strain-energy density; nevertheless, we point out that this contribution is two orders of

magnitude smaller with respect to the one provided by $\mathcal{I}_1$ and $\mathcal{I}_{4,\mathbf{s}_0}$.
Except for higher values for the circumferential-radial and longitudinal-radial Green-Lagrange strain components, no other significant differences are registered in the mechanical status of the ventricle during the cardiac cycle.
In addition, we numerically tested several different sheet configurations, keeping the endocardial and epicardial angles fixed; however, almost no differences were found in the distribution of strain and stress during the cardiac cycle, apart from minor changes in the value of $\mathcal{I}_{4,\mathbf{s}_0}$ and its corresponding strain energy inside the ventricular wall at the end of the systolic phase. In conclusion, based on our numerical model, we can confirm the low impact of the laminar structure on the ventricular mechanics.

CHAPTER 4

THE ROLE OF THE SECOND STRAIN INVARIANT AND BOUNDARY CONDITIONS

Introduction

The purpose of this chapter is to provide some minor modifications to the numerical model for ventricular mechanics presented in this work, from both the mechanical and mathematical point of view.
The first section focuses on the introduction of the second strain invariant, which is usually neglected in the Holzapfel-Ogden model: we provide some minor modifications to the model in order to analyse the mechanical impact of this invariant, and we discuss the results on the basis of some numerical simulations.
Next, we take a closer look to the boundary conditions and we discuss their introduction in the variational formulation for the pressure-volume loop. Moreover, we will consider a different kind of conditions in order to provide a better modelling for the physiological boundaries of the left ventricle.

4.1 The importance of the second strain invariant

The constitutive modelling of the mechanical response for isotropic, incompressible, hyperelastic materials is based on a strain energy density function that depends on the first two principal invariants of the strain tensor. The mechanical theory for rubber-like materials is often based on the neo-Hookean model, characterized by a strain energy that linearly depends on the first strain invariant; a classical modification for this model leads to the Mooney-Rivlin law, which includes an additive term, linear in the second

invariant. Even if these two classical models provide an accurate prediction for the mechanical response at small ranges of stretch, they fail to reproduce the strain-stiffening effect that is experimentally observed at larger values of stretch: in order to reproduce the correct phenomenological behaviour, several different strain-stiffening models have been proposed in the literature (Knowles et al. 1977, Ogden et al. 1997). Nevertheless, in the particular case of soft biomaterials, models with an exponential dependence on the strain invariants play a key role in the reproduction of the mechanical response of the material. As a matter of fact, in soft tissues the strain-stiffening effect arises at smaller values of stretch, when compared to rubber-like materials (Horgan et al. 2012).
In general, the inclusion of a dependence on the second strain invariant of the strain-energy function for an hyperelastic material provides a better modelling for the mechanical response of the material; on the other hand, models that do not consider this invariant fail to capture some significant physical effects (Wineman et al. 2005). In Section 4.1.1, in order to investigate the relevance of the second invariant, we analyze two simple constitutive models for incompressible isotropic elastic materials, and we examine the stress response for two simple homogeneous deformation in order to point out the effects of the inclusion of the second invariant. In Section 4.1.2, we propose a modified Holzapfel-Ogden model which takes into account the energetic contribution associated to the second invariant, which is usually neglected; consequently, in Section 4.1.3 we discuss the results of some numerical simulation based on the implementation of the modified model previously introduced, in order to evaluate the impact of the second invariant on ventricular mechanics.

4.1.1 The isotropic case

In order to fully understand the effect of the introduction of the second invariant, we describe two simple consistitutive models for incompressible isotropic elastic material and we analyse the predicted response for two basic homogeneous deformations (Wineman et al. 2005). First, we recall the first three invariants, which are scalar function of the right Cauchy-Green strain tensor:

$$\begin{aligned}\mathcal{I}_1(\mathsf{C}) &= \mathrm{tr}\mathsf{C}\ ,\\ \mathcal{I}_2(\mathsf{C}) &= \frac{1}{2}\Big[(\mathrm{tr}\mathsf{C})^2 - \mathrm{tr}\mathsf{C}^2\Big]\ ,\\ \mathcal{I}_3(\mathsf{C}) &= \det\mathsf{C}\ .\end{aligned}$$

The strain energy density function for an incompressible isotropic elastic material is $\mathcal{W} = \mathcal{W}(\mathcal{I}_1, \mathcal{I}_2)$, as $\mathcal{I}_3 = 1$ follows from the incompressibility. In the case of soft biomaterials, a common choice that takes into account the strain-stiffening effect is the *Fung-Demiray*

model:

$$\mathcal{W}^{FD}(\mathcal{I}_1) = \frac{a}{2b}\left[e^{b(\mathcal{I}_1-3)} - 1\right] , \tag{4.1}$$

which involves two constitutive parameters, the shear modulus a and the adimensional constant b which provides a measure of the strain-stiffening (Fung 1967, Demiray 1972). This model belongs to the class of generalized neo-Hookean materials, as the strain energy $\mathcal{W}^{FD}$ only depends on the first strain invariant. In the limit as $b \to 0$, the *Neo-Hookean model* is recovered:

$$\mathcal{W}^{NH}(\mathcal{I}_1) = \frac{a}{2}\,(\mathcal{I}_1 - 3) .$$

A generalization of the Fung-Demiray model that includes a dependence on the second invariant is the *Vito model*:

$$\mathcal{W}^{V}(\mathcal{I}_1, \mathcal{I}_2) = \frac{a}{2b}\left[e^{b[\delta(\mathcal{I}_1-3)+(1-\delta)(\mathcal{I}_2-3)]} - 1\right] , \tag{4.2}$$

which is based on the parameter $\delta \in [0, 1]$: for $\delta = 1$, the Fung-Demiray model (4.1) is recovered. In the limit as $b \to 0$, one obtains:

$$\mathcal{W}^{MR}(\mathcal{I}_1, \mathcal{I}_2) = \frac{a}{2}\left[\delta(\mathcal{I}_1 - 3) + (1-\delta)(\mathcal{I}_2 - 3)\right] ,$$

which is the so-called *Moonley-Rivlin model*. In the literature, the Vito model has received little attention when compared to the Fung-Demiray model, but the inclusion of the second invariant allows the reproduction of important mechanical features of soft biomaterials. In the following, we analyse the stress response of the Fung-Demiray and Vito models for two simple homogeneous deformations in order to examine the effects of the inclusion of the second invariant.

In a *simple extension* test, the deformation of a rectangular block along the X_1 direction is given by:

$$x_1 = \lambda X_1 , \quad x_2 = \frac{1}{\sqrt{\lambda}} X_2 , \quad x_3 = \frac{1}{\sqrt{\lambda}} X_3 ,$$

where $\lambda > 1$. Thus, the invariants are

$$\mathcal{I}_1 = \lambda^2 + \frac{2}{\lambda} , \quad \mathcal{I}_2 = 2\lambda + \frac{1}{\lambda^2} , \quad \mathcal{I}_3 = 1 , \tag{4.3}$$

As a consequence, the axial stress T_{11} in simple extension is given by

$$T_{11} = 2\left(\lambda^2 - \frac{1}{\lambda}\right)\left(\frac{\partial \mathcal{W}}{\partial \mathcal{I}_1} + \frac{1}{\lambda}\frac{\partial \mathcal{W}}{\partial \mathcal{I}_2}\right) ,$$

where the derivatives of the strain energy density are evaluated at the values of the invariants given in (4.3). Thus, for the Fung-Demiray model and for the Vito model we

obtain:

$$T_{11}^{FD} = a\left(\lambda^2 - \frac{1}{\lambda}\right) e^{b(\lambda^2+\frac{2}{\lambda}-3)} ,$$
$$T_{11}^{V} = a\left[\delta\left(\lambda^2 - \frac{1}{\lambda}\right) + (1-\delta)\left(\lambda - \frac{1}{\lambda^2}\right)\right] e^{b\left[\delta(\lambda^2+\frac{2}{\lambda}-3)+(1-\delta)(\frac{1}{\lambda^2}+2\lambda-3)\right]} ,$$

respectively. Naturally, for $\delta = 1$, $T_{11}^{V} = T_{11}^{FD}$, and for $b \to 0$ the neo-Hookean and Mooney-Rivlin models are recovered. The plot in Figure 4.1 provides a visual representation of the non-dimensional Cauchy stress T_{11}/a for different values of δ. It is clear that, for a given value of the strain-stiffening parameter b, the Fung-Demiray model predicts a stiffer response than the Vito model, and this effect is particularly noticeable for smaller values of b. In particular, we notice that, for $\lambda = 1,8$, the Fung-Demiray model predicts a Cauchy stress which is double than the one predicted by the Vito model with $\delta = 0,5$.

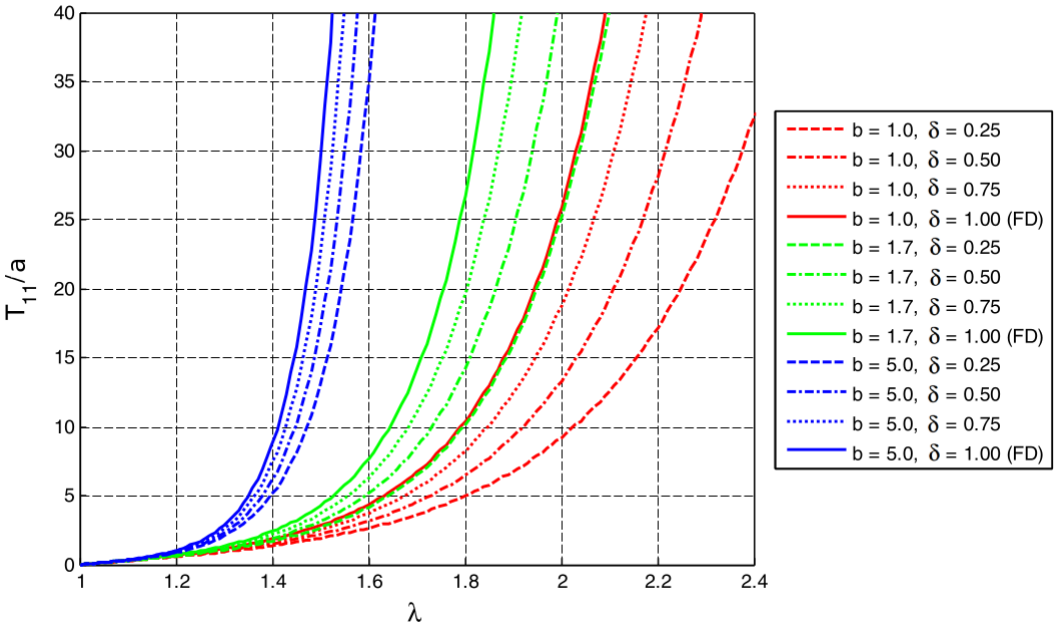

FIGURE 4.1: Cauchy stress response in simple extension for the Fung-Demiray and Vito models (Horgan et al. 2012).

Additionally, we consider a *simple shear* deformation, which can be defined by:

$$x_1 = X_1 + kX_2 , \quad x_2 = X_2 , \quad x_3 = X_3 ,$$

where $k > 0$ denotes the shear in the $X_1 - X_2$ plane. In the case of simple shear, it is well known (Horgan et al. 2010) that the stress field for an incompressible isotropic

elastic material is:

$$\mathsf{T} = \begin{bmatrix} 2k^2\mathcal{W}_1 & 2k(\mathcal{W}_1+\mathcal{W}_2) & 0 \\ 2k(\mathcal{W}_1+\mathcal{W}_2) & -2k^2\mathcal{W}_2 & 0 \\ 0 & 0 & 0 \end{bmatrix}, \tag{4.4}$$

where $\mathcal{W}_i$ denotes the derivative of $\mathcal{W}$ with respect to $\mathcal{I}_i$, evaluated at $\mathcal{I}_i = 3+k^2$. Thus, for the Fung-Demiray and Vito model we obtain:

$$\mathsf{T}^{FD} = ae^{bk^2} \begin{bmatrix} k^2 & k & 0 \\ k & 0 & 0 \\ 0 & 0 & 0 \end{bmatrix}, \tag{4.5}$$

$$\mathsf{T}^{V} = ae^{bk^2} \begin{bmatrix} \delta k^2 & k & 0 \\ k & -k^2(1-\delta) & 0 \\ 0 & 0 & 0 \end{bmatrix}, \tag{4.6}$$

respectively. As we can see, the shear stress is equal to $T_{12} = ake^{bk^2}$ for both models. From (4.4) it is clear that, in the nonlinear elasticity framework, normal stresses are necessary to maintain a state of simple shear (Horgan et al. 2012). The stress component T_{22} represents the traction at the top and bottom faces of the specimen under shear; however, such traction is predicted only for models that show a dependence on the second strain invariant. If no such traction is applied, a specimen under shear will undergo a lateral expansion or a contraction in the direction perpendicular to the shear; as a consequence, materials that exhibit this kind of mechanical behaviour under simple shear cannot be realistically modeled by strain energy functions that do not depend on the second invariant.

4.1.2 Modified Holzapfel-Ogden model

In this section, we focus on the Holzapfel-Ogden model for incompressible orthotropic hyperelastic materials: our aim is to introduce some minor modifications in order to take into account the mechanical influence of the second strain invariant. We recall the

definition of the invariants:

$$\begin{aligned}
\mathcal{I}_1(\mathsf{C}) &= \mathrm{tr}\mathsf{C} \ , \\
\mathcal{I}_2(\mathsf{C}) &= \frac{1}{2}\Big[(\mathrm{tr}\mathsf{C})^2 - \mathrm{tr}\mathsf{C}^2\Big] \ , \\
\mathcal{I}_3(\mathsf{C}) &= \det\mathsf{C} \ , \\
\mathcal{I}_{4,\mathbf{a}}(\mathsf{C}) &= \mathbf{a}\cdot\mathsf{C}\mathbf{a} \ , \\
\mathcal{I}_{5,\mathbf{a}}(\mathsf{C}) &= \mathbf{a}\cdot\mathsf{C}^2\mathbf{a} \ , \\
\mathcal{I}_{8,\mathbf{ab}}(\mathsf{C}) &= \mathbf{a}\cdot\mathsf{C}\mathbf{b} \ ,
\end{aligned}$$

and, given an orthonormal ternary $\{\mathbf{f}_0, \mathbf{s}_0, \mathbf{n}_0\}$, the reduced set of invariants

$$\Upsilon_{\mathrm{HO}} = \Big\{\mathcal{I}_1,\ \mathcal{I}_{4,\mathbf{f}_0},\ \mathcal{I}_{4,\mathbf{s}_0},\ \mathcal{I}_{8,\mathbf{f}_0\mathbf{s}_0}\Big\}$$

is considered in the Holzapfel-Ogden model: as already discussed in detail in Section 2.2, for an incompressible material $\det\mathsf{C} = 1$, and the quadratic invariants are neglected.
In order to introduce the dependence on $\mathcal{I}_2$, a standard approach can be adopted: the strain energy density function associated to the second invariant is

$$\widetilde{\mathcal{W}}_2(\mathcal{I}_2) = \frac{a_2}{2b_2}\Big[e^{b_2(\mathcal{I}_2-3)} - 1\Big] \ .$$

Similarly to the strain energy associated to other invariants, the exponential form allows a proper reproduction of the strain-stiffening effect of the biological tissue, and an additive splitting of the strain energy is possibile:

$$\begin{aligned}
\widehat{\mathcal{W}}(\mathsf{C}) &= \widetilde{\mathcal{W}}(\mathcal{I}_1,\ \mathcal{I}_2,\ \mathcal{I}_{4,\mathbf{f}_0},\ \mathcal{I}_{4,\mathbf{s}_0},\ \mathcal{I}_{8,\mathbf{f}_0\mathbf{s}_0}) = \\
&= \widetilde{\mathcal{W}}_1(\mathcal{I}_1) + \widetilde{\mathcal{W}}_2(\mathcal{I}_2) + \widetilde{\mathcal{W}}_{4,\mathbf{f}_0}(\mathcal{I}_{4,\mathbf{f}_0}) + \widetilde{\mathcal{W}}_{4,\mathbf{s}_0}(\mathcal{I}_{4,\mathbf{s}_0}) + \widetilde{\mathcal{W}}_{8,\mathbf{f}_0\mathbf{s}_0}(\mathcal{I}_{8,\mathbf{f}_0\mathbf{s}_0}) \ .
\end{aligned}$$

Even if this modification of the Holzapfel-Ogden model seems perfectly reasonable, the main difficulty lies in the shear modulus a_2 and in the strain-stiffening parameter b_2 associated to the second invariant: to our knowledge, in the literature no experimental studies that provide an extimate for these parameters are reported. As far as we now, the only thing we could do is to provide an educated guess for these parameters.

The purpose of this section is to provide a couple of different approaches to this problem. The first one, intuitively, is still based on an additive splitting of the strain energy density, but is based on an extra parameter ω which measures the influence of the second

invariant:

$$\widehat{\mathcal{W}}(\mathsf{C}) = \omega\ \widetilde{\mathcal{W}}_1(\mathcal{I}_1) + (1-\omega)\ \widetilde{\mathcal{W}}_2(\mathcal{I}_2) + \widetilde{\mathcal{W}}_{4,\mathbf{f}_0}(\mathcal{I}_{4,\mathbf{f}_0}) + \widetilde{\mathcal{W}}_{4,\mathbf{s}_0}(\mathcal{I}_{4,\mathbf{s}_0}) + \widetilde{\mathcal{W}}_{8,\mathbf{f}_0\mathbf{s}_0}(\mathcal{I}_{8,\mathbf{f}_0\mathbf{s}_0})\ ,$$

where $\omega \in [0,1]$. The exact form for first two terms is given by:

$$\widetilde{\mathcal{W}}_1(\mathcal{I}_1) = \frac{a}{2b}\left[e^{b(\mathcal{I}_1-3)} - 1\right]\ ,$$
$$\widetilde{\mathcal{W}}_2(\mathcal{I}_2) = \frac{a}{2b}\left[e^{b(\mathcal{I}_2-3)} - 1\right]\ ,$$

where we point out that the parameter a and b are the *same* in both cases. Obviously, for $\omega = 1$, the original Holzapfel-Ogden model is recovered, while for $\omega = 0$ the first invariant is completely neglected, in favor of $\mathcal{I}_2$. Following the same argument exposed in Section 2.2, we can compute the first Piola-Kirchhoff tensor:

$$\begin{aligned}\mathsf{P} &= \frac{\partial \mathcal{W}}{\partial \mathsf{F}} - p\ \mathrm{cof} = 2\mathsf{F}\frac{\partial \widehat{\mathcal{W}}}{\partial \mathsf{C}} - p\ \mathrm{cof} = \\ &= 2\mathsf{F}\Bigg[\omega\ \frac{\partial \widetilde{\mathcal{W}}_1}{\partial \mathcal{I}_1}\frac{\partial \mathcal{I}_1}{\partial \mathsf{C}} + (1-\omega)\ \frac{\partial \widetilde{\mathcal{W}}_2}{\partial \mathcal{I}_2}\frac{\partial \mathcal{I}_2}{\partial \mathsf{C}} + \frac{\partial \widetilde{\mathcal{W}}_{4,\mathbf{f}_0}}{\partial \mathcal{I}_{4,\mathbf{f}_0}}\frac{\partial \mathcal{I}_{4,\mathbf{f}_0}}{\partial \mathsf{C}} + \frac{\partial \widetilde{\mathcal{W}}_{4,\mathbf{s}_0}}{\partial \mathcal{I}_{4,\mathbf{s}_0}}\frac{\partial \mathcal{I}_{4,\mathbf{s}_0}}{\partial \mathsf{C}} + \\ &\quad + \frac{\partial \widetilde{\mathcal{W}}_{8,\mathbf{f}_0\mathbf{s}_0}}{\partial \mathcal{I}_{8,\mathbf{f}_0\mathbf{s}_0}}\frac{\partial \mathcal{I}_{8,\mathbf{f}_0\mathbf{s}_0}}{\partial \mathsf{C}}\Bigg] - p\ \mathrm{cof}\ ,\end{aligned}$$

and, recalling the derivative of the second invariant

$$\frac{\partial \mathcal{I}_2}{\partial \mathsf{C}} = \mathrm{tr}\mathsf{C}\ \mathsf{I} - \mathsf{C}\ ,$$

we can compute the explicit form for the Cauchy stress tensor:

$$\begin{aligned}\mathsf{T} &= a\omega\ e^{b(\mathcal{I}_1-3)}\ \mathsf{B} + a(1-\omega)\ e^{b(\mathcal{I}_2-3)}\ (\mathsf{B}\ \mathrm{tr}\mathsf{B} - \mathsf{B}^2) - p\mathsf{I} + \\ &\quad + 2\ a_f(\mathcal{I}_{4,\mathbf{f}_0} - 1)\ e^{b_f(\mathcal{I}_{4,\mathbf{f}_0}-1)^2}\ \mathbf{f}\otimes\mathbf{f} + 2\ a_s(\mathcal{I}_{4,\mathbf{s}_0} - 1)\ e^{b_s(\mathcal{I}_{4,\mathbf{s}_0}-1)^2}\ \mathbf{s}\otimes\mathbf{s} + \\ &\quad + a_{fs}\ \mathcal{I}_{8,\mathbf{f}_0\mathbf{s}_0}\ e^{b_{fs}\mathcal{I}^2_{8,\mathbf{f}_0\mathbf{s}_0}}\ (\mathbf{f}\otimes\mathbf{s} + \mathbf{s}\otimes\mathbf{f})\ .\end{aligned}$$

In the following, the model presented above will be referred to as *additive* Holzapfel-Ogden model; note that the original Holzapfel-Ogden model is additive by nature, and our nomenclature only refers to the treatment of the strain-energy term associated to the second invariant.

In contrast, a different approach is possible, based on the Vito model presented in Section 4.1.1. As a matter of fact, one can consider a single strain-energy term which takes into account for both $\mathcal{I}_1$ and $\mathcal{I}_2$: once again, the model is based on an extra parameter, δ, which reflects the degree of dependence on the second invariant. However, this parameter

is part of the exponent of the expression, and in particular we have:

$$\widetilde{\mathcal{W}}_{1,2}(\mathcal{I}_1,\mathcal{I}_2)=\frac{a}{2b}\left[e^{b\left[\delta(\mathcal{I}_1-3)+(1-\delta)(\mathcal{I}_2-3)\right]}-1\right], \tag{4.7}$$

where $\delta\in[0,1]$. This expression turns out to be the exact form for the strain energy of an incompressible isotropic hyperelastic material according to the Vito model. In our case, the material parameters a and b are the ones that we have previously used for $\widetilde{\mathcal{W}}_1$. This term, which takes into account for both $\mathcal{I}_1$ and $\mathcal{I}_2$, contributes to the total strain energy in an additive way, as usual:

$$\begin{aligned}\widehat{\mathcal{W}}(\mathsf{C})&=\widetilde{\mathcal{W}}(\mathcal{I}_1,\ \mathcal{I}_2,\ \mathcal{I}_{4,\mathbf{f}_0},\ \mathcal{I}_{4,\mathbf{s}_0},\ \mathcal{I}_{8,\mathbf{f}_0\mathbf{s}_0})=\\&=\widetilde{\mathcal{W}}_{1,2}(\mathcal{I}_1,\mathcal{I}_2)+\widetilde{\mathcal{W}}_{4,\mathbf{f}_0}(\mathcal{I}_{4,\mathbf{f}_0})+\widetilde{\mathcal{W}}_{4,\mathbf{s}_0}(\mathcal{I}_{4,\mathbf{s}_0})+\widetilde{\mathcal{W}}_{8,\mathbf{f}_0\mathbf{s}_0}(\mathcal{I}_{8,\mathbf{f}_0\mathbf{s}_0})\ .\end{aligned}$$

It is clear that for $\delta=1$ the original Holzapfel-Ogden model is recovered; additionally, for $\delta=0$ the first invariant is completely neglected, and this model coincides with the additive modification of the Holzapfel-Ogden presented above with $\omega=0$. Obviously, for $0<\omega=\delta<1$, the two models provide a different strain energy.
In this case, the first Piola-Kirchhoff tensor is:

$$\begin{aligned}\mathsf{P}&=\frac{\partial\mathcal{W}}{\partial\mathsf{F}}-p\ \mathrm{cof}=2\mathsf{F}\frac{\partial\widehat{\mathcal{W}}}{\partial\mathsf{C}}-p\ \mathrm{cof}=\\&=2\mathsf{F}\left[\frac{\partial\widetilde{\mathcal{W}}_{1,2}}{\partial\mathsf{C}}+\frac{\partial\widetilde{\mathcal{W}}_{4,\mathbf{f}_0}}{\partial\mathcal{I}_{4,\mathbf{f}_0}}\frac{\partial\mathcal{I}_{4,\mathbf{f}_0}}{\partial\mathsf{C}}+\frac{\partial\widetilde{\mathcal{W}}_{4,\mathbf{s}_0}}{\partial\mathcal{I}_{4,\mathbf{s}_0}}\frac{\partial\mathcal{I}_{4,\mathbf{s}_0}}{\partial\mathsf{C}}+\frac{\partial\widetilde{\mathcal{W}}_{8,\mathbf{f}_0\mathbf{s}_0}}{\partial\mathcal{I}_{8,\mathbf{f}_0\mathbf{s}_0}}\frac{\partial\mathcal{I}_{8,\mathbf{f}_0\mathbf{s}_0}}{\partial\mathsf{C}}\right]-p\ \mathrm{cof}\ ,\end{aligned}$$

where we need to properly compute the exact form for $\frac{\partial\widetilde{\mathcal{W}}_{1,2}}{\partial\mathsf{C}}$:

$$\begin{aligned}\frac{\partial\widetilde{\mathcal{W}}_{1,2}}{\partial\mathsf{C}}&=\frac{\partial}{\partial\mathsf{C}}\left[\frac{a}{2b}\ e^{b\left[\delta(\mathcal{I}_1-3)+(1-\delta)(\mathcal{I}_2-3)\right]}-1\right]=\frac{a}{2b}\ \frac{\partial}{\partial\mathsf{C}}\left[e^{b\delta(\mathcal{I}_1-3)}e^{(1-\delta)(\mathcal{I}_2-3)}\right]=\\&=\frac{a}{2b}\ \frac{\partial}{\partial\mathsf{C}}\left(e^{b\delta(\mathcal{I}_1-3)}\right)e^{(1-\delta)(\mathcal{I}_2-3)}+\frac{a}{2b}\ e^{b\delta(\mathcal{I}_1-3)}\frac{\partial}{\partial\mathsf{C}}\left(e^{(1-\delta)(\mathcal{I}_2-3)}\right)=\\&=\frac{a}{2}\delta\frac{\partial\mathcal{I}_1}{\partial\mathsf{C}}e^{b\left[\delta(\mathcal{I}_1-3)+(1-\delta)(\mathcal{I}_2-3)\right]}+\frac{a}{2}(1-\delta)\frac{\partial\mathcal{I}_2}{\partial\mathsf{C}}e^{b\left[\delta(\mathcal{I}_1-3)+(1-\delta)(\mathcal{I}_2-3)\right]}=\\&=\frac{a}{2}\left[\delta\frac{\partial\mathcal{I}_1}{\partial\mathsf{C}}+(1-\delta)\frac{\partial\mathcal{I}_2}{\partial\mathsf{C}}\right]e^{b\left[\delta(\mathcal{I}_1-3)+(1-\delta)(\mathcal{I}_2-3)\right]}\ .\end{aligned}$$

Recalling that

$$\frac{\partial\mathcal{I}_I}{\partial\mathsf{C}}=\mathsf{I}\ ,\quad \frac{\partial\mathcal{I}_2}{\partial\mathsf{C}}=\mathrm{tr}\mathsf{C}\ \mathsf{I}-\mathsf{C}\ ,$$

the explicit form for the Cauchy stress tensor reads:

$$\begin{aligned}\mathsf{T} = a\delta\ e^{b\left[\delta(\mathcal{I}_1-3)+(1-\delta)(\mathcal{I}_2-3)\right]}\mathsf{B} + a(1-\delta)\ e^{b\left[\delta(\mathcal{I}_1-3)+(1-\delta)(\mathcal{I}_2-3)\right]}(\mathsf{B}\ \mathrm{tr}\mathsf{B} - \mathsf{B}^2) - p\mathsf{I} + \\ + 2\ a_f(\mathcal{I}_{4,\mathbf{f}_0}-1)\ e^{b_f(\mathcal{I}_{4,\mathbf{f}_0}-1)^2}\ \mathbf{f}\otimes\mathbf{f} + 2\ a_s(\mathcal{I}_{4,\mathbf{s}_0}-1)\ e^{b_s(\mathcal{I}_{4,\mathbf{s}_0}-1)^2}\ \mathbf{s}\otimes\mathbf{s} + \\ + a_{fs}\ \mathcal{I}_{8,\mathbf{f}_0\mathbf{s}_0}\ e^{b_{fs}\mathcal{I}^2_{8,\mathbf{f}_0\mathbf{s}_0}}\ (\mathbf{f}\otimes\mathbf{s}+\mathbf{s}\otimes\mathbf{f})\ .\end{aligned}$$

In the following, the model presented above will be referred to as *Vito-Holzapfel-Ogden model.*

4.1.3 Results and discussion

In this Section, we analyse the impact of the second invariant on the ventricular mechanics, thanks to the numerical method which has been widely discussed in previous chapters: our purpose is to evaluate the mechanical influence of the influence of $\mathcal{I}_2$ in the modified Holzapfel-Ogden model, in order to justify the fact that the second strain invariant is usually neglected in the original strain energy form.
First, we consider the case in which the only isotropic contribution in the strain energy comes from the second strain invariant, which means that the first invariant is neglected and $\mathcal{I}_2$ is used in its place:

$$\begin{aligned}\widehat{\mathcal{W}}(\mathsf{C}) &= \widetilde{\mathcal{W}}(\mathcal{I}_2,\ \mathcal{I}_{4,\mathbf{f}_0},\ \mathcal{I}_{4,\mathbf{s}_0},\ \mathcal{I}_{8,\mathbf{f}_0\mathbf{s}_0}) = \\ &= \widetilde{\mathcal{W}}_2(\mathcal{I}_2) + \widetilde{\mathcal{W}}_{4,\mathbf{f}_0}(\mathcal{I}_{4,\mathbf{f}_0}) + \widetilde{\mathcal{W}}_{4,\mathbf{s}_0}(\mathcal{I}_{4,\mathbf{s}_0}) + \widetilde{\mathcal{W}}_{8,\mathbf{f}_0\mathbf{s}_0}(\mathcal{I}_{8,\mathbf{f}_0\mathbf{s}_0})\ .\end{aligned}$$

This is equivalent to considering the additive model with $\omega = 0$ or the Vito-Holzapfel-Ogden model with $\delta = 0$. Once again, we recall that the shear modulus a and the strain-stiffening parameter b for $\mathcal{W}_2$ are the ones computed by Wang and co-workers associated to $\mathcal{I}_1$ (see Table 2.1 for reference).
We performed a numerical simulation based on this choice, considering a microstructure characterized by a helix angle that linearly spans the $(-60°, 60°)$ interval, and a radial laminar structure. We can directly compared the results with the simulation discussed in Section 2.7.

Indicator	**Value**
Stroke Volume	22,15 ml
Ejection Fraction	55,25 %
Thickening Base	27,25 %
Thickening Apex	29,54 %
Shortening	3,72 %
Height/Radius Ratio EDP	2,53 %
Height/Radius Ratio ESP	2,60 %
Torsion	9,77°

TABLE 4.1: Set of physiological indicators for the simulation based on $\mathcal{I}_2$ instead of $\mathcal{I}_1$

A comparison with the set of physiological indicators reported in Table 4.1 shows that no significant change is reported; however, we notice a small and almost negligible reduction in the ventricular efficiency, wall thickening and shortening. A minor difference can be spotted in the ventricular height during the cycle: as a matter of fact, if $\mathcal{I}_2$ is considered, the ventricle is about 0,5 cm shorter both at the end of diastole, at the end of the isochoric contraction phase and at the end-systolic point. However, we can state that the global ventricular functioning is not significantly affected by this modification. In order to evaluate the impact of the choice of either $\mathcal{I}_1$ or $\mathcal{I}_2$, we should look closely to the spatial and temporal variation of the invariants and their corresponding strain energy density. Both invariants have a similar trend during the cardiac cycle, with a secondary peak at the end of the isovolumic contraction phase. However, we report that the end-systolic peak of $\mathcal{I}_2$ takes place far from both the endocardium and the midwall, while the peak for $\mathcal{I}_1$ is very close to the endocardium. From the energetic point of view, the variation of strain energy during the cycle is similar, but if $\mathcal{I}_2$ is used, $\mathcal{W}_2$ has notably

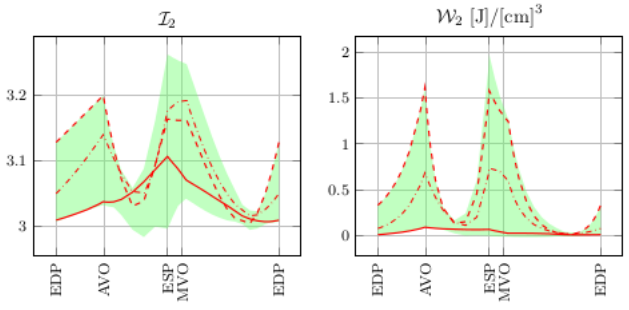

FIGURE 4.2: Plot of the second invariant and the corresponding strain energy density during the cardiac cycle for a simulation considering the second strain invariant instead of the first. The lines refer to the sub-epicardium (solid line), sub-endocardium (dashed line), and mid-myocardium (dash-dotted line). The green area represents the range of values spanned in the radial direction. The data are taken in a mid-axis section of the ellipsoid.

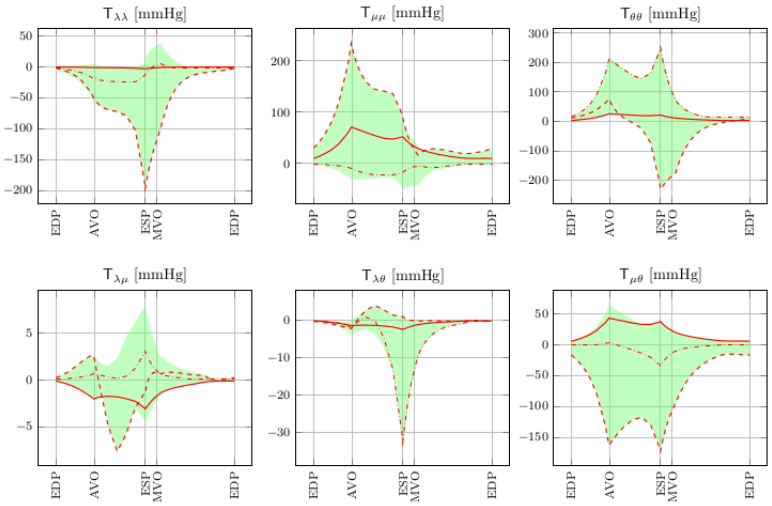

FIGURE 4.3: Plot of Cauchy stress components during the cardiac cycle for a simulation considering the second strain invariant instead of the first. The lines refer to the sub-epicardium (solid line), sub-endocardium (dashed line), and mid-myocardium (dash-dotted line). The green area represents the range of values spanned in the radial direction. The data are taken in a mid-axis section of the ellipsoid.

higher peaks.

Analysing the stress distribution, we report higher end-systolic peaks for the diagonal components of the Cauchy stress, with increases between 10% and 30%. Additionally, the same is true for the material pressure p, which we recall is used in the model as a Lagrangian multiplier in order to enforce incompressibility. However, apart from these minor differences, no significant changes are found.

In order to further analyse the effects of the introduction of the second strain invariant, we now consider the additive model chosing $\omega = 0.5$ and compare it with the results obtained from the Vito-Holzapfel-Ogden model with $\delta = 0.5$. Thus, we are considering that $\mathcal{I}_1$ and $\mathcal{I}_2$ have the same significance in the mechanics, which is a reasonable assumption.

Once again, with reference to Table 4.2, no macroscopic differences can be found in the principal physiological quantities during the cardiac cycle. Similarly to the case $\delta = \omega = 0$, higher end-sistolic values for stresses are found in both cases.

In the additive model, we notice that $\mathcal{W}_2$ takes higher values with respect to $\mathcal{W}_1$, with a 20% higher end-systolic peak; additionally, an high strain-energy density for the second invariant is registered at the end of the isochoric contraction phase. On the other hand, for the Vito-Holzapfel-Ogden model the trend for $\mathcal{W}_{1,2}$ is quite standard, and its magnitude is almost equal to the sum of the magnitudes of $\mathcal{W}_1$ and $\mathcal{W}_2$ in the additive model. Referring to the values of invariants, almost no differences are found between the two models.

Indicator	$\omega = 0.5$	$\delta = 0.5$
Stroke Volume	22,34 ml	22,36 ml
Ejection Fraction	55,58 %	55,62 %
Thickening Base	27,60 %	27,62 %
Thickening Apex	30,03 %	30,18 %
Shortening	3,77 %	3,75 %
Height/Radius Ratio EDP	2,53 %	2,53
Height/Radius Ratio ESP	2,60 %	2,60
Torsion	9,87°	9,89°

TABLE 4.2: Set of physiological indicators for the the additive model with $\omega = 0.5$ and the Vito-Holzapfel-Ogden model with $\delta = 0.5$

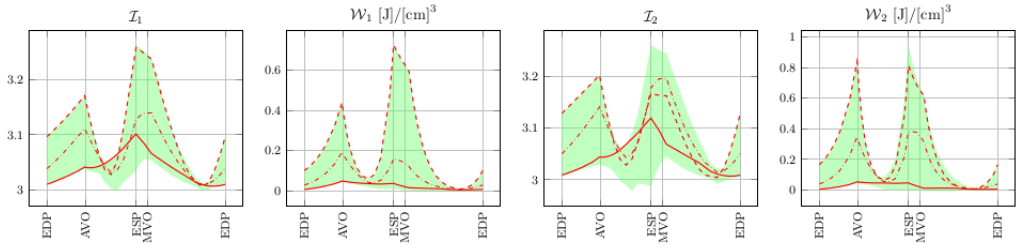

FIGURE 4.4: Plot of the first two invariant and the corresponding strain energy density during the cardiac cycle for a simulation considering the additive model with $\omega = 0.5$. The lines refer to the sub-epicardium (solid line), sub-endocardium (dashed line), and mid-myocardium (dash-dotted line). The green area represents the range of values spanned in the radial direction. The data are taken in a mid-axis section of the ellipsoid.

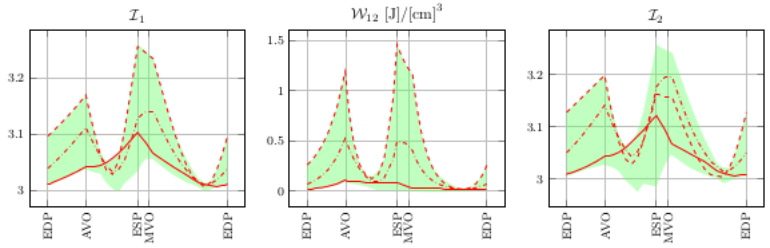

FIGURE 4.5: Plot of the first two invariants and the strain energy density associated to the second invariant during the cardiac cycle for a simulation considering the Vito-Holzapfel-Ogden model with $\delta = 0.5$. The lines refer to the sub-epicardium (solid line), sub-endocardium (dashed line), and mid-myocardium (dash-dotted line). The green area represents the range of values spanned in the radial direction. The data are taken in a mid-axis section of the ellipsoid.

In conclusion, we can state that the introduction of the second strain invariant in the Holzapfel-Ogden model has no significant impact on the mechanical state of the ventricle during the cardiac cycle, and as a consequence it can be neglected in the model, as originally assumed by Holzapfel and Ogden. However, we provided two different modifications which allow the inclusion of the second invariant, and both of them seem appropriate both from the theoretical and numerical point of view.

4.2 Boundary Conditions

When solving the variational formulation associated to a partial differential equation using a finite element method, the application of boundary conditions plays an important role, as it can greatly affect the numerical solution. However, in the case of the left ventricle, the proper modelling of the mechanical effects of the surrounding anatomy of the heart is not an easy task.

The cardiac muscle is surrounded by the pericardium, a fibrous sac which consists of two different layers: the visceral pericardium, which is a part of the epicardium, and the parietal pericardium; between the two, the pericardial fluid acts as a lubricant. As a consequence, there should be (almost) no friction, and a common choice is not to impose any kind of boundary conditions at the epicardial surface. Nevertheless, a proper model should include the interaction of the left ventricle with the right ventricle, as the *intraventricular septum*, which is the wall separating the two sides of the heart, shows a different mechanical behaviour with respect to the rest of the ventricular wall. However, in our work we neglect this interaction, as we are focusing on the left ventricle in a vacuum: in the case of numerical models, this is a common choice in the literature.

If no essential boundary conditions are applied, or if they only affect some components of the deformation, there might not be a unique solution for the variational problem: as a matter of fact, a sum of the 'real' solution of the elastic problem and any kind of rigid motion that satisfies the boundary conditions is an admissible solution.

4.2.1 Mean displacement and rotation

In the numerical model presented in Chapter 2, we assumed that the base of the ventricle was fixed in the longitudinal direction, so that no vertical displacement can take place: this is a reasonable hypothesis, as the ventricle is fixed to the left atrium. Consequently, we will always consider the Dirichlet boundary condition on the z-component on the basal plane.

As briefly introduced in Section 2.7, the strategy used in the simulations performed in previous chapters was based on the requirement of zero mean rotation and zero mean displacement of the whole ventricle, in order to avoid any rigid motion. In particular

$$\int_{\Omega_0} \boldsymbol{\varphi} \, \mathrm{d}V = 0 \tag{4.8}$$

means that the mean displacement of the whole reference domain is null, and

$$\int_{\Omega_0} \mathbf{X} \times \boldsymbol{\varphi} \, \mathrm{d}V = 0 \tag{4.9}$$

imposes zero mean rotation. However, we need more specific conditions, in order to avoid non-physiological alterations to the ventricular mechanics. First of all, given that we are imposing Dirichlet boundary conditions for the z-component at the base, we should remove the zero mean displacement condition in the longitudinal direction, so that the ventricle can shorten during the cardiac cycle. Given the twisting motion of the ventricle, the assumption of a zero mean displacement in the $x-$ and $y-$direction seems reasonable. Additionally, we obviously impose the zero mean rotation condition only around the longitudinal axis of the ventricle, which is trivially obtained by considering the last component of (4.9).
These kind of 'volumetric' constraints can be applied through the proper use of Lagrangian multipliers: the complete Lagrangian formulation reads:

$$\mathcal{L}_{BC}(\boldsymbol{\varphi}, p, \xi; \gamma, c_1, c_2, c_3) := \mathcal{L}(\boldsymbol{\varphi}, p, \xi; \gamma) + \int_{\Omega_0} c_1 X_1 + c_2 X_2 \, \mathrm{d}V + c_3 \int_{\Omega_0} (\mathbf{X} \times \boldsymbol{\varphi})_3 \, \mathrm{d}V$$

where $\mathcal{L}$ is the Lagrangian formulation which has been widely discussed in Section 2.5, $\mathbf{X} = (X_1, X_2, X_3)$ and $(\mathbf{X} \times \boldsymbol{\varphi})_3$ denotes the third (longitudinal) component of the cross product. c_1, c_2 and c_3 are the Lagrangian multipliers introduced in order to impose the global constraint.

4.2.2 A hint to physiological boundary conditions

Even if the imposition of global rotation and displacement constraints seems reasonable from a mechanical viewpoint, this choice hardly encodes the effect of the boundary on the ventricular kinematics. In the literature, several different approaches have been used, but most of them do not model the surrounding of the ventricle in a realistic way: for instance, Bovendeerd and co-workers (1992) completely suppressed the rotation of the endocardial basal ring; while it is true that the ventricular base is fixed to the left atrium, a non-zero basal endocardial rotation is commonly reported in medical researches (such as Young et al. 2012): thus, we do not completely understand this modelling choice, which has a negative impact on ventricular torsion.
A first modification with respect to the strategy presented in Section 4.2.1, could lie in the imposition of the 'zero mean rotation' constraint only on the basal plane. However, this approach naturally leads to an opposite endocardial rotation with respect to the epicardial one, which is a non-physiological behaviour (Young et al. 2012). In addition, if every other boundary condition is removed, the ventricle undergoes a large apical rotation, resulting in a non-physiological twitch.
In order to adopt more physiological boundary conditions, we should remove the global

constraints imposed through Lagrangian multipliers. We base our analysis on Robin-type boundary conditions in order to model the surrounding anatomy of the heart, which means that a traction proportional to the displacement is considered.
First, we should take into account the fact that the ventricular base is closely attached to the left atrium. In the variational formulation, we consider the boundary term

$$-\int_{\Gamma_{base}} \mathsf{T}\mathbf{n}\cdot\eta \ \mathrm{d}A \ ,$$

where Γ_{base} denotes the basal plane and $\mathbf{n}$ is the outward normal. Given that no vertical displacement of the base is possible, we can simply consider

$$-\int_{\Gamma_{base}} \mathsf{T}\mathbf{n}\cdot\eta \ \mathrm{d}A = -\int_{\Gamma_{base}} t_x\eta_x + t_y\eta_y \ \mathrm{d}A \ ,$$

where t_x and t_y are the first two components of $\mathsf{T}\mathbf{n}$. Imposing the boundary condition $t_x = -k_1 u_x$, $t_y = -k_1 u_y$ we have

$$-\int_{\Gamma_{base}} t_x\eta_x + t_y\eta_y \ \mathrm{d}A \ = k \ \int_{\Gamma_{base}} u_x\eta_x + u_y\eta_y \ \mathrm{d}A \ .$$

Obviously, the most difficult task is the choice of the parameter k_1, which depends on material parameters and on the nature of the interaction between the ventricular base and the apex. Nevertheless, we point out that this kind of boundary conditions could severely hinder the basal rotation during the cardiac cycle, especially for high values of k_1.
Another possible improvement is related to the presence of the pericardium, the fibrous sac which contains the heart: it is filled with pericardial fluid and it is characterized by an high stiffness. In order to mimic the presence of the pericardium, a viable strategy could be the introduction of a Robin-type boundary condition which models a traction proportional to the radial displacement of the epicardial surface. For instance, if the radial position in the reference and in the actual configuration are given by

$$R = \sqrt{X^2 + Y^2} \quad \text{and} \quad r = \sqrt{x^2 + y^2} \ ,$$

respectively, then the resulting radial displacement is $u_r = r - R$. We assume that the radial stress is related to the radial displacement, which means

$$t_r = -k_2 u_r \ .$$

As a consequence, in the variational formulation we have

$$-\int_{\Gamma_{epi}} \mathsf{T}\mathbf{n}\cdot\eta \ \mathrm{d}A \ = k_2 \ \int_{\Gamma_{epi}} t_r\eta_r \ \mathrm{d}A \ ,$$

where Γ_{epi} denotes the epicardial surface and η_r is a proper radial test function, such as

$$\eta_r = \frac{\eta_x x + \eta_y y}{r} \ .$$

Once again, the choice of the value of the parameter k_2 is a key issue for this type of boundary condition: clearly, it should be closely related to the tissue modulus of the pericardium, which has been widely investigated in the literature (Lee et al. 1985). However, by imposing this kind of constraint we are penalising the epicardial expansion, and the mechanical behaviour of the ventricle could be altered during the cardiac cycle: for instance, this modelling choice could have a notable impact on the values for basal wall thickening and ejection fraction.

In conclusion, physiological boundary conditions could lead to a more complete model for ventricular mechanics, but several mechanical and anatomical features have to be considered. Additionally, the imposition of Robin-type conditions that correlate traction and displacement are based on the choice of modelling parameters, which could be hard to determine in a correct way. We do not further investigate this topic, because we presume that a complete modelling of the surrounding anatomy of the heart can only be achieved starting from a realistic geometry of the left ventricle, so that the interaction with other ventricular chambers can be taken into account.

CONCLUSIONS AND FUTURE WORK

We have illustrated a mathematical and numerical model for the left ventricle of the heart, based on the mechanical model originally proposed by Holzapfel and Ogden; the active behaviour of cardiac muscle fibres has been taken into account using an active strain approach. A proper variational formulation for the cardiac pressure-volume loop has been provided, and the finite element method has been exploited in order to perform several numerical simulations of the ventricular mechanics.

The mechanical impact of the microstructure of the cardiac wall is the main focus of this work: the myocardium is composed of a complex bundle of helical muscle fibres, which are organized in laminar structures. Based on the proposed model and on the numerical simulations which have been performed considering a simplified geometry for a canine ventricle, the variation of the helix angle of myofibres inside the wall thickness appeared to be a key determinant of the cardiac function: we have analysed in detail several different fibre configurations, in order to determine their effect on the ventricular functionality. We have found that a higher portion of longitudinal fibres, located in the sub-endocardial and sub-epicardial layers, provides the correct physiological shortening of the ventricle during the cardiac cycle, but in turn reduces the torsion; the values for ventricular twitch registered in medical studies can be recovered by assuming that myofibres are left-handed at the middle of the cardiac wall, resulting in an asymmetric distribution of fibres, consistently with most physiological researches on healthy hearts. In addition, we have discussed the role of the transverse angle, which adds a mechanical coupling between the endocardium and the epicardium; based on our simulations, the influence on the thickening of the ventricular wall reported in the literature has been confirmed. Moreover, we have evaluated the mechanical impact of a non-radial sheet distribution, which yields a slight increase in the physiological quantities which have been considered.

Finally, we proposed a modification of the original Holzapfel-Ogden model in order to include the second strain invariant. Nevertheless, no significant differences in the distribution of strain and stress in the ventricular wall have been registered, and we have concluded that it is possible to neglect the second invariant in the model with no relevant changes in the mechanics.
Last but not least, a detailed insight on the imposition of boundary condition has been provided: in place of the mean displacement and mean axial rotation constraints, we have proposed two Robin-type boundary conditions in order to take into account the presence of the pericardium and the interaction with the left atrium in the basal region.

Our research is based on a complete mechanical model, which is applied to a simplified geometry of the left ventricle. First of all, the implementation of the valve-opening effect could have a notable impact on the cardiac mechanics, in particular during the systolic phase. Another natural improvement to the present work is to consider a more physiological ventricular geometry, together with a realistic fibre and sheet configuration, which can be obtained exploiting the most recent imaging techniques and advanced fibre-tracking algorithms. Additionally, it is possibile to consider the mechanics of the whole cardiac muscle, in order to take into account the interaction between the four chambers of the heart in a physiologically accurate way. Moreover, the proper modelling of the surrounding anatomy of the heart is another key element for a complete cardiac model that could be useful for medical purposes, such as the identification and treatment of several cardiac pathologies.

BIBLIOGRAPHY

[1] Martin S. Alnæs. *UFL: a Finite Element Form Language*, chapter 17. Springer, 2012.

[2] Martin S. Alnæs, Anders Logg, and Kent-Andre Mardal. *UFC: a Finite Element Code Generation Interface*, chapter 16. Springer, 2012.

[3] Martin S. Alnæs, Anders Logg, Kent-Andre Mardal, Ola Skavhaug, and Hans Petter Langtangen. Unified framework for finite element assembly. *International Journal of Computational Science and Engineering*, 4(4):231–244, 2009.

[4] Martin S. Alnæs, Anders Logg, Kristian B. Ølgaard, Marie E. Rognes, and Garth N. Wells. Unified form language: A domain-specific language for weak formulations of partial differential equations. *ACM Transactions on Mathematical Software*, To appear, 2013.

[5] Martin S. Alnæs and Kent-Andre Mardal. On the efficiency of symbolic computations combined with code generation for finite element methods. *ACM Transactions on Mathematical Software*, 37(1), 2010.

[6] Martin S. Alnæs and Kent-Andre Mardal. *SyFi and SFC: Symbolic Finite Elements and Form Compilation*, chapter 15. Springer, 2012.

[7] Peter HM Bovendeerd, Wilco Kroon, and Tammo Delhaas. Determinants of left ventricular shear strain. *American Journal of Physiology-Heart and Circulatory Physiology*, 297(3):H1058–H1068, 2009.

[8] PHM Bovendeerd, T Arts, JM Huyghe, DH Van Campen, and RS Reneman. Dependence of local left ventricular wall mechanics on myocardial fiber orientation: a model study. *Journal of biomechanics*, 25(10):1129–1140, 1992.

[9] PHM Bovendeerd, JM Huyghe, T Arts, DH Van Campen, and RS Reneman. Influence of endocardial-epicardial crossover of muscle fibers on left ventricular wall mechanics. *Journal of biomechanics*, 27(7):941–951, 1994.

[10] Maurice B Buchalter, James L Weiss, Walter J Rogers, Elias A Zerhouni, Myron L Weisfeldt, Rafael Beyar, and Edward P Shapiro. Noninvasive quantification of left ventricular rotational deformation in normal humans using magnetic resonance imaging myocardial tagging. *Circulation*, 81(4):1236–1244, 1990.

[11] Valentina Carapella, Rafel Bordas, Pras Pathmanathan, Maelene Lohezic, Jurgen E Schneider, Peter Kohl, Kevin Burrage, and Vicente Grau. Quantitative study of the effect of tissue microstructure on contraction in a computational model of rat left ventricle. *PloS one*, 9(4):e92792, 2014.

[12] Piero Colli Franzone, Luciano Guerri, Micol Pennacchio, and Bruno Taccardi. Spread of excitation in 3-d models of the anisotropic cardiac tissue. ii. effects of fiber architecture and ventricular geometry. *Mathematical biosciences*, 147(2):131–171, 1998.

[13] CA Conti, E Votta, C Corsi, D De Marchi, G Tarroni, M Stevanella, M Lombardi, O Parodi, EG Caiani, and A Redaelli. Left ventricular modelling: a quantitative functional assessment tool based on cardiac magnetic resonance imaging. *Interface focus*, page rsfs20100029, 2011.

[14] Kevin D Costa, Yasuo Takayama, Andrew D McCulloch, and James W Covell. Laminar fiber architecture and three-dimensional systolic mechanics in canine ventricular myocardium. *American Journal of Physiology-Heart and Circulatory Physiology*, 276(2):H595–H607, 1999.

[15] Hilmi Demiray. A note on the elasticity of soft biological tissues. *Journal of biomechanics*, 5(3):309–311, 1972.

[16] Paul WM Fedak, Subodh Verma, Richard D Weisel, and Ren-Ke Li. Cardiac remodeling and failure: from molecules to man (part i). *Cardiovascular Pathology*, 14(1):1–11, 2005.

[17] YC Fung. Elasticity of soft tissues in simple elongation. *Am. J. Physiol*, 213(6):1532–1544, 1967.

[18] T Christian Gasser, Ray W Ogden, and Gerhard A Holzapfel. Hyperelastic modelling of arterial layers with distributed collagen fibre orientations. *Journal of the royal society interface*, 3(6):15–35, 2006.

[19] Liesbeth Geerts, Peter Bovendeerd, Klaas Nicolay, and Theo Arts. Characterization of the normal cardiac myofiber field in goat measured with mr-diffusion tensor imaging. *American Journal of Physiology-Heart and Circulatory Physiology*, 283(1):H139–H145, 2002.

[20] Patrick A Helm, Laurent Younes, Mirza F Beg, Daniel B Ennis, Christophe Leclercq, Owen P Faris, Elliot McVeigh, David Kass, Michael I Miller, and Raimond L Winslow. Evidence of structural remodeling in the dyssynchronous failing heart. *Circulation Research*, 98(1):125–132, 2006.

[21] Johan Hoffman, Johan Jansson, Rodrigo V. de Abreu, Cem Degirmenci, Niclas Jansson, Kaspar Müller, Murtazo Nazarov, and Jeanette H. Spühler. Unicorn: Parallel adaptive finite element simulation of turbulent flow and fluid-structure interaction for deforming domains and complex geometry. *Computer and Fluids*, in press, 2012.

[22] Johan Hoffman, Johan Jansson, Cem Degirmenci, Niclas Jansson, and Murtazo Nazarov. *Unicorn: a Unified Continuum Mechanics Solver*, chapter 18. Springer, 2012.

[23] Johan Hoffman, Johan Jansson, Niclas Jansson, C. Johnson, and Rodrigo V. de Abreu. *Turbulent Flow and Fluid–structure Interaction*, chapter 28. Springer, 2012.

[24] Gerhard A Holzapfel, Thomas C Gasser, and Ray W Ogden. A new constitutive framework for arterial wall mechanics and a comparative study of material models. *Journal of elasticity and the physical science of solids*, 61(1-3):1–48, 2000.

[25] Gerhard A Holzapfel and Ray W Ogden. Constitutive modelling of passive myocardium: a structurally based framework for material characterization. *Philosophical Transactions of the Royal Society A: Mathematical, Physical and Engineering Sciences*, 367(1902):3445–3475, 2009.

[26] CO Horgan and JG Murphy. Simple shearing of incompressible and slightly compressible isotropic nonlinearly elastic materials. *Journal of Elasticity*, 98(2):205–221, 2010.

[27] Cornelius O Horgan and Michael G Smayda. The importance of the second strain invariant in the constitutive modeling of elastomers and soft biomaterials. *Mechanics of Materials*, 51:43–52, 2012.

[28] Niclas Jansson, Johan Jansson, and Johan Hoffman. Framework for massively parallel adaptive finite element computational fluid dynamics on tetrahedral meshes. *SIAM Journal on Scientific Computing*, 34(1):C24–C41, 2012.

[29] Robert C. Kirby. Algorithm 839: Fiat, a new paradigm for computing finite element basis functions. *ACM Transactions on Mathematical Software*, 30(4):502–516, 2004.

[30] Robert C. Kirby. *FIAT: Numerical Construction of Finite Element Basis Functions,*, chapter 13. Springer, 2012.

[31] Robert C. Kirby, Matthew G. Knepley, Anders Logg, and L. Ridgway Scott. Optimizing the evaluation of finite element matrices. *SIAM Journal on Scientific Computing*, 27(3):741–758, 2005.

[32] Robert C. Kirby and Anders Logg. A compiler for variational forms. *ACM Transactions on Mathematical Software*, 32(3), 2006.

[33] Robert C. Kirby and Anders Logg. Efficient compilation of a class of variational forms. *ACM Transactions on Mathematical Software*, 33(3), 2007.

[34] Robert C. Kirby and Anders Logg. Benchmarking domain-specific compiler optimizations for variational forms. *ACM Transactions on Mathematical Software*, 35(2):1–18, 2008.

[35] Robert C. Kirby, Anders Logg, L. Ridgway Scott, and Andy R. Terrel. Topological optimization of the evaluation of finite element matrices. *SIAM Journal on Scientific Computing*, 28(1):224–240, 2006.

[36] Robert C. Kirby and L. Ridgway Scott. Geometric optimization of the evaluation of finite element matrices. *SIAM Journal on Scientific Computing*, 29(2):827–841, 2007.

[37] J Michael Lee and Derek R Boughner. Mechanical properties of human pericardium. differences in viscoelastic response when compared with canine pericardium. *Circulation research*, 57(3):475–481, 1985.

[38] IJ LeGrice, Y Takayama, and JW Covell. Transverse shear along myocardial cleavage planes provides a mechanism for normal systolic wall thickening. *Circulation Research*, 77(1):182–193, 1995.

[39] Anders Logg. Automating the finite element method. *Archives of Computational Methods in Engineering*, 14(2):93–138, 2007.

[40] Anders Logg. Efficient representation of computational meshes. *International Journal of Computational Science and Engineering*, 4(4):283–295, 2009.

[41] Anders Logg, Kent-Andre Mardal, Garth N. Wells, et al. *Automated Solution of Differential Equations by the Finite Element Method.* Springer, 2012.

[42] Anders Logg, Kristian B. Ølgaard, Marie E. Rognes, and Garth N. Wells. *FFC: the FEniCS Form Compiler*, chapter 11. Springer, 2012.

[43] Anders Logg and Garth N. Wells. Dolfin: Automated finite element computing. *ACM Transactions on Mathematical Software*, 37(2), 2010.

[44] Anders Logg, Garth N. Wells, and Johan Hake. *DOLFIN: a C++/Python Finite Element Library*, chapter 10. Springer, 2012.

[45] Herve Lombaert, Jean-Marc Peyrat, Laurent Fanton, Farida Cheriet, Hervé Delingette, Nicholas Ayache, Patrick Clarysse, Isabelle Magnin, and Pierre Croisille. Variability of the human cardiac laminar structure. In *Statistical Atlases and Computational Models of the Heart. Imaging and Modelling Challenges*, pages 160–167. Springer, 2012.

[46] JG Murphy. Transversely isotropic biological, soft tissue must be modelled using both anisotropic invariants. *European Journal of Mechanics-A/Solids*, 42:90–96, 2013.

[47] Ray W Ogden and Gerhard A Holzapfel. *Mechanics of biological tissue*. Springer, 2006.

[48] Raymond W Ogden. *Non-linear elastic deformations*. Courier Dover Publications, 1997.

[49] Kristian B. Ølgaard, Anders Logg, and Garth N. Wells. Automated code generation for discontinuous galerkin methods. *SIAM Journal on Scientific Computing*, 31(2):849–864, 2008.

[50] Kristian B. Ølgaard and Garth N. Wells. Optimisations for quadrature representations of finite element tensors through automated code generation. *ACM Transactions on Mathematical Software*, 37, 2010.

[51] Pearu Peterson, Mari Kalda, and Marko Vendelin. Real-time determination of sarcomere length of a single cardiomyocyte during contraction. *American Journal of Physiology-Cell Physiology*, 304(6):C519–C531, 2013.

[52] S Pezzuto. Mechanics of the heart: constitutive issues and numerical experiments. *Doctoral Thesis*, 2013.

[53] S Pezzuto and D Ambrosi. Active contraction of the cardiac ventricle and distortion of the microstructural architecture. *Biomechanics and Modeling in Mechanobiology*, 2014.

[54] Paolo Piras, Antonietta Evangelista, Stefano Gabriele, Paola Nardinocchi, Luciano Teresi, Concetta Torromeo, Michele Schiariti, Valerio Varano, and Paolo Emilio Puddu. 4d-analysis of left ventricular heart cycle using procrustes motion analysis. *PloS one*, 9(1):e86896, 2014.

[55] Marie E. Rognes, Robert C. Kirby, and Anders Logg. Efficient assembly of h(div) and h(curl) conforming finite elements. *SIAM Journal on Scientific Computing*, 31(6):4130–4151, 2009.

[56] Damien Rohmer, Arkadiusz Sitek, and Grant T Gullberg. Reconstruction and visualization of fiber and laminar structure in the normal human heart from ex vivo diffusion tensor magnetic resonance imaging (dtmri) data. *Investigative radiology*, 42(11):777–789, 2007.

[57] Iris K Rüssel, Marco JW Götte, Jean G Bronzwaer, Paul Knaapen, Walter J Paulus, and Albert C van Rossum. Left ventricular torsion: an expanding role in the analysis of myocardial dysfunction. *JACC: Cardiovascular Imaging*, 2(5):648–655, 2009.

[58] Iris K Rüssel, Sandra R Tecelão, Joost PA Kuijer, Robert M Heethaar, and J Tim Marcus. Comparison of 2d and 3d calculation of left ventricular torsion as circumferential-longitudinal shear angle using cardiovascular magnetic resonance tagging. *Journal of Cardiovascular Magnetic Resonance*, 11(1):1–7, 2009.

[59] Daniel D Streeter. Gross morphology and fiber geometry of the heart. *Handbook of physiology*, pages 61–112, 1979.

[60] Daniel D Streeter, Henry M Spotnitz, Dali P Patel, John Ross, and Edmund H Sonnenblick. Fiber orientation in the canine left ventricle during diastole and systole. *Circulation research*, 24(3):339–347, 1969.

[61] F Torrent-Guasp. The cardiac muscle. *Madrid, Juan March Foundation*, 1973.

[62] SWJ Ubbink, PHM Bovendeerd, Tammo Delhaas, Theo Arts, and Frans N van de Vosse. Towards model-based analysis of cardiac mr tagging data: relation between left ventricular shear strain and myofiber orientation. *Medical image analysis*, 10(4):632–641, 2006.

[63] Raymond Vito. A note on arterial elasticity. *Journal of biomechanics*, 6(5):561–564, 1973.

[64] HM Wang, H Gao, XY Luo, C Berry, BE Griffith, RW Ogden, and TJ Wang. Structure-based finite strain modelling of the human left ventricle in diastole. *International journal for numerical methods in biomedical engineering*, 29(1):83–103, 2013.

[65] HM Wang, XY Luo, H Gao, RW Ogden, BE Griffith, C Berry, and TJ Wang. A modified holzapfel-ogden law for a residually stressed finite strain model of the human left ventricle in diastole. *Biomechanics and modeling in mechanobiology*, 13(1):99–113, 2014.

[66] Alan Wineman. Some results for generalized neo-hookean elastic materials. *International Journal of Non-Linear Mechanics*, 40(2):271–279, 2005.

[67] Alistair A Young and Brett R Cowan. Evaluation of left ventricular torsion by cardiovascular magnetic resonance. *J Cardiovasc Magn Reson*, 14:49, 2012.